Characterizing the influence of neutron fields in causing single-event effects using portable detectors

By CAI Xiao Xiao

A thesis submitted in partial fulfilment

of the requirements for the degree of

DOCTOR OF PHILOSOPHY

University of Central Lancashire

March 2010

Declaration

I declare that while registered as a candidate for the research degree, I have not been a registered candidate or enrolled student for another award of the University or other academic or professional institution. I declare that no material contained in the thesis has been used in any other submission for an academic award and is solely my own work.

Cai Xiao Xiao

To my family

Acknowledgements

I would like to thank Dr. Simon Platt and Mr. Bryan Cassels and Prof. Djamel Ait-Boudaoud for supervising my research, and their guidance, advice, and encouragement throughout every stage of this study.

I would like to thank Dr. Zoltán Török for his invaluable help during my first year of study. His PhD research is the solid foundation of this work. I would like to thank Dr. Chen Wei and Dr. Guy Rolland for their helpful comments on my simulation models. I also would like to thank Prof. Jean-Luc Autran for providing the resources of our long term experiment at the Altitude SEE Test European Platform (ASTEP).

I would like to thank my colleagues in Advanced Digital Signal and Image Processing (ADSIP) Centre. I received great supports from them in my stay at UCLan, especially during the preparation of this thesis.

Abstract

The malfunction of semiconductor devices caused by cosmic rays is known as Single Event Effects(SEEs). In the atmosphere, secondary neutrons are the dominant particles causing this effect. The neutron flux density in atmosphere is very low. For a good statistical certainty, millions of device hours are required to measure the event rate of a device in the natural environment. Event rates obtained in such testings are accurate. To reduce the cost and time of getting the event rate, a device is normally taken to artificial accelerated neutron beams to measure its sensitivity to neutrons. Comparing the flux density of the beam and the flux density of a location in the atmosphere, the real time event rate can be predicted by the event rate obtained. This testing method was standardized as the neutron accelerated soft error rate (ASER) testing in JEDEC JESD89A standard. However, several life testings indicated that the neutron flux density predictions given by the accelerated testings can have large errors. Up to a factor of 2 discrepancy was reported in the literature. One of the major error sources is the equivalence of the absolute neutron flux density in the atmosphere and in accelerated beam.

This thesis proposes an alternative accelerated method of predicting the real-time neutron error rate by using proxy devices. This method can avoid the error introduced by the uncertainty in the neutron flux density.

The Imaging Single Event Effect Monitor (ISEEM) is one of the proxy devices. It is the instrument originally developed by Z. Török and his co-workers in the University of Central Lancashire. A CCD was used as the sensitive element to detect neutrons. A large amount of data sets acquired by Török were used in this work. A re-engineered ISEEM has been developed in this work to improve ISEEM performance in life testings. Theoretical models have been developed to analyze the response of ISEEM in a wide range of neutron facilities and natural

environment. The agreement of the measured and calculated cross-sections are within the error quoted by facilities. Because of the alpha contamination and primary proton direct ionization effects, performance of ISEEM in life testings appeared to be weak.

A large extended Bonner sphere is the other proxy device. Methods have been developed to adjust the configuration of an extended Bonner sphere to approximate the response function of semiconductor devices. To take an example, a Bonner sphere was designed to have a similar response to ISEEM. Monte Carlo simulations predict that the event rate of this sphere is about five orders of magnitude of the rate of ISEEM. Using this sphere, the neutron event rate of ISEEM in atmospheric neutrons can be estimated in a much shorter time.

Contents

List of Figures

List of Tables

List of abbreviations

ANITA - Atmospheric-like Neutrons from thIck TArget

ASER - Accelerated Soft Error Rate

ASTEP - Altitude SEE Test European Platform

CCD - Charge-Coupled Device

CCE - Charge Collection Efficiency

CDS - Correlated Double Sampling

CERN - The European Organization for Nuclear Research

CMOS - Complementary Metal-Oxide-Semiconductor

DRAM - Dynamic Random Access Memory

ECC - Error-Correcting Code

ENDF - Evaluated Neutron Data File

FIFO - First In First Out

FPGA - Field Programmable Gate Array

GEANT4 - GEometry ANd Tracking

GeV - Giga Electronvolt

GRAS - Geant4 Radiation Analysis for Space

IBM - International Business Machines

IEEE - Institute of Electrical and Electronics Engineers

ISA - Industry Standard Architecture

ISEEM - Imaging Single Event Effect Monitor

ITO - Indium-Tin-Oxide

JEDEC - Joint Electron Devices Engineering Council

JENDL - Japanese Evaluated Neutron Data Liberty

LANSCE - Los Alamos Neutron Science Center

LET - Linear Energy Transfer

LOD - Lateral Overflow Drain

PTB - Physikalisch-Technische Bundesanstalt

MCNP - Monte Carlo N-Particle Transport Code

MCNPX - Monte Carlo N-Particle eXtended

MBU - Multiple Bit Upset

MeV - Mega Electronvolt

MSPS - Mega Sample Per Second

NASA - National Aeronautics and Space Administration

NEMUS - the PTB Neutron Multisphere Spectrometer

NUSPA - NUclear SPAllation reaction model

PCI - Peripheral Component Interconnect

PLL - Phase-Locked Loop

PVR - Programable Voltage Reference

QARM - Qinetiq Atmospheric Radiation Model

QMN - The Svedberg Laboratory Quasi-Monoenergetic Neutrons

RAM - Random Access Memory

REM - Roentgen Equivalent Man

RTS - Random Telegraph Signal

SDRAM - Synchronous Dynamic Random Access Memory

SEB - Single Event Burnout

SEMM - Soft Error Monte Carlo Model

SEE - Single Event Effect

SEFI - Single Event Functional Interrupt

SEGR - Single Event Gate Rupture

SEL - Single Event Latchup

SET - Single Event Transient

SEU - Single Event Upset

SHE - Single Event Induced Hard Error

SPI - Serial Peripheral Interface

SRAM - Static Random Access Memory

SRIM - Stopping and Range of Ions in Matter

SSER - System Soft Error Rate

TCAD - Technology Computer-Aided Design

TNS - Transactions on Nuclear Science

TOF - Time Of Flight

TRIM - Transport of Ions in Matter

TSL - The Svedberg Laboratory

USB - Universal Serial Bus

WNR - Weapons Neutron Research

List of symbols

b	b (barn) is a unit of area. One b is defined as $10^{-28}\,\mathrm{m}^2$.
DN	Digital Number, the unit of measuring the charge density in a CCD pixel.
kb	Kilobit, a multiple of the unit bit. One kilobit is 1000 bits.
kB	Kilobyte, a multiple of the unit byte. One kilobyte is 1024 (2^{10}) bytes.
Mb	Megabit, a multiple of the unit byte. One Megabit is 10^6 bits.
MB	Megabyte, a multiple of the unit byte. One Megabyte is 1,024,000 (2^{20}) bytes.

Chapter 1

Introduction

1.1 Discovery of single event effects

In the early 1960s, Wallmark and Marcus[1] published a paper to predict the trend of microelectronics. The minimum feature size was predicted to be approximately 10 µm, which turned out to be wrong later. However, they correctly predicted that cosmic ray direct ionization would upset a circuit when the feature size of microelectronics became small enough. However, this prediction was too far ahead its time. More than one decade elapsed before the technology reached critical circumstances predicted. When this effect was studied by the pioneers at the end of 1970s, there was no accepted term to refer to it. This effect was referred to as "anomalies" by Binder et al. [2] in 1975, "bit errors" by Pickel et al. [3] in 1978, "soft errors" by May et al. [4] and "single event upsets" by Guenzer [5] in 1979. The term "soft errors" and "single event upsets" have been adopted in many later works. JESD89A [6] of the JEDEC standard standardized this effect as SEU (single event upset) . This is one type of single event effects (SEEs), and also the type of main interest in this work. Classifications of different types of SEEs are introduced in section 1.2.

Today, four event mechanisms have been discovered. This section introduces them in the order of the time of discovery. For all these mechanisms, the basic

principle of the effect is that a charged ion strikes an active region of an electronic device and generates a large amount of charge to alter the state of the circuit. A ion dissipates its kinetic energy in matter to release electron-hole pairs. For silicon, on average, every 3.6 eV of kinetic energy can release one electron-hole pair [7]. The four mechanisms are classified by how these charged ions emerge [8].

By the very early 1970s, the main device used in this project, the CCD, was invented in the Bell laboratry [9]. This invention won the Nobel prize in 2009. These devices are essentially large photoactive capacitor matrices which are capable of shifting out the charge packet stored in each capacitor. Unlike many other radiation detectors, a full-frame CCD can time-independently record the charges generated by stopping ions. CCDs were used to study radiation effects on semiconductors shortly after they were invented [10]. More than a dozen works, directly relate to the radiation effects on CCDs, were published in the literature in the second half of the 1970s (e.g. [11–20]). They were used to measure the noise introduced by gamma and ion radiations (e.g. [11–15]), the methods of hardening the devices (e.g. [16, 17]), and the mechanisms of neutron damage in semiconductors (e.g. [18–20]). Reviews of the radiation effects research and developments in the 1970s, as given by Srour [10], remarked that by the end of the 1970s, the CCDs were realized as "an excellent vehicle for studying, characterizing , and understanding certain basic effects of radiation that otherwise would not be observable or observed".

The galactic cosmic ray is the first recognized source of SEE. It originates from outer space, and is composed of energetic particles such as hydrogen (94 %), helium (5 %) , and other heavier ions. Its flux density is shown as a function of ion mass up to ^{58}Ni in Fig. 1.1. Heavier ions than helium have very low flux densityes. Among these heavier ions, carbon (of mass 12) and oxygen (of mass 16) have the largest flux densityes, though they are two orders of magnitude lower than helium. A local peak appears at mass of 56 (mostly iron), its flux density is one order of magnitude lower than carbon.

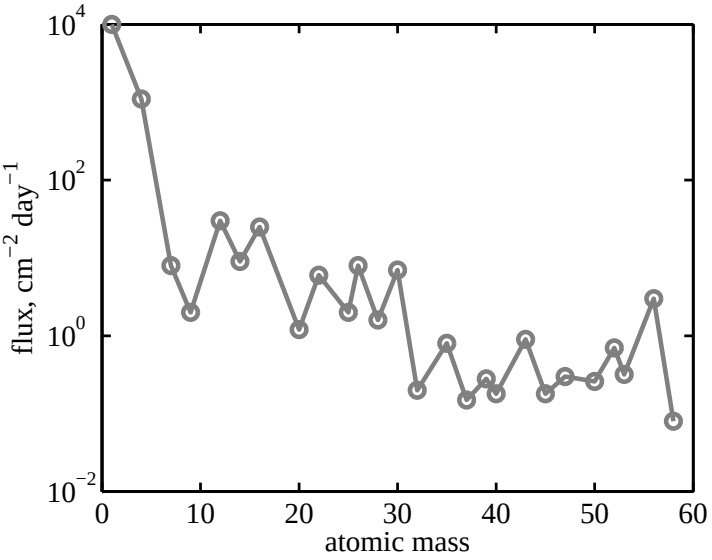

Figure 1.1: Galactic cosmic ray flux density as a function of ion mass, after [21]

A paper entitled "satellite anomalies from galactic cosmic rays" [2] was published in 1975 by Binder et al. They reported the upsets observed in J-K flip-flops in a satellite. To identify the source of the upsets, they used the differential cosmic ray spectra, the range-energy curves, and the mass distribution of the galactic cosmic ray to produce a Linear Energy Transfer (LET)-like spectrum. LET and stopping power are both used to quantify the kinetic energy variations of a charged particle in matter. LET quantifies the energy transferred from the stopping particle to matter. Stopping power quantifies the energy lost by the particle. The authors assumed that a heavy ion, of some LET above a certain threshold, causes an upset. The discrepancy between their prediction and the observation was relatively small (about a factor of 2). This method inspired a great number of later works. Even today, the use of LET spectra to predict the event rate in space is still widespread.

With succeeding technologies, the feature sizes of memory devices continually shrink. As a result, a second source of SEE became significant and was first reported by May et al. [4] in 1979. By the end of the 1970s, Intel built a factory downstream of an abandoned uranium mine. Unaware about that the river was polluted by radioactive contaminations, water from this river was used in product

fabrication. The uranium and thorium isotopes were brought into the products of this factory. These isotopes decay by emitting alpha particles, which can cause SEEs if they hit a sensitive region. The Dynamic Random Access Memories (DRAMs) and CCDs from this factory were found to be highly unstable. The error rate in the DRAMs was very high (about 200 per device per hour). This was a new SEE mechanism as the source of the radiation was not from the galactic cosmic rays in space, but was from the local material. May and Woods reported this upset mechanism [4], and introduced the new term "soft errors" to describe the upsets. Their work indicated that the microelectronic devices can have a critical reliability issue even at sea level. Right after May and Woods's work, Pickel and Blandford published a calculation of the event rate for a 4kb [1] (Random access Memories) RAM in space caused by galactic cosmic ray direct ionization [3]. The results showed that error rate of a total of 96kb of RAM can be up to 0.62 per day. Their work demonstrated that random errors can be found in systems which require high reliability. This work, along with May and Wood's discovery, had a large impact on the community. The concerns then were widely spread.

By the end of the 1970s, another SEE mechanism was discovered. It confirmed that the secondary cosmic rays in the earth's atmosphere can cause SEE.

When the galactic cosmic rays arrive at the upper atmosphere, many interactions occur. New generations of nuclides are produced by nuclear reactions between the incomers and the local atoms, and those then propagate towards the earth as illustrated in Fig 1.2. These processes are known as cosmic ray cascades [7]. Such cascades are mainly engendered by the galactic cosmic ray protons and alphas in the first place, as they are the dominant particles in the GCR flux density and have relatively long ranges in matter, such as the atmosphere.

The flux density of the secondary cosmic ray in the atmosphere is shown as a function of altitude in Fig 1.3. The data for this figure were extracted from

[1] kb, kilobit

the QinetiQ Atmospheric Radiation Model (QARM) website example 6 [22–24]. It can be seen that at the edge of the atmosphere, the flux density of cosmic rays increases as the cascades grow towards the earth, and reaches a peak at the altitude of about 18 km. With further decrease in altitude, the air becomes denser, and the flux density drops rapidly below 18 km. It seems that the shielding effect of the atmosphere is more significant than the particle production effect in that region. Neutron and proton flux density are similar in quantity at the top of the atmosphere. With the decrease of altitude, the flux density of neutrons becomes higher than the flux density of protons. At sea level, the flux density of neutrons is about 15 times higher than the flux density of protons.

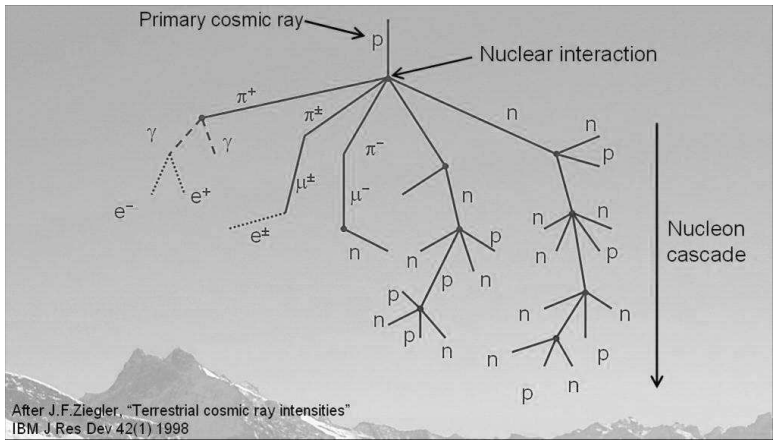

Figure 1.2: Cosmic Cascade

Ziegler and Lanford, who suspected that cosmic rays in the atmosphere can also cause soft errors, published a paper in Science in 1979 [7]. This paper was the first detailed analysis of the soft error mechanisms induced by particles other than energetic heavy ions. They had evaluated the interactions of electrons, protons, neutrons and muons with silicon. Their work showed that electrons and muons have very weak interaction with silicon, therefore they couldn't produce enough charge to upset memory devices. Energetic hadrons which are the neutrons, protons and pions, may have strong interactions with silicon. Therefore they are capable of causing SEE. Neutrons are the dominant hadron below the flight altitude (about 20km) as indicated by Fig. 1.3, which makes neutrons the main

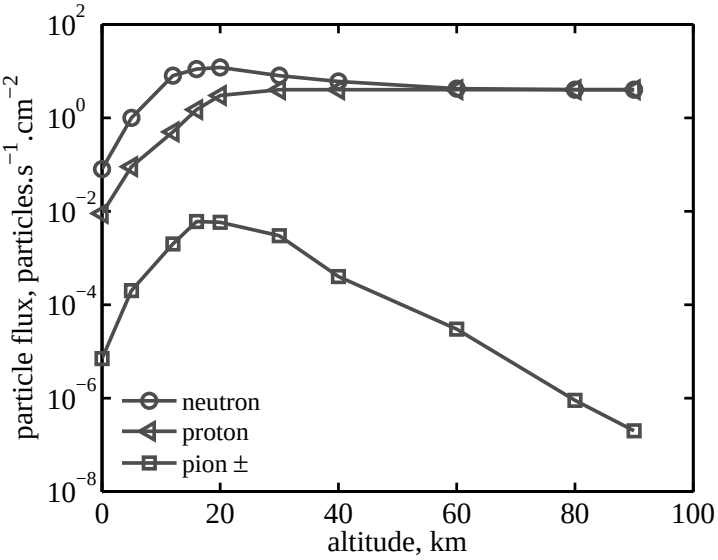

Figure 1.3: Cosmic ray flux density against the altitude, after the QARM [24, 25] website example 6

concern of the soft errors.

The first experimental evidence of the errors caused by protons and neutrons were reported by Guenzer et al. with 1979 [5]. They tested some memory devices in 6.5 MeV to 14 MeV neutrons and 32 MeV protons. The authors proposed that the effect was caused by the alpha particles created by a (n, α) or (p, α) or similar nuclear reaction. The term "single event upset" was first introduced in this paper. As the upset is caused by a single incident particle, it is so called a "single event".

From the 1980s to the early of 1990s, the alpha contamination problem was the major research topic of SEE [26]. This effect was reduced significantly after its discovery. One way of reducing this effect is using extremely high purity materials. The alpha particle emitting rate was reduced by a factor of more than 10^5 times [27]. Methods were also developed to prevent the alpha particles reaching the sensitive volume by coating the volume with thick enough materials. As devices scaled down, secondary neutrons became the main source of SEE at flight altitude [28]. Neutron induced SEEs became one of the major research topics of SEE from then to today.

The latest event mechanism was first reported on those devices doped with boron in the substrates in 1986 [29]. ^{10}B emits an alpha particle and a ^{7}Li after capture of a thermal neutron. Up to 2.8 MeV energy in total can be released. Fig. 1.4 illustrates the cross-sections of (n,α) reactions for ^{10}B and ^{28}Si. ^{10}B shows a large cross section of interacting with neutrons. The integrated cross-section of ^{10}B(n,α) below 2MeV is more than 4 orders of magnitude higher than the cross-section of ^{28}Si(n,α). Since a small volume of boron is used in semiconductors, the overall geometry cross section of boron against silicon may not be as significant as the material cross-sections.

Even though the disadvantages of using ^{10}B in devices are clear, it didn't stop the manufacturers using it to achieve lower manufacturing costs. By the mid-90s, memory containing borophosphosilicate glass (BPSG) were the most favoured products on the market. Then Baumann alerted the community to the risks of using memories that contain ^{10}B [30]. In 2002, Kobayashi et al. [31] gave experimental evaluations of the three sources of the single event upsets on some 0.18μm and 0.25μm feature size SRAM; and the results showed that the thermal neutrons contributed 74% of the events, which is about three times the events caused by cosmic neutrons. Alpha particle contaminations contributed 1% of the events. However, the weights of the sources are strongly dependent on the designs, as Armani et al. addressed more recently in [32]: the sensitivity of the SRAMs, with the same feature size, to thermal neutrons can vary more than one order of magnitude.

1.2 Types of SEEs and the type of interest in this work

The types of SEEs are well defined in the JEDEC JESD89A standard [6]. They generally fall into to the categories of "hard error" and "soft error". Hard errors refer to those errors which are associated with permanent damage. Soft errors

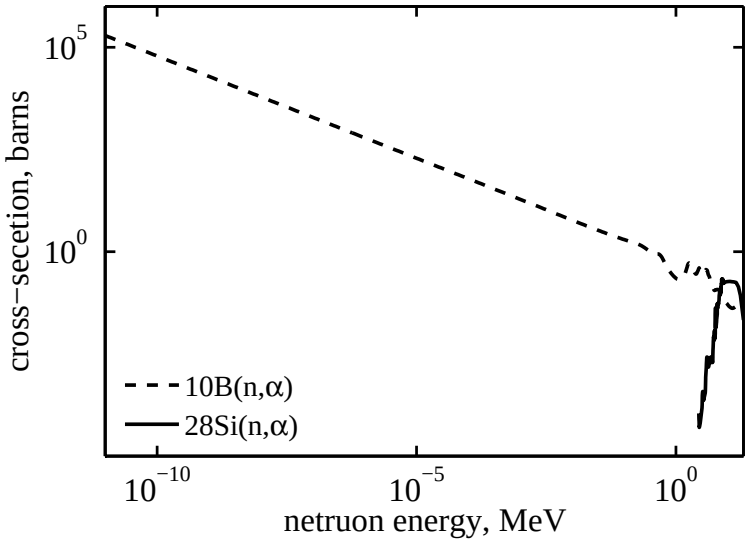

Figure 1.4: ^{10}B(n,α) and ^{28}Si (n,α) cross-sections, data are from ENDF/B-VII.0

are those errors that can be recovered by re-initialization or sometimes a hard reset [6]. Common soft errors in memories are single event upset (SEU), multi-bit upset (MBU).

SEU is a latched logic state alteration in digital circuits. The term was first introduced by Guenzer [5] after he observed bit upsets of a SRAM in neutron and proton beams. This type of error can be detected and corrected by the circuitry in some high demand applications, such as the Error-Correcting Code (ECC) memory, which is commonly used in network severs.

MBU is a soft error involving multiple adjacent bits. Such events are often observed in a small feature size device, where the adjacent cells are close to each other. The short-range heavy ions can hit several cells before they stop. This type of error is more difficult to correct, and is becoming more significant, because of shrinking feather sizes which makes the cells closer to each other.

SET is the transient current pulse generated by incident particle in a linear or combinational circuit. The width of the pulse is strongly depends on the particle LET and the device technology. Such pulses would be attenuated when propagating through the paths in a device. A SET could be latched and cause an SEU [33]. This error is becoming more and more important in advanced memory

devices, because of the trend to faster bus speeds.

SEU is the main type of interest in this project. In CCDs, the radiation induced charge transients can be recorded as charge packages. The event charge packages are essentially the results of SET effect. Applying a certain threshold, such transients could be considered as SEUs, to simulate the analogous effects in the memory devices.

1.3 Standard methods of characterizing SEE in memory devices

JESD89A [6] standardized two methods of measuring soft errors, the SSER (System Soft Error Rate) and ASER (Accelerated Soft Error Rate) testings.

SSER is the measured devices' real time event rate, when operating directly in a natural radiation environment. This type of testing provides the most accurate results, because no extrapolation or assumption is made. Since the neutron flux density in the atmosphere is very low, this type of testing often uses a large number of devices to increase the effective event rate. It usually needs millions of device hours to reduce the statistical error. Such requirements usually make SSER testings very expensive, especially when it takes place at a remote location (such as mountain top). The event rate in the natural environment is extremely low. For example, Autran et al. [34] placed 3.6Gb [2] of 0.13 μm feature size SRAM at the Altitude SEE Test European Platform (ASTEP) for about half a year. They observed only 44 events.

To reduce the cost and time to test a certain type of device, ASER testing is often employed. In such testing, a device is exposed to an intense beam of particle to accelerate the event rate. The neutron fluence in this type of testing is measured by facility beam monitors. The accuracy of the beam monitors is the main error source in this type of measurement. (as discussed in section

[2] Gb, giga bit

2.6). White neutron sources have similar neutron energy spectra to that of the natural cosmic neutrons. Therefore they are, in particular, used to simulate device responses in the atmosphere. Such beams are produced using energetic protons to bombard a metal target, and have a wide energy range (from thermal up to several hundreds MeV). Fig. 1.5 compares the neutron spectrum of Weapons Neutron Research (WNR) facility in the Los Alamos Neutron Science Center (LANSCE) and the atmospheric neutron spectrum predicted by JESD89A. The radiation intensity at LANSCE is about 8 orders of magnitude greater than that of the atmospheric neutron radiation. However, the LANSCE spectrum shows a lower cut-off energy at the high energy end, and small discrepancies in the shape of the spectra. The most energetic neutrons are a very small part in the overall neutrons. The lower cut-off energy effect is often neglected. The discrepancies of the shape may lead to considerable error. Kobayashi et al [35] have noted that such discrepancies could lead up to 25% difference in results of ASER and SSER.

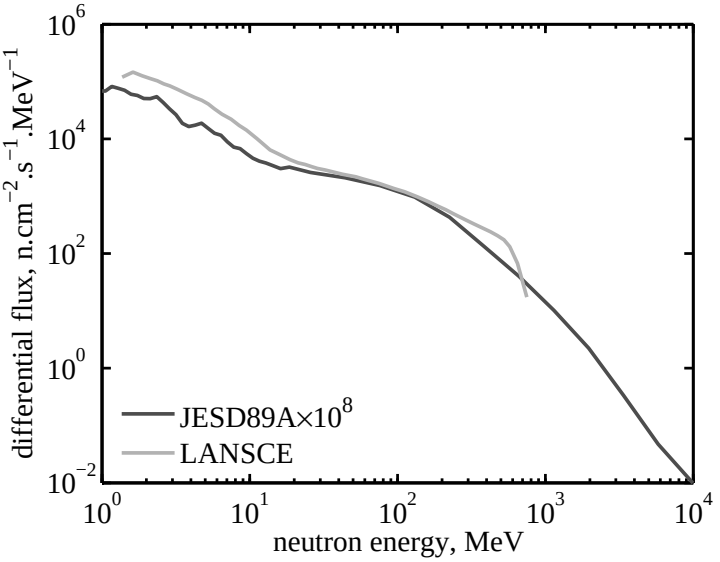

Figure 1.5: Neutron spectra

The neutron flux densityes at the testing sites are usually predicted by models, for example, the JESD89A model [6] and QARM [24, 25]. Errors in such models will be introduced to the final ASER prediction. This effect is introduced in section 1.3.1, which also discusses some benchmarking testing to evaluate ASER

testings in recent years.

1.3.1 A brief review of the state-of-art SEE life testings

Measurements of SSER in some devices have been undertaken by several researchers in recent years [34–37], they measure these rates at different locations to validate ASER and/or verify the neutron flux density predicted by models. SRAM based devices were used as sensitive elements in all these studies.

Kobayashi et al. [35] reported a large discrepancy between the ASER and SSER for a 0.18 μm feature size SRAM in 2004. The measured ASER and SSER were 7800FIT/Mb (failures in time per mega bit)[3] and 3000FIT/Mb, respectively. The authors analyzed all possible error sources and suspected that the neutron flux density prediction at the location of their experiment had an error up to a factor of 2.

The Rosetta experiment [36] of Xilinx compared ASER from several different locations. Comparing the predictions of JESD89, the discrepancy is in the range of -34% to 47%.

Autran et al. [34] has reported surprisingly good agreements of the event rate predicted by ASER at TRIUMF (within 10%) for 130nm feature size CMOS SRAMs in 2007. Later in 2009, they reported [37] a 30% discrepancy for 65nm feature size CMOS SRAMs between the ASER at LANSCE and the SSER at the same location as where they did their previous experiment. These two measurements at ASTEP demonstrated that the errors of ASER predictions of different devices at the same location are not consistent.

A few characteristics of state-of-art devices could be found in these three studies. Firstly, alpha particle induced soft errors still exist in today's devices. Secondly, the devices that have strong incident angular dependency could introduce discrepancy between the accelerated testings and life testings. For example, in the Rosetta experiment of Xilinx [36], the cross-section of FPGAs at 180° in-

[3] the number of failures per 10^9 device-hours per mega bit

cident angle is known to be twice as high as the event rate at 0° incident angle. Since the neutron incident angles in the atmosphere are difficult to predict, it's hard to correct for the influence of this effect. Finally, the neutron flux density uncertainty in the atmosphere is the major error source of SSER.

Several conclusions for the memory devices' SSER testings can be drawn. The memory devices have very low event rate, even at high altitude laboratories. A large amount of space, power, and maintenance are needed to keep devices operating. Also strong incident angular responses of devices can introduce considerable errors to the final results. Such errors are usually difficult to correct.

1.4 Measuring atmospheric neutrons using gaseous counters

There are many instruments that can be used to measure the neutron spectrum in the atmosphere. Gaseous counters are popularly employed. [38] These sensors utilize a certain reaction to detect neutrons. ^{3}He and BF_3 thermal neutron counters are are discussed below.

BF_3 counters utilize the reaction

$$^{10}B + n \rightarrow {}^{7}Li + {}^{4}He + Q$$

Q is the released energy in this reaction. Fig. 1.4 shows the cross-section curve of ^{10}B in the energy range from 1×10^{-12} MeV to 20 MeV. The cross section curve follows a 1/v relationship[4] up to about 0.1 MeV. Q is 2.31 MeV 93% of the time, when the lithium nuclide is left in its first excited state. 7% of the time the lithium nuclide is left in its ground state, and Q is 2.79 MeV.

^{3}He counters utilize the reaction below to detect thermal neutrons.

$$^{3}He + n \rightarrow {}^{3}H + {}^{1}H + Q\,(0.764MeV)$$

[4] v is the neutron velocity

The cross-section curve of this reaction is similar to the ^{10}B(n,α) reaction. Its cross section curve follows a 1/v relationship up to about 0.2 MeV. The cross-section at thermal energy (i.e. 0.025 eV) is 5330 b. Compared to the 3840 b of ^{10}B(n,α) reaction at this energy, ^{3}He has 40% higher cross-section to detect thermal neutron. Therefore, ^{3}He counters are commonly used in low flux density environments. All the neutron spectrum measurements in the atmosphere introduced in section 1.5, below, used ^{3}He counters.

^{3}He counters are widely used in two types of instruments, the standard neutron monitor NM64 [39] and Bonner sphere spectrometers [40].

The standard neutron monitors form a global network to measure neutrons. Measured data from a large number of stations are openly available on the Internet. However, the response of such monitors to neutrons is proportional to neutron energy from 10 MeV to 100 GeV [39], which is very different from semiconductor response to neutrons. Neutrons above about 1 MeV can induce SEE in semiconductors, and such response is typically saturated at the energy on the orders of 10 MeV. A notable feature of the neutron monitors is that they have a very large size, therefore have a large geometrical cross-section. The neutron monitor at the Altitude SEE Test European Platform (ASTEP) [34] has about 10 events every second.

In the natural environment, the Bonner sphere spectrometer is widely used [38]. A Bonner sphere spectrometer consists a set of Bonner spheres in different sizes. Different size spheres have a peak response at different energies. (see Table 6.2 for example) Response functions of the spheres can form a response matrix. After exposing the spheres to the same neutron field simultaneously, individual counts can be unfolded according to the response matrix to obtain the neutron spectrum. This type of spectrometer was first described in 1960 [40]. They have very good energy range, good sensitivity, and isotropic angular response. But the energy resolution is poor, and the processes of unfolding a spectrum is complex [38].

A cylindrical scintillator was used in the initial design of the Bonner sphere [40].

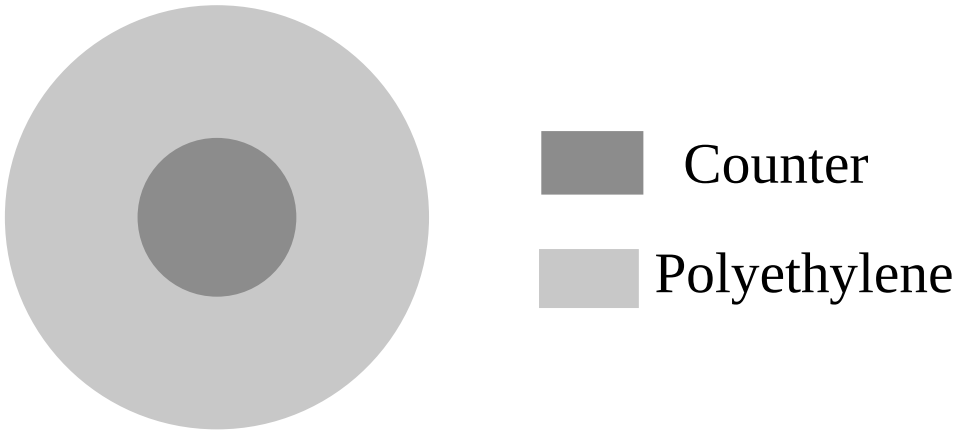

Figure 1.6: Example Bonner sphere geometry (not to scale)

In the 1980s and early 1990s, spherical ^{3}He counters, produced by Centronic Ltd., UK, have been used as the sensor of Bonner spheres [38]. A Bonner sphere spectrometer can be used in accelerated neutron fields [41, 42]. In that case, passive detectors (e.g. gold foil) are used as the sensitive element, because active detectors (e.g. ^{3}He counters) are too sensitive, high flux density neutrons can induce serious event pile-up.

An example geometry is shown in Fig. 1.6. There is a thermal neutron sensor placed in the center of the sphere. It could be gas filled counter, activation foil, or scintillator [43]. Pure polyethylene surrounds the sensor to moderate the incoming neutrons. The thickness of that moderator can be adjusted to make the peak response appear at different energies. The conventional Bonner sphere has a very weak response to high energy neutrons. To increase the high energy response, high-Z materials have been purposed to be added to the spheres by Hsu et al.[44]. Such spheres are so called "extended Bonner spheres". The mechanism of improved response is to utilize the (n,xn) reaction of high Z materials at high energy.

Generally, a set of varied size Bonner spheres are involved to measure a neutron spectrum. As different sizes of the spheres have peak responses at different energies, the actual neutron spectra can be obtained by unfolding the counts using individual response functions. This process is generally considered as the

source of the most significant potential error [38], because the response functions are from simulations, and there is no standard procedure for the calculation. It has been observed that most of the calculations of the response functions are based on MCNP and MCNPX (e.g. [44–48]). Possibly, as the results are strongly affected by the hadron models used in the simulation code, most work in the literature sticks to the same model in the same toolkit to obtain consistency with other work.

To study the performance of Bonner sphere spectrometers, a literature study has been performed.

Tommasino et al. [49] described the neutron spectrum measurement at flight altitudes by a passive multidetector stack spectrometer [50]. This stack utilize the fission reactions of neutrons with materials (e.g. uranium, thorium, and bismuth) to detect neutrons. When they compared this spectrum with the one measured by Goldhagen et al. [46] using Bonner spheres, they found a neutron flux density peak at 300 MeV instead of at 100 MeV in the spectrum measured by the Bonner sphere spectrometer. The authors suggested that this discrepancy may be caused by the inaccurate cross-sections used in both of the studies. This statement seems convincing. The cross-section data files are released by different organizations and made available through data files, such as the Evaluated Nuclear Data File (ENDF) [51], Japanese Evaluated Nuclear Data Library (JENDL) [52], and others (e.g. [53–55]). Nuclear processes for neutrons up to 20 MeV are well established in those files. Many Monte Carlo simulation codes use the tabulated data from the data files. (a short review of Monte Carlo simulation toolkits is in section 2.2) Above 20 MeV, the cross-sections in a simulation are mainly from nuclear models. Predictions from the models may have large discrepancies with the reality. However, data from the evaluated neutron data files may not all be as accurate as they would be in ideal case. Sometimes, discrepancies can be observed when comparing the neutron total cross-section of an isotope given by two different organizations. For example, Fig. 1.7 compared neutron total

reaction cross-section in ^{202}Pb from the latest version of ENDF and JENDL. The cross-section in ENDF is about 10% higher than that in JENDL.

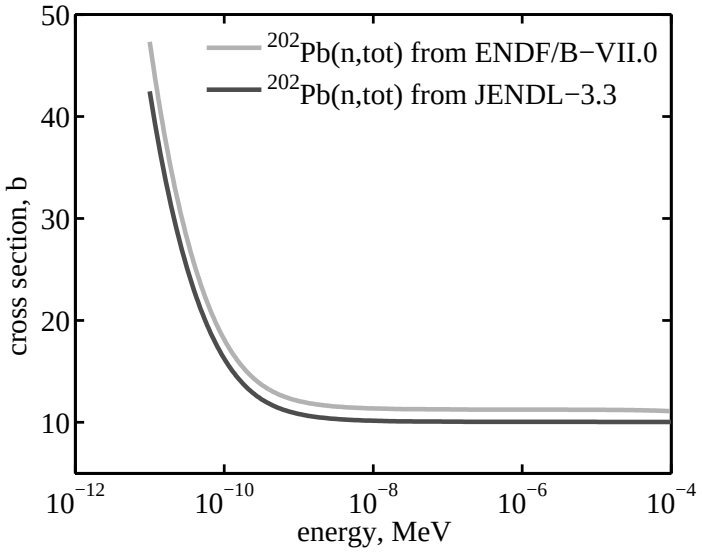

Figure 1.7: Discrepancy in evaluated neutron data files

Today, neutrons in atmosphere are still not understood very well. Indicated by Ziegler's review [56], the measured neutron spectra have large discrepancies with each other. Different instruments used in those measurements may be the main factor causing the large discrepancies. At the present time, the spectrum measured by Bonner sphere spectrometers is the most trusted. The shape of the spectrum measured [48] in New York City has been standardized in JEDEC JESD89A[6] as the shape of the spectrum in the atmosphere. Also it agrees with the shapes predicted by some Monte Carlo simulations. (e.g. QARM) The spectra measured by Bonner spheres rely on the response matrix, which also is given by Monte Carlo simulations. Therefore, it is no surprise that those shapes agreed. Because they all derived from simulation, and the major nuclear processes of the primary neutron cascades in the atmosphere and the neutron propagation in a Bonner sphere are actually the same. They are spallation reactions and elastic scattering. An extended Bonner sphere can be considered as an analog of the atmosphere, of which cross-sections are significantly biased. However, using other mechanisms to detect neutrons (such as TOF, and fission reactions

discussed above) may give different results.

The inaccuracy of neutron spectra is the main concern for calculating the real-time event rate of a memory device in standard ASER testing. In this work, an alternative method of estimating the real-time event rate is proposed to avoid the influence to the spectra inaccuracy.

1.5 Notable neutron spectrum measurements in the atmosphere

Two sets of Bonner spheres have been involved in many secondary neutron spectrum measurements. One is the de facto Japan standard Bonner spheres [45] and the other one is that used in the National Aeronautics and Space Administration's (NASA) ER-2 project [46, 47]. Three aspects are common. Firstly, a 5.1cm diameter ^{3}He counter is used as the sensitive element in each sphere. Secondly, their response matrixes are calculated by MCNP or MCNPX. Finally, they all contain extended Bonner spheres, which can extend the measured energy range.

There are 6 different size spheres, from 5.1cm (bare ^{3}He counter) to 23cm, in the Japanese spectrometer. While the NASA's ER-2 project intended to utilized 14 spheres from 5.1cm (bare ^{3}He counter) to 38.1cm (about 15 inch). The two largest spheres out of the 14 spheres are loaded with high-Z materials to enhance the response to high energy neutrons as suggested by Hsu et al. [44]. Since the ER-2 project used more spheres, the spectrometer in that project may have better energy resolution than the resolution of the Japanese spectrometer. However, they take more space. This factor may limit the usage of this spectrometer. Two out of fourteen spheres did not fly in the ER-2 project due to the space constraints. [46]

The notable measurements in 1990s are the NASA ER-2 program and the life testing at New York as measured by International Business Machines (IBM). NASA's ER-2 program [46, 47] is a multi-purpose program that was undertaken

in 1990s. One of the aims of this program is to characterize the dosage of atmospheric cosmic radiation to air crews. The Bonner sphere spectrometer was intensively flown by the ER-2 High Altitude Airborne Science Aircraft [57]. In the experiment, the aircraft was typically operating at 65,000 feet (19.8km) altitude, where there is the peak neutron flux density in the atmosphere. Those measurements have provided valuable scientific data to many other projects. For instance, the data have been used to verify the predictions of QARM [24]. Useful conclusions were given by Goldhagen et al. [46, 47]. At high altitude, geomagnetic latitude has very little effect on the shape of the spectrum, but it strongly affects the flux density. The shape of the spectrum varies only slightly at high altitude (20km to 12km). But there is a significant difference at sea level. Three peaks (at 10^{-8} MeV, 1 MeV, and 100 MeV) are observed in the spectrum at sea level. However, the thermal neutron peak is not observed at high altitude.

This spectrometer was later deployed at the IBM T. J.Watson Research Center for 10 months to measure the neutron spectrum at New York. [48] The measured spectrum has later become part of the JEDEC JESD89A standard. Spectra of five other locations have also been measured by Gordon to compare with the New York spectrum.

In the first decade of the 21st century, many experiments in Japan [58, 59] and Germany [60, 61] have also used Bonner sphere spectrometers to measure atmospheric neutron spectra. Nakamura et al. [58] and Kowatar et al. [59] have measured the spectra in Japan. The main strategy of their work has been to undertake measurements at sereral different altitudes on a mountain (e.g. Fuji), and to compare the neutron spectra and the equivalent dose [5] delivered by neutrons. The neutron spectra at different altitudes of a mountain were found to have a similar shape to each other closely.

The flux density in the atmosphere also affects by other factors, especially

[5] In the unit of Gray. One gray is the absorption of one joule of energy, in the form of ionizing radiation, by one kilogram of matter.

latitude and solar activities. Generally, the flux density in a higher latitude location is higher than the flux density in a location of lower latitude [6]. The solar activities can affect the flux density in a location by up to a factor of two [6].

The PTB NEutron MUltisphere Spectrometer (NEMUS) of Wiegel and Alevra [60, 61] is an extended Bonner sphere spectrometer which consists of 16 spheres from 3 inch to 18 inch diameter. Four out of these 16 spheres were loaded with high Z-materials to enhance the response at high energy. This spectrometer was tested in monoenergetic neutron beams from 1.2 keV to 19 MeV, and in a 60 MeV quasi-monoenergetic neutron source. The conventional Bonner spheres were calibrated in the neutron beams below 14.8 MeV. The average errors of the measured and calculated response of the individual spheres agreed within $\pm 2\%$. They used MCNPX to simulate the response. This good agreement demonstrated that MCNPX can accurately model the neutron moderation and the ^{3}He interactions with thermal neutrons. The extended Bonner spheres were calibrated in the 60 MeV quasi-monoenergetic neutron source. The calculations overestimated the measurement by about 5%.

A battery-powered version of this spectrometer was also briefly introduced in [61]. Relying on four C-sized batteries, this system can operate for 7 days. This feature makes measurements at remote locations very convenient.

1.6 Project objectives and brief introduction

The main objective of this work is to investigate the use of proxy devices, which have neutron response functions similar to some of memory devices, to characterize the influence of neutron fields in causing SEUs. The proxy devices can be used in accelerated beams and more importantly in natural environments. A methodology has been developed to estimate the real-time event rate as an alternative method to that of the standard ASER testing [6].

In the following section, the standard accelerated method used to estimate

device real-time event rate (the ASER (Accelerated Soft Error Rate) testing) [6] is referred to as the direct method. The method of using a proxy device is referred to as the indirect method. They are both accelerated methods and need, to use an accelerated beam.

The real-time event rate of a device, R, is calculated by

$$R = \int \sigma(E)\varphi(E)\, dE \tag{1.1}$$

where σ is the detector response function, φ is the neutron flux density (e.g. in the atmosphere). To avoid the expensive SSER testing. R is normally estimated by the accelerated testings. To simplify the work, one hypothesis is made. This is that the shapes of the neutron spectra in an accelerated beam and in the atmosphere are identical. This hypothesis is almost true if the accelerated testing takes place in a white neutron beam, such as that of LANSCE, TRIUMF and Atmospheric-like Neutrons from thIck TArget (ANITA). Then Equ. 1.1 is simplified as

$$R = \sigma\varphi \tag{1.2}$$

where σ is the overall cross-section, and φ is the integrated flux density. σ can be calculated as dividing the observed event count by the neutron fluence of the beam, and φ at the location of interest can be obtained by models or even measured by spectrometers. However, if the accelerated beam is not broadly similar to the atmospheric neutron field, the calculation of event rate should strictly use Equ. 1.1. In that case, the device needs to be characterized by the monoenergetic or quasi-monoenergetic neutron beams, or high energy proton beams to measure the cross-section at certain energies. The response function is obtained by curve fitting to the measured points.

In the indirect method, the proxy device is tested together with the sample memory device in a beam, and then the proxy device is placed at the location of interest. The event rate of the memory device in life testing, R_{M_l}, can be

predicted by

$$R_{M_l} = \frac{R_{M_a} R_{P_l}}{R_{P_a}} = \frac{R_{P_l}}{H} \tag{1.3}$$

where R_{M_a} and R_{P_a} are the measured event rates of the memory device and the proxy device in an accelerated neutron beam, R_{P_l} is the measured event rate of the proxy device in life testing, and H is the response enhancement factor. In contrast with the direct method, the indirect method hypothesizes that the shape of the memory device's response function is identical to the one of proxy device's. A event in the proxy devices could be a pulse, which exceeds a certain height, in a gaseous counter, or a group of pixels, which is brighter than a certain intensity, in a CCD . Those thresholds should be chosen to make the response function of the proxy device broadly similar to the response function of the device of interest.

As the hypotheses of these two methods are different, they treat the neutron spectra and device response functions differently.

The direct method needs to compare the neutron flux density in the atmosphere and the artificial beam. At the present time, there may be no method to do this which is good enough. (see the comparisons of the measured neutron spectra in section 1.5) Even though the absolute flux density in the atmosphere and artificial beams are known, there still are difficulties. For example, because a device usually has different cross-sections in different white beams. (e.g. [62, 63]), it's difficult to justify which cross-section is the closest one to the cross-section of this device in the atmospheric neutron field.

The indirect method needs to compare device response functions. This can be done by means of simulation, or simply testing the device of interest and the proxy device in the same beam. The response enhancement factor can be measured in a white beam. Agreement of the shapes can be evaluated in monoenergetic beams or high energy proton beams.

For a better performance, it is preferred that the proxy device has an isotropic response to neutron incident angles, as neutrons strike devices with random angles in the atmosphere. If the proxy device has an isotropic response to neutrons, the

angular effects of a memory device can be easily characterized by rotating it in the accelerated testing. One disadvantage of the indirect method is that it requires the life testing of the proxy device. In some cases, that may be difficult (e.g. at remote locations). To summarize, the ideal proxy devices should

- have similar response to neutrons as that of SEE in devices of interest
- have high event rates in natural environments
- be portable
- have isotropic response to the neutron incident angle

The Imaging Single Event Effects Monitor (ISEEM) and large extended Bonner spheres are the proxy devices studied in this work.

The ISEEM was originally developed by Z. Török and his co-workers. [64] A CCD was used as the sensitive element in this instrument. It has been taken to many well defined neutron facilities to calibrate. It has also been deployed to a high altitude laboratory (Jungfraujoch) to perform a SSER testing. A large amount of experimental data have been accumulated using ISEEM before the start of this work. The testing facilities include the Los-Alamos Neutron Science Center (LANSCE) [65–67], the The Svedberg Laboratory (TSL) (Quasi-Monoenergetic Neutrons) QMN [68, 69], and the Tri-University Meson Facility (TRIUMF) [70] The development of ISEEM and measured data analysis were previously published in [62, 71–73]. Török was awarded a PhD degree for his development of ISEEM. His work focused on developing the software and hardware, and comparing the measured data from different facilities to analyze the characteristics of individual beams. But no model was developed to analyze the detail event mechanisms (e.g. a microdosimetry model, or TCAD model of the sensor). His work provided an excellent instrument for this work. A CCD has similar characteristics to those of memory devices, because they are all semiconductor devices. Therefore ISEEM was evaluated in this work as a proxy device. During this work, the newly available beam TSL ANITA [74] was measured, and ISEEM has been deployed to ASTEP [34] for a six months life testing.

The analyzed results have indicated that ISEEM has excellent performance for benchmarking different accelerated beams; but it sufferers from alpha contamination and low energy proton direct ionization in natural environments. Therefore, it is not an ideal candidate for the proxy.

Large extended Bonner spheres are the other proxy devices studied in this work. Monte Carlo simulations were employed to evaluate different design parameters of an extended Bonner sphere to approximate the response function of semiconductor devices. It has been found that extended Bonner spheres have a near constant event rate enhancement of the rate of ISEEM, even in very different accelerated fields (such as TSL 180MeV and LANSCE). This instrument shows better performance than ISEEM in the natural environment, because it has much higher detection efficiency, and it is not affected by alpha contamination or proton direct ionization.

1.7 Introduction of the thesis

The rest of the thesis is divided into six chapters.

Chapter 2 introduces the Monte Carlo simulation of neutron interactions in the CCD (type KAF-0402E). GEANT4 [75, 76] was chosen for use. A literature study was performed to assess its performance comparing with other similar simulation toolkits. Then the correctness of using this toolkit was verified by simulating the pulse height spectrum of a diode, of which the design parameters and measurement results were known. Followed by that, the methods to construct the CCD model and estimate the effective depth of the sensitive region are introduced. This model simplifies the CCD response to charged ions to the extreme by assuming all charges generated in specified regions are collected, and none from elsewhere. The simulated charge collection spectra at different neutron beams agreed closely with measurements, which suggested that the species and energies of the secondaries were correctly modelled. The origins of charged particles and

the event contributions of each device components were further explored. The simulated event cross sections were found have a relatively large discrepancies with the measurements (up to a factor of 2.6). Most likely, the simplification of CCD response is the main error source. The investigation of charge collection behavious in the CCD leads to the work presented in Chapter 3.

Chapter 3 introduces the work to characterize the CCD response to charged ions. This chapter starts with a short review of the charge diffusion models in the literature, and identifies a suitable model for this application. The critical design parameters of CCD KAF-1401E were known. Therefore, this CCD was simulated using the GEANT4 and diffusion models. The simulated cross-sections agreed with measurements better than 30% in all cases. This discrepancy is within the error quoted by the facilities.

Chapter 4 analyzes the ISEEM performance in natural environments. The different experimental conditions of accelerated and life testing are discussed, and corresponding effects were analyzed. ISEEM's life and accelerated testings were compared. Final results indicated that ISEEM has a good performance in high flux density beams, and poor performance in natural environments.

Chapter 5 describes the software and hardware developments to improve the performance of ISEEM.

Chapter 6 introduces the methods of adjusting the response function of an extended Bonner sphere [40, 44] to match the shape of the function of an electronic device. To take an example, a sphere was designed to have a similar shape of response function to that of ISEEM. Monte Carlo simulations indicated the event rate enhancement (on the orders of 10^5) of this Bonner sphere against ISEEM is almost a constant at the neutron fields defined at JESD89A, TSL, ANITA, TRIUMF and LANSCE. This result shows the good agreement of their response shapes.

Chapter 7 summaries the knowledge acquired in this work, and discusses future work.

Chapter 2

The nuclear interactions of neutrons and CCDs

Chapter 2 and 3 introduce the simulations of ISEEM responses to neutrons. Chapter 2 focuses on analyzing the nuclear interactions. A model was therefore developed using the GEANT4 toolkit [75, 76]. Secondary species and their origins were analysed. The record of particle energy deposition in the CCD active regions is worked together with a simple charge collection model to generate a charge collection spectrum in terms of shape. Simulated spectra on all test sites agreed with those from measurements. However, event cross-sections were overestimated by up to a factor of 2.4. Chapter 3 introduces the work of modelling the CCD response to charged secondary particles. This model was coupled with the preliminary GEANT4 model. Event cross-sections predicted by this new model have a discrepancy of 30% with our measurements. This discrepancy is within the error quoted by the facilities.

A preliminary CCD model was developed to analyse the basic event mechanisms. This model used alpha particle responses (measured by Dunne [77]) to study the charge collection behaviours of a CCD. Monoenergetic neutrons from 1 MeV to 9 GeV along with five complex neutron fields were simulated with this model. The simulated and measured charge collection spectra agree closely. They

are described in section 2.5.4 and analysed in section 2.6.

This chapter starts with the justifications of the used tools and methods, and followed by the results and discussion.

2.1 Introduction of calculations for neutron induced SEUs

Complementary with experimental studies, simulation has emerged as an important aid to understand single event effects. Monte Carlo simulation is a widely used approach to simulate the complex events. In this type of simulation, statistical characteristics of events can be studied given three types of information: the nuclear data (secondaries energy and angular distributions), device geometry, and the charge collection behaviour of the sensitive element.

The nuclear data are an essential part of the simulation. These data are either measured from experiments or calculated from nuclear reaction models. Neutron interactions with matter have been intensively measured below 20 MeV [51]. The data were later evaluated and released in the evaluated neutron data file. Section 1.4 introduced the evaluated neutron data files. GEANT4 provides a model which can be used to simulate neutron-hadron interactions with matter below 20 MeV. It is a data driven model, based on a mixture of ENDF and JENDL, and is called the "high precision" model (G4HPNeutron). Even though many measurements for the neutrons above 20 MeV have taken place, because of the wide range of energies, they are not yet complete. Therefore theoretical nuclear models are usually used to model neutrons with energies above 20 MeV.

The devices' materials strongly affect the productions of secondaries in a semiconductor device. (In some cases, geometries may also affect the production of secondaries, for example, the extended Bonner spheres introduced in section 6.3.) They are generally easy to obtain for the large instruments, such as gas filled counters. By comparison, the detailed design of commercial microelectronics are

microscopic and confidential. They are often one of the main source of uncertainty, as for instance in this project.

The model of charge collection behaviour is the bridge to connect the passage of charged particles in the sensitive region to the measured response. For semiconductor sensors, this kind of model could be accurately characterized by Technology Computer Aided Design (TCAD) tools (e.g. Minimos [78]). However, TCAD calculations are generally time consuming, therefore not the best choice for a mass event simulation. The charge collection behaviours are usually simplified by making assumptions. One of the simplest assumptions is that the charges generated in a certain region were collected, and none were collected from elsewhere.

All three prerequisites of an SEU calculation can be found in an SEU calculation code. Take the first 3D SEU simulation program "Soft Error Monte Carlo Modeling" (SEMM) [79] developed by IBM in the 1980s for example. It has been developed for simulating bipolar devices. Device geometry can be modelled with large number of cubes, as shown in Fig.2.1. This code used the NUclear SPAllation (NUSPA) reaction model [80] to generate the event secondaries. However, only some typical heavy recoils (such as He) of the secondaries can be tracked. A device volume is modelled with a large number of cubes. The characters at the top surface of each cube indicate different devices, and the cubes in 3D represent different region in a sensitive region. The regions marked by the same character have the some physical properties. It simplifies the devices' charge collection behaviours by the popular assumption mentioned earlier.

2.2 A brief review of candidate Monte Carlo toolkits

GEANT4 [75, 76] is a Monte Carlo toolkit developed by the European Organization for Nuclear Research (CERN) for simulation of the passage of particles

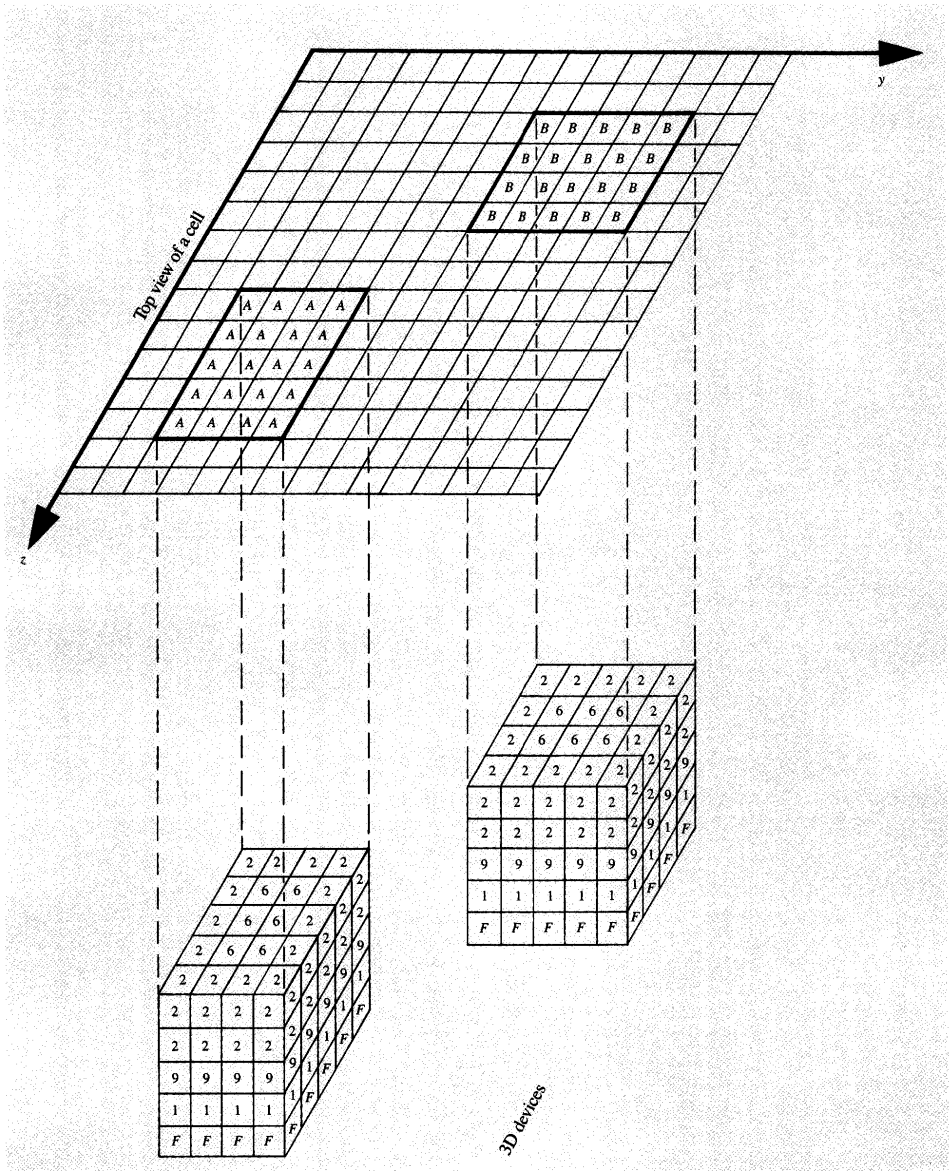

Figure 2.1: An example of SEMM geometry model, from[79]

through matter. The CCD models developed in this work are based on this toolkit. Benefiting from the object oriented programming of C++, GEANT4 applications are flexible, and easy to use. All the particles and physics processes involved in a simulation can be defined by the user, and the properties can be easily modified. A functional GEANT4 application needs to register three mandatory objects, which define the detector, the physics processes of interest, and the incident particles, to the kernel. They are implemented as virtual classes for the user to derive new classes. Optional user actions may be needed to perform extra functionalities, such as killing unwanted secondaries and recording reaction

version	release year	available classes
4.05.00	2003	1820
4.07.00	2005	2063
4.09.01	2008	2465

Table 2.1: Progress of GEANT4 development

products.

There are many software toolkits that are capable of simulating neutron effects on semiconductors, such as GEANT4 [75, 76], MCNP [81, 82], MCNP based packages (such as MCNPX [83–85], MARS [86]), and FLUKA [87]. Because of access restrictions, GEANT4 appeared to be the only choice for the purposes of access and distribution. Another main advantage of GEANT4, apart from its open-source nature [88], is that it is professionally maintained. Table 2.1 presents the enhancements of the released GEANT4 versions by the counts of available classes, which have names beginning with "G4". It can be observed that GEANT4 classes have expanded 20 % every two or three years, which demonstrates the potential of GEANT4. Several radiation effect tools are based on GEANT4 [89–91]. GEANT4 shows good performance in predicting neutron induced pulse-height spectra in PIN diodes [92], and has been used previously to simulate neutron effects in CCDs [93, 94]. It also can be used to analyse packaging effects of devices [95].

A brief assessment of GEANT4 follows.

MCNP, and packages based on it, has the largest group of users (about one third more than the users of GEANT4 in 2006) [84]. MCNP uses a measured data file up to 150 MeV [84], while GEANT4 uses neutron data only up to 20 MeV. As more measured data files are used, fewer errors may be introduced, and the predictions given by MCNP may seem to be more convincing.

Because it's a popular topic to compare the simulation results of these toolkits. The performance of GEANT4 are assessed from the openly published papers.

Lemrania et al. [96] have used GEANT4 and MCNPX to simulated the low

energy neutron (below 20 MeV) propagation in rocks. Unsurprisingly, the results closely agreed as they both use measured neutron data files in that energy range. Yeh et al. [97] have simulated neutron propagation in water using FLUKA, GEANT4 and MCNP in a higher energy regime (20 MeV to 150 MeV). Two points can be concluded from their results. First of all, GEANT4 and MCNP agreed closely at all the simulated energies (20 MeV to 150 MeV). Secondly, though FLUKA predictions have the largest discrepancies with the other two toolkits at most cases, these three toolkits agreed within 20% in all cases.

For light particle production at medium energy, the GEANT4 collaboration has presented comparisons of measured and simulated neutron production of medium energy protons on heavy metals on their website (see the "Medium Energy Verifications" [98]). The measured and GEANT4 calculated cross section curves overlapped almost at the full energy range, only small discrepancies are observed at the highest energies.

However, for single event effects, the neutron propagation and light particle production are not the key factors. The key factor should be the heavy ion production, because these have high LET and are capable of depositing large amounts of energy in a thin layer. A disappointing performance of GEANT4 on predicting the production of very heavy ions was reported by Reed et. al. [99] in 2007. They simulated the fragment production of 180 MeV protons on ^{27}Al, and compared the results with measurements as shown in Fig. 2.2. In this figure, the simulated results overestimated the production cross-section below about 8 MeV, but underestimated it above about 14 MeV. Reed et al. stated that similar results have been obtained for other residual nuclei. The impact of the wrong predictions of yielding energy could be significant for applications which have strong energy dependent responses.

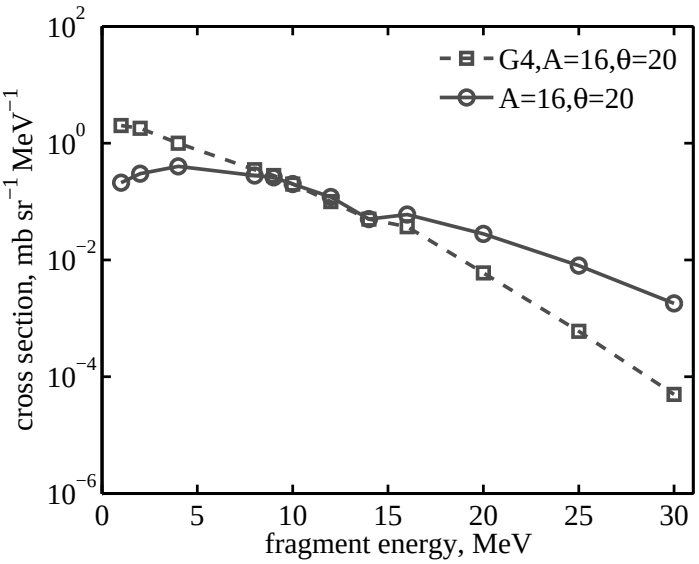

Figure 2.2: 180MeV protons fragment(A=16) production on ^{27}Al at $\theta = 20$, after Reed et al. [99]

Process	Energy	G4 class name	G4NeutronHP-dataset
neutron elastic	<20MeV	G4NeutronHPElastic	ElasticData
	>19.9MeV	G4HadronElastic	-
neutron inelastic	<20MeV	G4NeutronHPInelastic	InelasticData
	>19.9MeV	G4BinaryCascade	-
neutron fission	<20MeV	G4NeutronHPFission	FissionData
	>19.9MeV	G4LFission	-
neutron capture	<20MeV	G4NeutronHPCapture	CaptureData
	>19.9MeV	G4LCapture	-
proton elastic	<100TeV	G4HadronElastic	-
proton inelastic	<10GeV	G4BinaryCascade	-

Table 2.2: GEANT4 models to simulate ISEEM response to neutrons

2.3 Validation of developed GEANT4 code

The correctness of the developed GEANT4 code is discussed in this section.

The physics list used to simulate the hadron physics is shown in Table 2.2.

Truscott et al. [92] reported a comparison of the measured and simulated pules hight spectra of a silicon diode with a 300 μm thick, 25 mm diameter active region. In this work, a GEANT4 simulation was implemented to make compar-

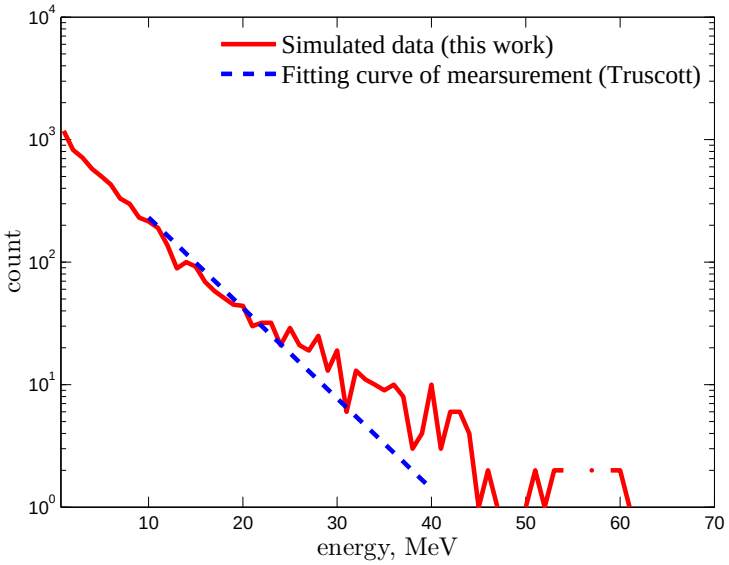

Figure 2.3: Simulated PIN diode pulse high spectra

ison with the work of Truscott et al. [92] to verify the correctness of the simulation code. Fig. 2.3 shows the calculated pulse height spectrum in a simulated 100 MeV monoenergetic neutron beam. The comparison with the 100 MeV quasi-monoenergetic simulated resulted in reference [92] is good. The exponential slope of the curve below 10 MeV decreases against energy. The slope is stable above 10 MeV, with a decay constant approximately 0.18 MeV^{-1}. The corresponding slope in reference Fig. 2.3 is about 0.15 MeV^{-1}. This discrepancy may be caused by the materials surrounding the active region, such as the device package. In this work, those materials are not simulated.

2.4 KAF-0402E geometry and the GEANT4 model

The KAF-0402E is the most used CCD in the measurements. It has been previously taken to the Los-Alamos Neutron Science Center (LANSCE) ICE House [65–67], the The Svedberg Laboratory (TSL) [68, 69], and the Tri-University Meson Facility (TRIUMF) [70] by Török and his co-workers. [64] This device has 0.4 mega pixels (512×768 pixels), and operated in full frame mode. The square pixel has the size of 9 µm. No anti-blooming gates are implemented in this CCD,

so all exceeding charges will flow into the vertically adjacent pixels. Fig. 2.4, from the device data sheet, illustrates the geometry of this device. There are five components, namely the image sensor, package, die attach resin, bonding wires, and cover glass. The image sensor was fully modelled in the simulation.

The corresponding CCD model in GEANT4 is shown in Fig. 2.5. The structure of the gates are suggested by Ciccaralli et al. [100]. Each pixel is $9\,\mu m \times 9\,\mu m$ and controlled by a pair of gates. One of the gates was made from silicon, and the other from indium tin oxide (ITO) [101]. The dielectric overlayer covered at the surface of the gate is assumed to be SiO_2. An additional aluminium enclosure face above the CCD surface was added in the simulated world volume. In all simulations, incident particles are in the plane at 90° to the aluminium face.

The depth of the active region was estimated from measurements of the alpha particle irradiations taken by Dunne [77]. In those measurements, alpha particles with energies in the range from 2.2 MeV to 4.4 MeV were incident approximately normally onto the CCD surface with the cover slip removed. The energy of the alpha particles were controlled by adjusting the distance between the source and CCD. To simplify the work of estimating the position of the CCD active region, all volume above the active region was assumed to be silicon. This assumption unifies the material of the device. However, there are two major components above the active region that are not silicon. If changing the materials can strongly distort the energy lost of the alpha particle in those regions, this assumption will introduce large error.

The first component is the passivation, the depth of which is approximately $3\,\mu m$ (estimated from [100]). Likely, it's made of SiO_2. The ranges of 1 MeV α particles in Si and SiO_2 are $3.51\,\mu m$ and $3.58\,\mu m$, respectively. Therefore, the stopping capabilities of $3\,\mu m$ Si and $3\,\mu m$ SiO_2 should be similar. Then the assumption should have a minor effect.

The second component is the ITO gate. Assuming the ITO to consist of 10%

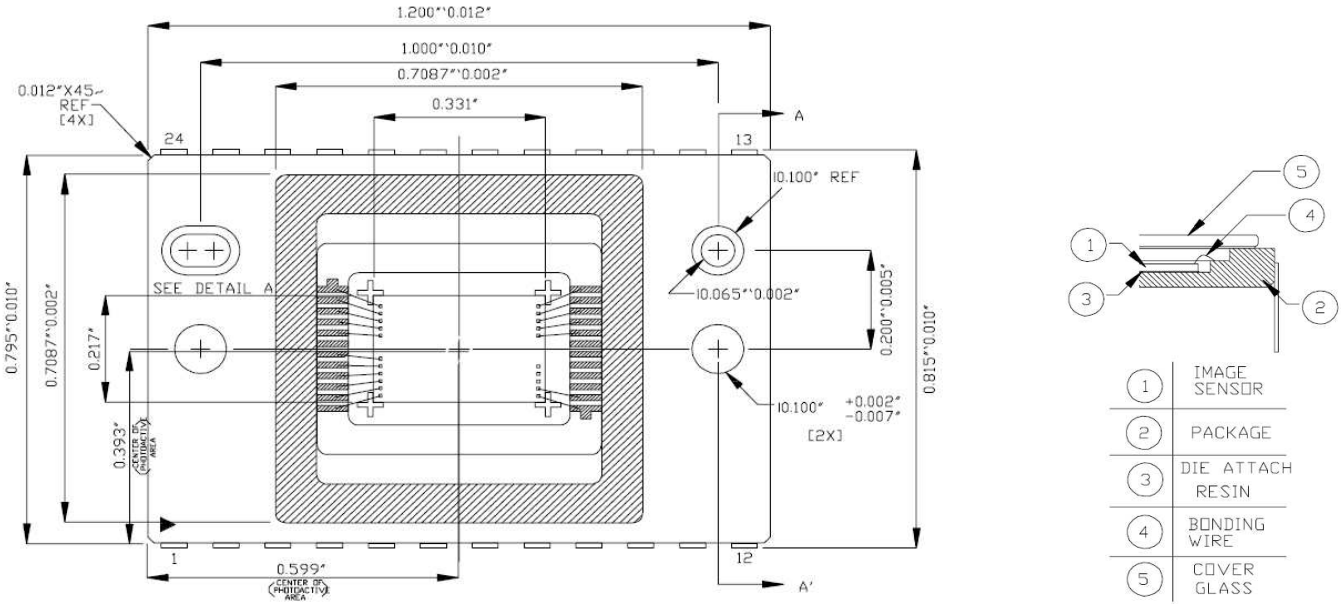

(a) Top view

(b) Side view

Figure 2.4: KAF-0402E geometry, from [101]

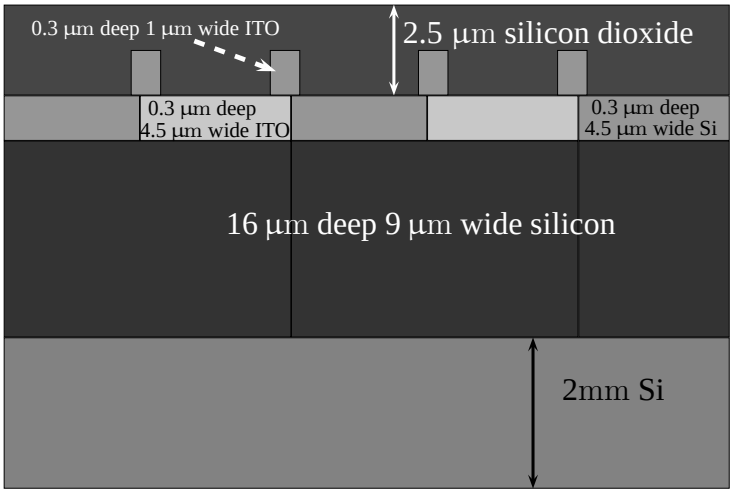

Figure 2.5: Simulated KAF-0402E geometry (not to scale)

SnO_2 and 90% In_2O_3, with density $7.12\,\mathrm{g}\cdot\mathrm{cm}^{-3}$, calculations using SRIM [102] predict that α particles do not deposit more than 80 keV in a track of 0.3 μm. Therefore taking the passivation and ITO gates to be silicon will make the alpha particle gain at most 50 keV energy, as 0.3 μm silicon can absorb at most 30 keV energy. Overall, the assumption has minor effect to the estimation.

The collected energy for each incident energy can be expressed as

$$E_i(r_b, r_e) = \int_{r_b}^{r_e} \frac{\mathrm{d}E_i}{\mathrm{d}x}\,\mathrm{d}x \tag{2.1}$$

where E_i is the collected energy, i denotes the identity of each incident energy, $\mathrm{d}E_i/\mathrm{d}x$ is the stopping power, and r_e and r_b are the limits of the active region. This equation is illustrated in Fig. 2.6, the data of which is calculated by SRIM [102]. This figure shows the stoping power of alpha particles at various energies. Energy noted at each curve shows the initial kinetic energy of the alpha particle. Here we have r_e and r_b both in the axis of the silicon depth. Equation 2.1 calculates the area under a specified curve in the region $[r_e, r_b]$.

The width, $w = (r_e - r_b)$, and depth of centre, $d = (r_e + r_b)/2$, of the active region are defined in Fig. 2.7. To estimate the value of w and d, they were enumerated in a range with a fine interval (0.02 μm per step); and corresponding E_i is calculated to compare with measurements. w and d were evaluated by the

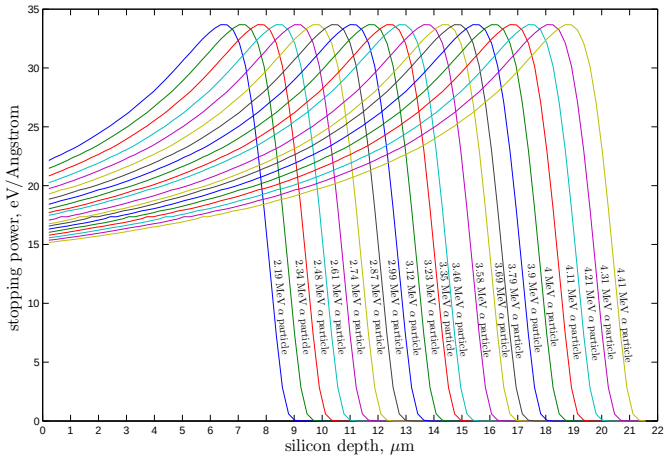

Figure 2.6: Stopping power of alpha particles in silicon

mean-square residual against the measurements:

$$MSR(w,d) = \sum_i (E_i(d - w/2, d + w/2) - kN_i)^2 \tag{2.2}$$

$$with\ w/2 \geq d \tag{2.3}$$

where N_i is the detected signal (total grey level) at each α energy and k is the conversion from measured grey level to energy, which is 3.5×10^{-3} MeV per digital number. It is clear that Equ. 2.2 is valid only when the depth is larger than half of width. The calculated MSR for various configuration is shown in Fig. 2.8. As defined by Equ. 2.3, data on the right hand side of the dashed line are valid.

The best estimate (the smallest MSR, which is 0.0757) is w =16.06 μm and d =11 μm. This implies an oxide layer thickness of approximately 2.5 μm, compared to a depth of approximately 3 μm estimated from [100]. Fig 2.9 compares measured and modelled deposited energies from the α-particle experiments. Fig. 2.9 shows the effect of energy loss in the overlayer and of saturation as energetic particles traverse the active layer, depositing some of their ionisation energy in the substrate (where the charge collection efficiency is assumed to be zero). Measured grey level and modelled energy deposition compare well.

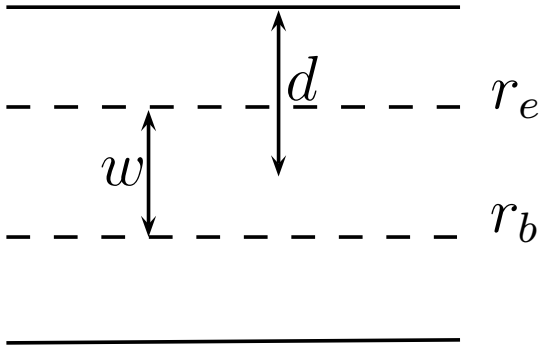

Figure 2.7: The width and depth of the active region

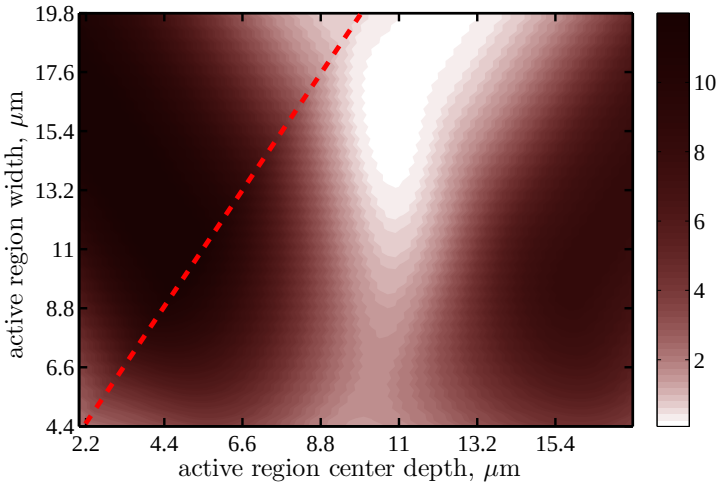

Figure 2.8: The contour plot of Equ. 2.2 for different active region depth and width

2.5 Simulation results

In the measurement, an event is defined as adjacent bright pixels (each brighter than 1.44 fC, which is the charge generated by 0.324 MeV ionizing radiation), when there is more than 8 fC charge in total. Those thresholds have been used in measurements at LANSCE, TRIUMF and TSL to effectively extract events [62, 71]. Some example events are shown in Fig. 2.10. To be consistent with the measurements, charged particles depositing more than 0.18 MeV , which can generate 8 fC of charge, in a close enough region are counted as an event in the simulations,. The CCD model was simulated with monoenergetic neutrons from 1 MeV to 9 GeV, and with five neutron beams.

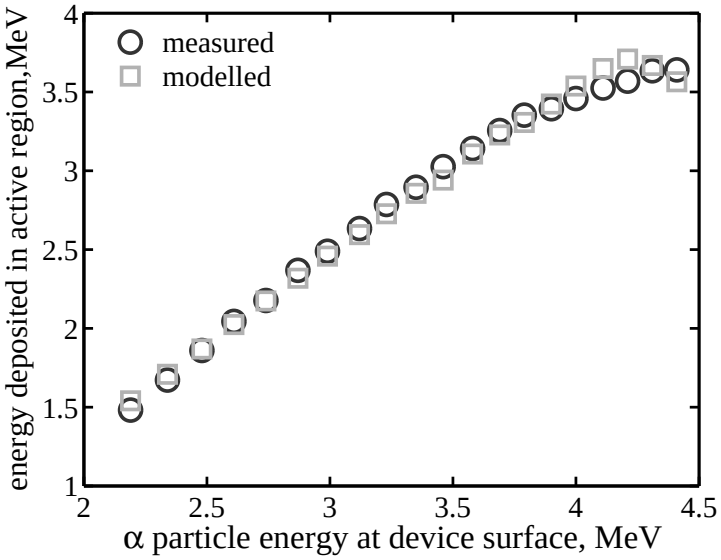

Figure 2.9: Alpha particle measurement and estimated energy

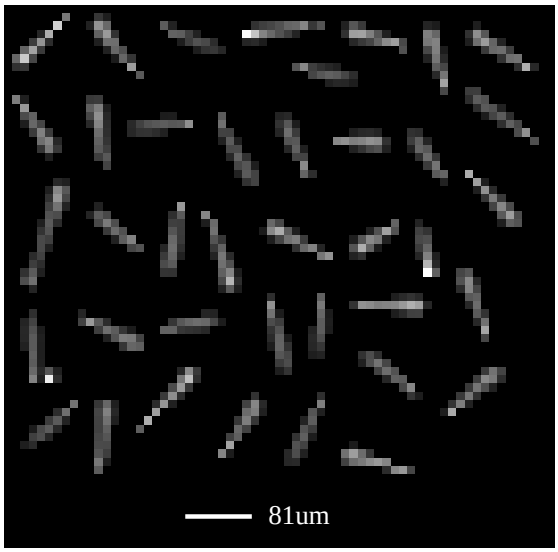

Figure 2.10: Example events

2.5.1 Simulation in monoenergetic neutron fields

The responses of the CCD to monoenergetic neutrons were simulated in the range from 1 MeV to 9 GeV. This section will analyze the simulated event cross-sections and the shapes of the charge collection spectra in different energies.

In each simulation, 5×10^7 incident neutrons were propagated normally through the model within a $4\,\mathrm{cm}^2$ cross-sectional area encompassing the whole active area of the CCD, corresponding to a neutron fluence of $1.25 \times 10^6\,\mathrm{cm}^{-2}$ at each energy.

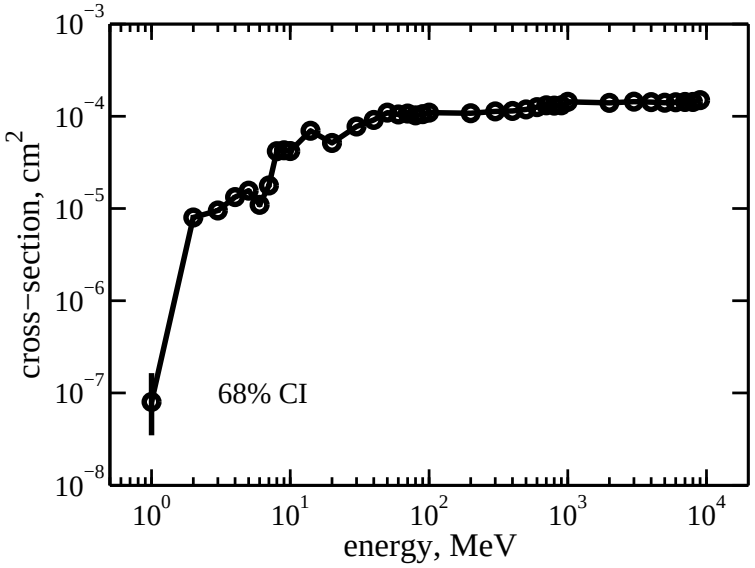

Figure 2.11: Simulated event cross-section in monoenergetic neutron fields

The monoenergetic event cross-section $\sigma(E)$ is calculated as:

$$\sigma(E) = \frac{N_e}{\Phi} \tag{2.4}$$

Here, N_e is the number of events depositing more than a threshold charge in the active region and Φ is the neutron fluence. Fig. 2.11 illustrates the simulated cross-sections. Error bars in this figure show 68% confidence interval (CI). They indicate that measured data points locate within them 68% of the time. The threshold charge (8 fC) is chosen to match the threshold adopted elsewhere in the analysis of experimental data [62, 71–73]. The cross-section increases by about two orders of magnitude between 1 MeV and 2 MeV. Two local peaks are observed at 5 MeV and 14 MeV, each followed by a dip. A similar peak in SEU cross-section at 14 MeV has been reported in several experimental and simulation studies of memory devices [63, 103, 104]. The cross-section increases steadily above 50 MeV from about $1.09 \times 10^{-4}\,\mathrm{cm}^2$ to about $1.49 \times 10^{-4}\,\mathrm{cm}^2$ at 9 GeV.

Table 2.3 shows the threshold energies of the reactions. Charge collection spectra for 2MeV to 5MeV neutrons are shown in Fig. 2.12. At 2 MeV only the elastic and inelastic collisions are active. Both of these reactions could deposit little energy. At 3 MeV, when alpha particles could be produced, the upper limit

Table 2.3: Example reaction threshold energies of ^{28}Si

reaction	energy(MeV)
n + ^{28}Si → ^{28}Si + n	0
n + ^{28}Si → ^{28}Si* + n	1.8434
n + ^{28}Si → ^{25}Mg + α	2.74554
n + ^{28}Si → ^{28}Al + p	3.99916
n + ^{28}Si → ^{24}Mg + α + n	10.346
n + ^{28}Si → ^{27}Al + d	10.5

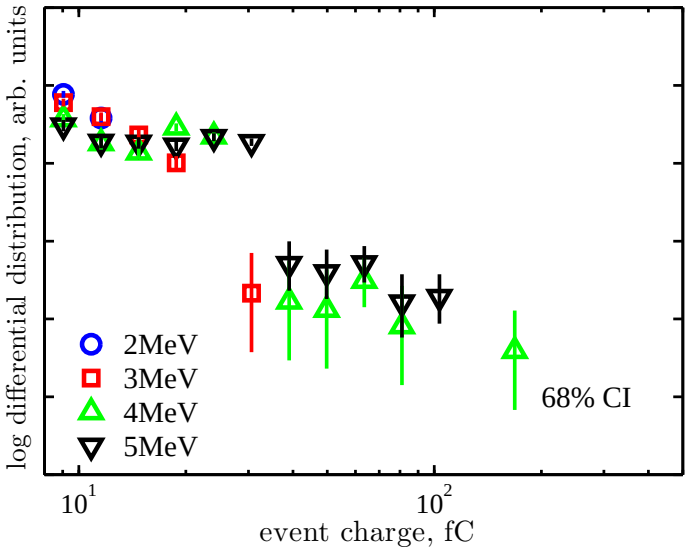

Figure 2.12: Simulated charge collection spectra on mono-energetic neutron field, 2 MeV to 5 MeV. Each interval in the vertical axis indicates a decade

of the spectrum is expanded from around 10 fC to 30 fC. Above 4 MeV, protons appeared, when the event upper limit is increased to 170 fC, the cross-section increased 7 times when energy move from 2 MeV to 5 MeV.

Fig. 2.13 shown the shape of charge collection spectra changes from 5 MeV to 14 MeV. At 10 MeV two peaks were observed at 12 fC and 110 fC.

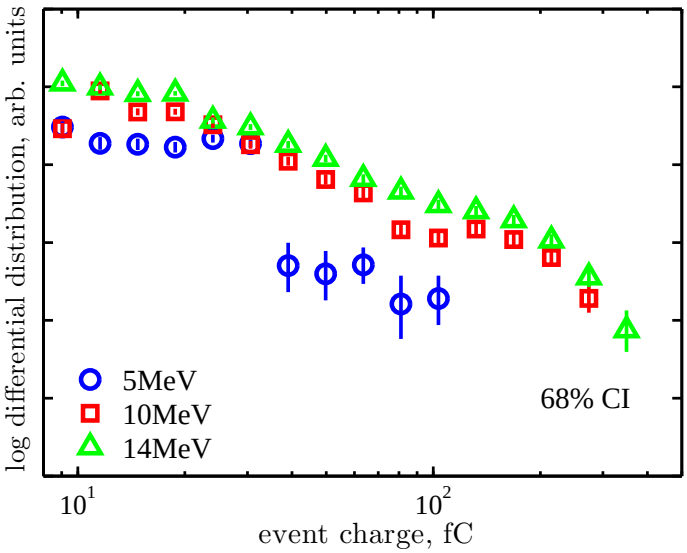

Figure 2.13: Simulated charge collection spectra on mono-energetic neutron field, 5 MeV to 14 MeV. Each interval in the vertical axis indicates a decade

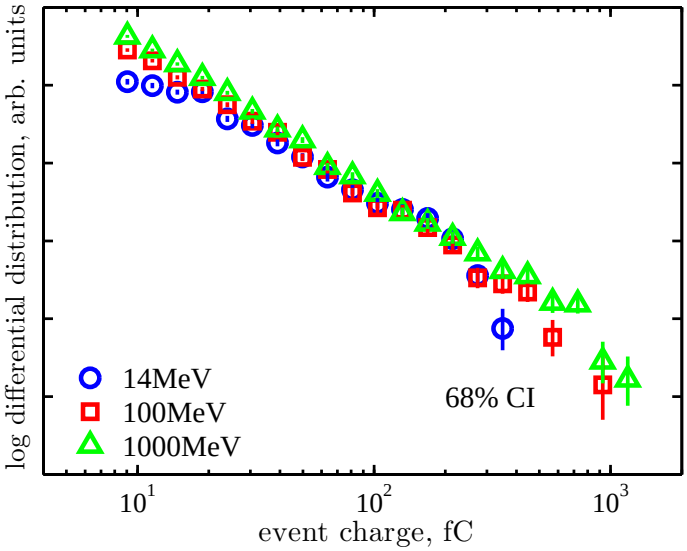

Figure 2.14: Simulated charge collection spectra on mono-energetic neutron field, 14 MeV to 1000 MeV. Each interval in the vertical axis indicates a decade

2.5.2 The secondary nuclide species

Fig. 2.15 shows the contributions of different particle types to the cross-section for events above 8 fC. As Fig. 2.15 shows, the component due to secondary hydrogen and helium ions is greater at 14 MeV than at 20 MeV. Baggio et. al [104] have recently reported that, for some SRAMs that are sensitive to helium ions, the

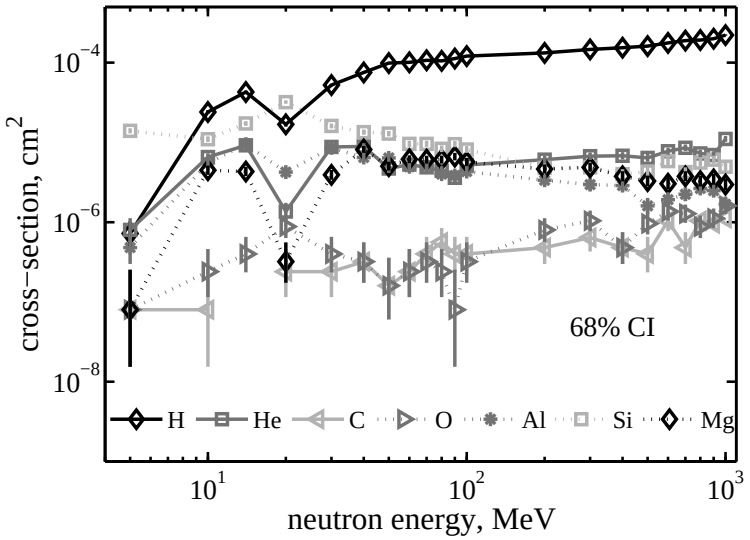

Figure 2.15: The contribution of different secondary particles to the event cross-section

SEE cross-sections can be greater at 14 MeV than at 100 MeV. However, the SRAMs studied in [104] are immune to hydrogen ions' direct ionisation due to the small feature size. Therefore the hydrogen ions' effect in those devices is not significant at all. However, it is no surprise also to see peaks in the aluminum and magnesium curves at 14 MeV, as these are the complements of hydrogen and helium, respectively. We also find a global maximum at 14 MeV for the contribution due to a local maximum in the cross-section for (n,xp) and (n,$x\alpha$) reactions in silicon around this energy [105].

As indicated by Fig. 2.11, the event cross-section above 50 MeV is nearly a constant. The major event contributors, which are hydrogen, helium, aluminium, magnesium, and silicon , show two different characteristics above 50 MeV. The production of lighter ions (hydrogen and helium ions) is increased against energy, and the production of heavier ions is decreased against energy.

Fig. 2.16 shows the proportion of event particles of each type which were produced in the active region. The blank squares indicate that no events were caused by the corresponding ion type.

A few particles with atomic number between helium and magnesium are ob-

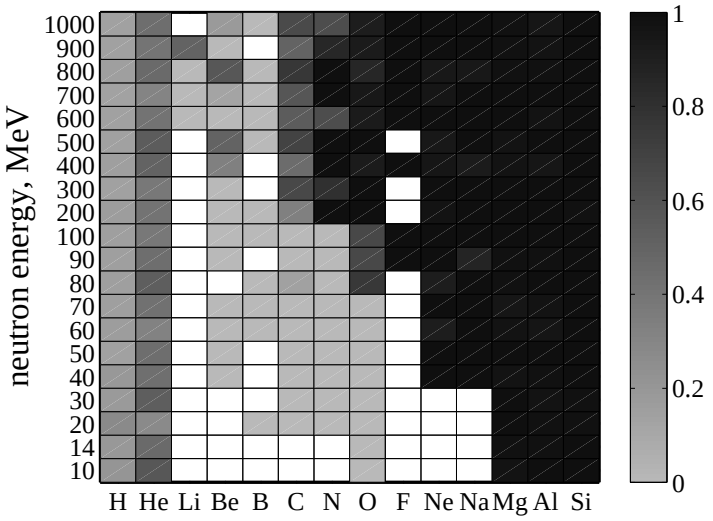

Figure 2.16: Proportions of event particles produced in the active region itself

served in the simulation. At the lower energies these come from reactions with oxygen in the passivation; with increasing energy these ions can be produced by silicon-neutron reactions and at the highest energies most come from the active region itself. Take carbon for example. Fig. 2.17 shows the cross-sections of possible reactions that can introduce carbon into the active region below 250 MeV. The data for this plot were calculated using TALYS [106]. The threshold for Si(n,xC) reactions is about 50 MeV. Below this threshold, as the active regions are taken to be pure silicon, the apparent carbon ions must be produced in the surroundings by O(n,xC) reactions whose threshold is about 2 MeV. Fig. 2.15 shows a minimum in the cross-section for carbon-induced events around 50 MeV. This is because both types of carbon production mechanisms are weak at this energy.

Fig. 2.16 also shows very high proportions for locally generated heavy ions. At all energies more than 97% of magnesium, aluminium and silicon ions originate in reactions in the active region.

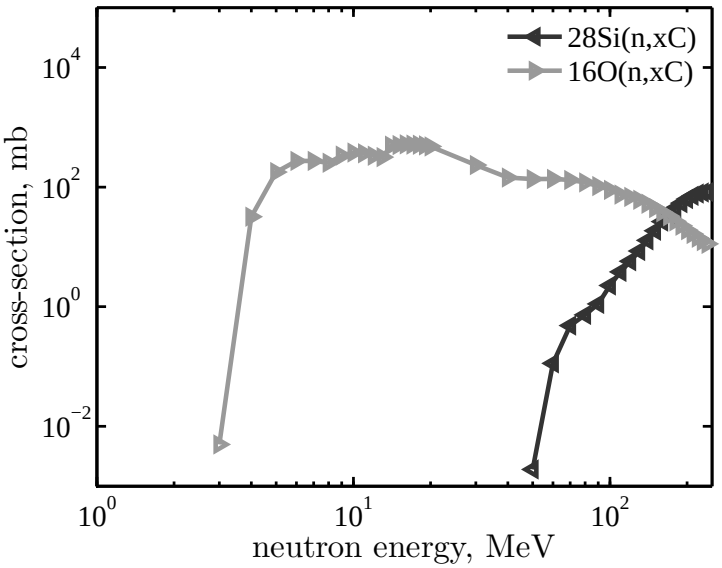

Figure 2.17: Cross-sections for possible reactions introducing carbon into the active region below 250 MeV

2.5.3 Origins of the secondary nuclides

Origins of secondary Hydrogen, Helium, Aluminium, Magnesium and Silicon are compared in Fig. 2.18 to Fig. 2.22 at 14, 50, 100, 300 and 1000 MeV. It can be seen that as the secondaries get heavier, more heavy ions are from the active region itself.

As indicated by Fig. 2.15, Hydrogen and Helium have the dominant number in the secondaries. As suggested by Fig. 2.18 and 2.19, the coverslip, active region along with the substrate are the main regions of producing those ions. The substrate is shown to be good at producing Hydrogen. About half of the hydrogen is from the substrate. After the active region, the coverslip is second major producer of helium. The helium production is very interesting. The global peak of helium at 14 MeV neutron shows not only at the bulk silicon, but also at the SiO_2 and even at the air. It may suggest oxygen or nitrogen or both have a peak helium production cross-section at 14 MeV. For the heavier ions, their productions are decreased against energy above 50 MeV. This can also be observed in Fig. 2.15.

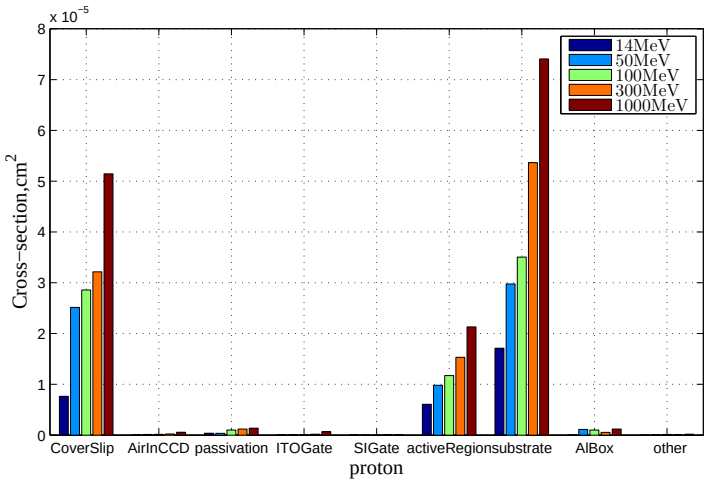

Figure 2.18: Hydrogen Origins

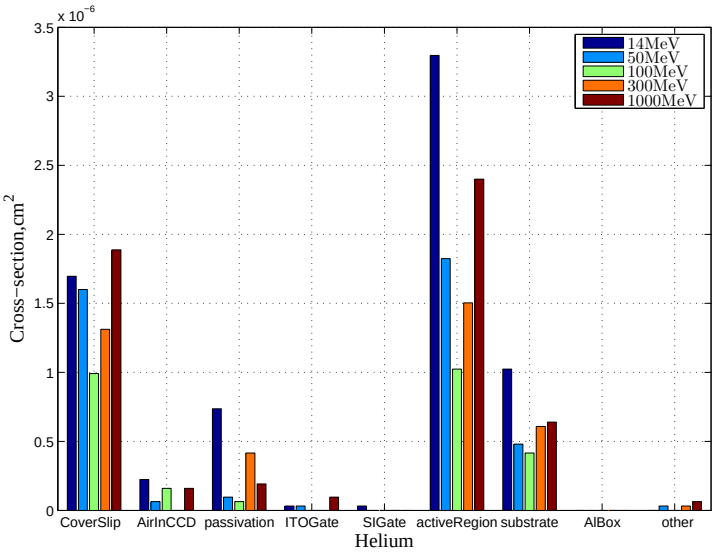

Figure 2.19: Helium Origins

2.5.4 Simulation in complex neutron fields

The corresponding neutron spectra of the complex fields are shown in Fig. 2.23. ISEEM behaviour was simulated in each of these neutron fields and results compared to measurements. Analysis of the measured data included frame cleaning, whereby one raw frame is subtracted from the previous one to remove all the permanent bright pixels in the frames, as often result from neutron-induced displacement damage. Transients due to Random Telegraph Signal (RTS) noise[107]

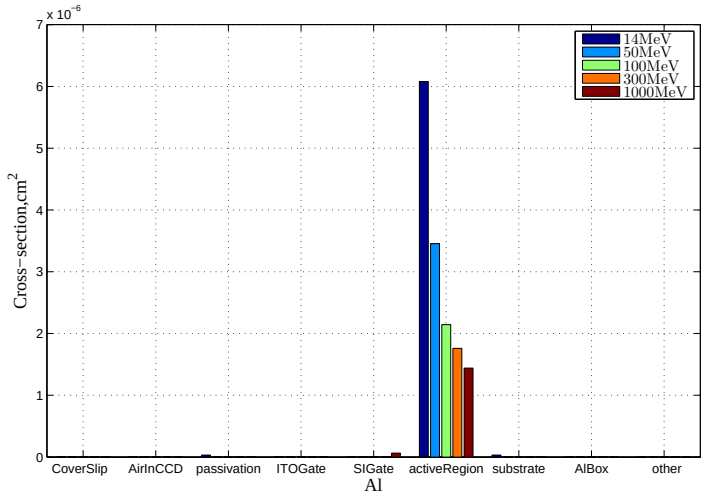

Figure 2.20: Aluminium Origins

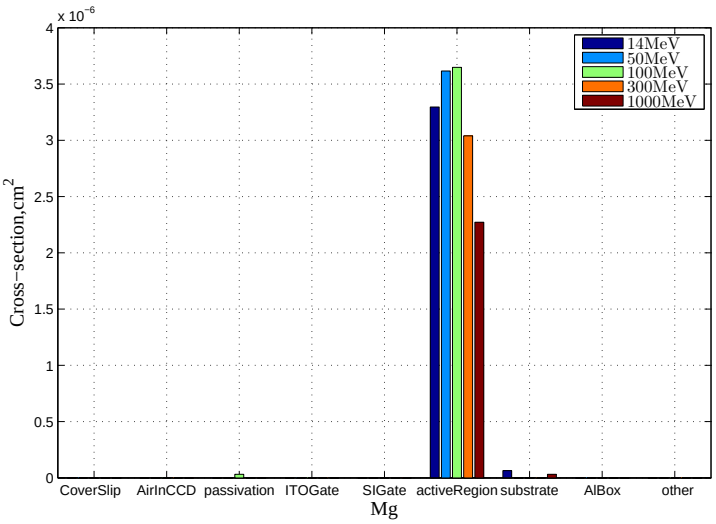

Figure 2.21: Magnesium Origins

were also identified and excluded from the measured data set. RTS is the signals from some damaged pixels. The events generated by such signal are relatively easy to be identified. They consist of a single pixel, and the charge level varies over time. Therefore, such hard damage effects were not considered in the simulations as they do not influence the measured data. In all the simulations, particles were incident normally on the aluminium box.

Simulated and measured event charge distributions agree closely. Examples are shown in Fig. 2.24. Similar agreement is found in the other fields studied.

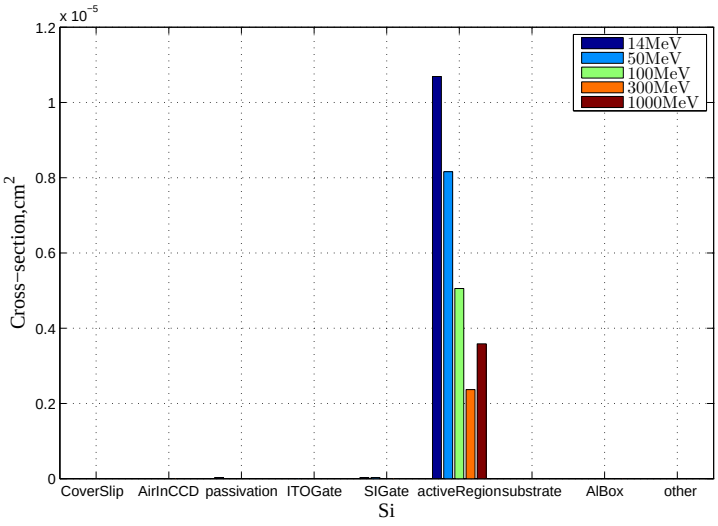

Figure 2.22: Silicon Origin

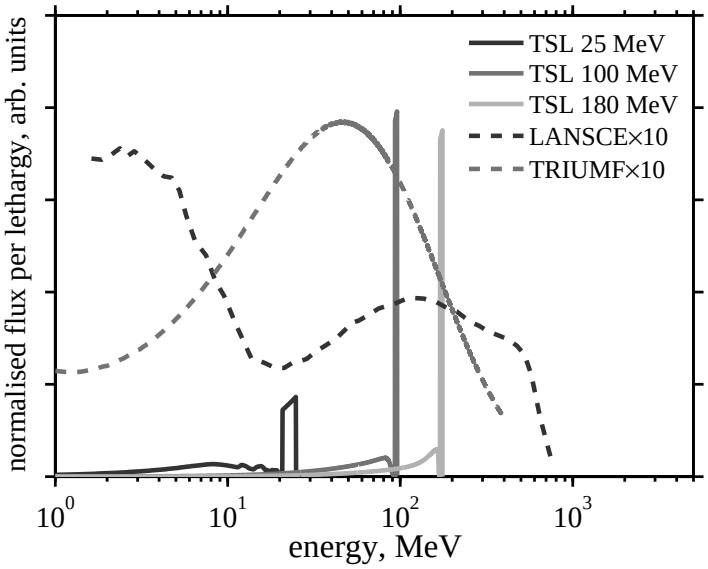

Figure 2.23: Spectra of accelerated neutron fields

The experimental event cross sections were previously measured by other researchers. [62, 71]. Those cross sections are defined as,

$$\sigma = \frac{N_e}{\Phi_h} \tag{2.5}$$

Where Φ_h is the integral neutron fluence. In the case of the white beams at LANSCE and TRIUMF, Φ_h is the fluence of neutrons above 10 MeV. In the case of the quasi-monoenergetic neutron beam at TSL, Φ_h is the fluence of neutrons at the quasi-monoenergetic peak. Simulated cross-sections are presented in Table 2.4,

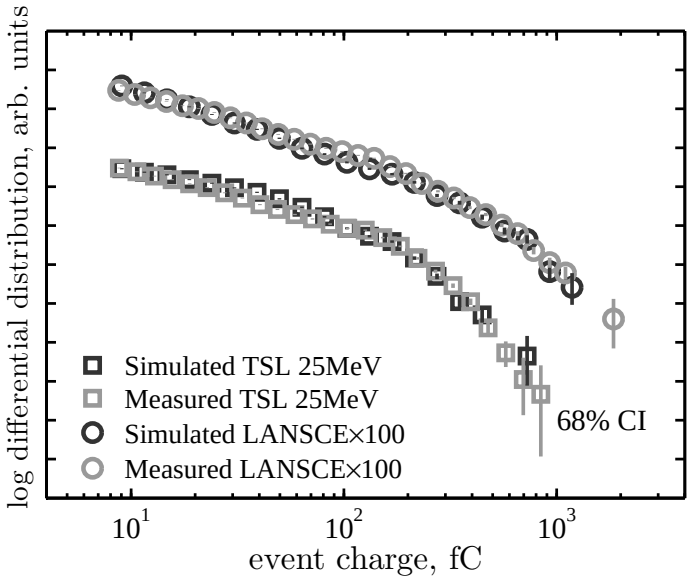

Figure 2.24: Event charge distribution comparisons for TSL 25 MeV and LANSCE

Table 2.4: Measured and simulated integral cross-sections in ISEEM

	cross-section, 10^{-5} cm^2	
	measured	simulated
LANSCE	7.66	11.2
TRIUMF	8.09	9.22
TSL 25 MeV	6.56	11.1
TSL 100 MeV	12.9	26.1
TSL 180 MeV	11.3	24.5

along with previously reported experimental data [71].

The simulated cross-sections in the white beams at LANSCE and TRIUMF are about 46% and 14% over the measured values, respectively. The simulated cross-sections in the quasi-monoenergetic beams at TSL exceed the measured values by between 69% and 117%, the discrepancy increasing as the quasi-monoenergetic peak moves to higher energies. The discrepancies are discussed in more detail in section 2.6.

Fig. 2.25 shows the contribution of particles of different types to the event cross-sections in the simulated LANSCE and TRIUMF beams. It shows that the extra component of the simulated cross-section at LANSCE is due to additional

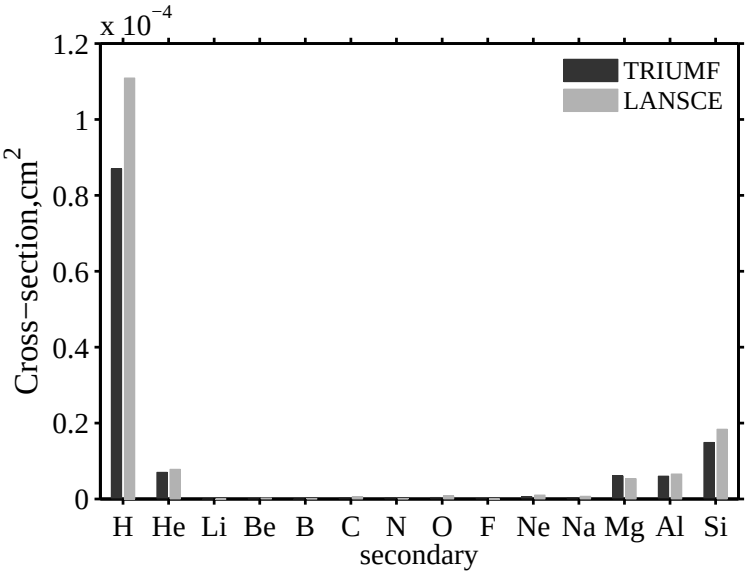

Figure 2.25: Types of particles generated at LANSCE and TRIUMF

recoils from elastic scattering and, especially, secondary hydrogen ions. The majority of events at this low threshold (i.e. 8 fC) are caused by hydrogen ions arising from interactions in regions other than the device active layer, most notably the substrate. Almost 40% of the simulated events originate in the silicon substrate, and the cross-section for these interactions is significantly greater in the harder beam at LANSCE. For the TSL simulations, the behavior of the discrepancy increased as the quasi-monoenergetic peak moves to higher energies. We discuss this in more detail in section 2.6. Fig. 2.26 shows the contribution of particles of different types to the event cross sections in the simulated TSL 25 MeV, 100 MeV and 180 MeV quasi-monoenergetic beams. The most striking feature is that many more hydrogen ions are generated as the energy of the quasi-monoenergetic peak increases from 25 MeV to 100 MeV.

2.6 Discussion of possible error sources

This section discusses the possible sources that can contribute to the discrepancies between the measured and simulated event cross-section.

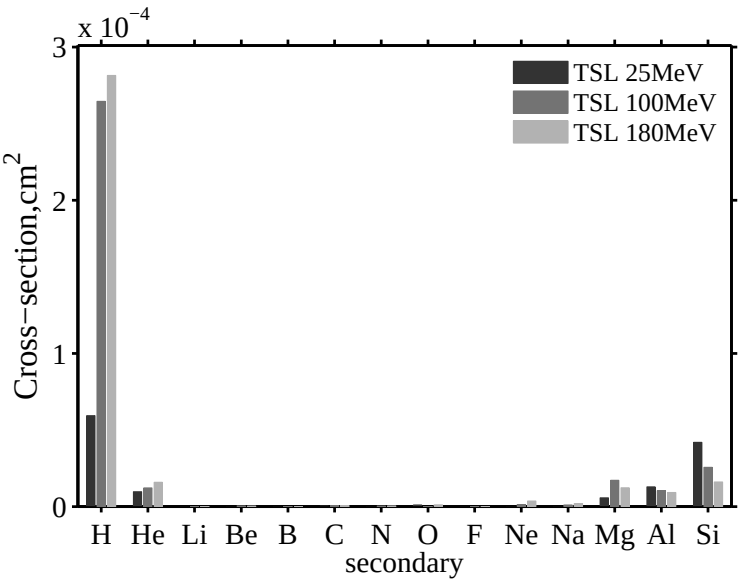

Figure 2.26: Types of particles generated at TSL

2.6.1 The absolute neutron fluence in measurement

The uncertainties in the measured cross-sections derive mostly from uncertainties in the absolute values of the neutron fluence.

For LANSCE the uncertainty in measured fluence is understood to be about 5% below 20 MeV [108]. The portions below and above 20 MeV each contribute about half of the total fluence above the ISEEM threshold of 2 MeV. The contribution to the cross-section of the higher-energy portion should be much the greater, as indicated by Fig. 2.11. Therefore the uncertainty of the fluence above 20 MeV should be a more important factor; but it's unknown. The uncertainty in the measured cross-section at LANSCE is therefore liable to be greater than 5%.

At TRIUMF, the absolute accuracy of the measurement of fluence above 10 MeV is understood to be about 30% [109]. As the event cross-section above 10 MeV is much larger than that below 10 MeV, and as about 80% of the neutrons to which ISEEM is sensitive (i.e. above about 2 MeV) are above 10 MeV, most events at TRIUMF should be caused by neutrons above 10 MeV and the uncertainty in measured cross-section should be dominated by that quoted for the measured integral fluence. Although the simulated cross-section for TRIUMF ex-

ceeds the measurement it is within the likely measurement uncertainty of about 30%.

For TSL, the measurement of fluence in the quasi-monoenergetic peak is understood to be accurate to 10%. This peak constitutes around 40% of the total fluence. The uncertainty in the contribution of the low-energy tail is less clear. However the discrepancies between measured and simulated cross-sections at the higher energies seem unlikely to be explicable by measurement uncertainty alone.

2.6.2 The CCD model in simulation

The simulations appear systematically to overestimate event cross-sections at all simulated fields. Possible sources of error include our model of the CCD geometry, as both the depth of the active region and the detailed construction of the underlying regions are estimated in the absence of design data. One of the largest sources of error is likely to be the assumption of 100% charge-collection efficiency in the active region.

Significant proportions of events are caused by particles entering the active region from outside, especially from the substrate. These will deposit significant proportions of their energy in low-field parts of the active region leading to charge collection processes which are heavily dependent on diffusion effects and subject to recombination processes. As a result, charge-collection efficiencies significantly less than 100% are likely to be experienced (cf. [110, 111]) leading to overestimated cross-sections in the simulations.

2.7 Summary

This Chapter introduces the preliminary Monte Carlo simulations of neutron interactions in the CCD using GEANT4. The GEANT4 hadron models were verified by simulating the pulse high spectrum of a pin diode, of which the design parameters and measurement results were known from the literature.

A simple CCD model was constructed using the results of alpha particle experiments. The simulated charge collection spectra shows good agreements with measurement in quasi-monoenergetic and white neutron beams. However, simulated event cross-section overestimated measurements up to a factor of two. It's suspected that this error is mainly introduced by lack of charge diffusion model. The later work described in Chapter 3 confirms such error is the dominant error in the simulation.

Chapter 3

The responses of CCDs to ionizing radiation

This chapter introduces the work of adding a charge diffusion model to the GEANT4 model. Chapter 2 presented the simulated results of the GEANT4 model. It successfully predicted the charge collection spectra in artificial neutron beams, and helped to understand the species and origins of the secondaries. However, the calculated event cross-sections overestimated those cross-sections from measurements by up to a factor of 2.4. Oversimplified charge collection behaviour of a CCD in the model may be one of the major error sources. A charge diffusion model was added to simulate charge diffusion in the low-field region of a CCD's sensitive region. The overall accuracy of the simulation was improved.

When Török began to develop ISEEM, he tested three different CCDs in accelerated beams to find the most suitable one for radiation monitoring. These CCDs are: KAF-0402E (9 μm pixel size, no anti-blooming protection), KAF- 0401LE (9 μm pixel size, lateral-overflow drain (LOD) for anti-blooming protection) and KAF-1401E (6.8 μmpixel size, no anti-blooming correction). Then KAF-0402E was identified to be the best CCD for use, because it has higher event cross-section and lower price. Most later measurements in this research group used this CCD as suggested by Török. However, one of the most critical design parameters, the

depth of the active region, of this CCD is still unknown. However, the sensitive depth of KAF-1400 is understood to be 15 μm. [112] KAF-1401E is an optically enhanced version of KAF-1400. Such enhancement was made by using a new material (indium tin oxide) to make one of the control gates. The design parameters of the these two CCDs may therefore be similar. Therefore the depth of the sensitive region in KAF-1401E was taken to be 15 μm. The KAF-1401E was used as the benchmark device in this work to evaluate the performance of the improved simulation model, and this new model of KAF-1401E has been found have an maximum error of 30% at LANSCE and TRIUMF. As this discrepancy is less than the absolute neutron fluence errors quoted by the facilities, this new model is considered to have good performance.

The parameters of the KAF-0402E were adjusted to calibrate to the LANSCE neutron spectrum. Because this spectrum is probably the best for the beams available. The simulated results of this calibrated model shows that the maximum error of the improved simulations on KAF-0402E is between -20.0% to 14.2% at all tested fields, including LANSCE, TRUMF, TSL QMN, and TSL ANITA.

3.1 Short review of charge diffusion models

Kirkpatrick did the pioneering work [113] to model the diffusion charge generated by ionizing particles in semiconductors in 1979. After that work, many diffusion models were published to model charge diffusion in semiconductor (e.g. [114–119]). Kirkpatrick's model was used in a CCD's low-field region by Lomheim et al. [112] in 1990. Lomheim et al. introduced a model to simulate charge collection behaviours of a CCD. In this model, the active region of a CCD was divided into two layers. The layer close to control gate is the "high-field region", and the other layer is the "low-field region". Charges in the high-field region are 100% collected, and charges diffuse according to Kirkpatrick's model in the low-field region. The simulated spatial charge distributions of this model are very similar

to the measurements, except the model tends to spread charges in a larger area.

In 1998, Pavlov et al. introduced a method [115] to model the charge collection in CCDs. In their model not only charge diffusion in the field free region, but also charge sharing in the high-field region could be characterized. Because more details are considered in this model, the implementation might be relatively difficult.

More recently in 2008, Rolland et al. introduced a method to model the charge collection in the field free region [119]. Along with this method, they also publish a companion paper [120] of applying this method in a Matlab simulation. As the arithmetic of implementation in [120] is very efficient and relatively simple, their model was chosen for use in this work.

3.2 The geometry of the KAF-1401E

The KAF-1401E is a 1.4 millon-pixel full frame CCD. Its pixel size is $6.8\,\mu m \times 6.8\,\mu m$. Lomheim et al. has noted that for the device KAF-1400, the depth of the active region is about $15\,\mu m$ [112]. As the KAF-1401E is the optically enhanced version of the KAF-1400, the design parameters of the these two CCDs may be similar. Therefore the depth of the active region in KAF-1401E was taken to be $15\,\mu m$.

The detailed geometry of KAF-1401E sensitive region is similar to the geometry described in Chapter 2, except for the different pixel size and the depth of the active region. Also the gates above the active region were replaced by the extension of the passivation, because of their complex structure and extremely weak contributions (see section 2.5.2).

The geometry of the CCD KAF-1401E is shown in Fig. 3.1. As indicated by this figure, the package of this CCD can be divided into five layers. Each layer can be represented by a box with a hole in the center as illustrated in Fig. 3.2. The materials of the package are unknown. In this simulation, it was taken to be aluminum oxide.

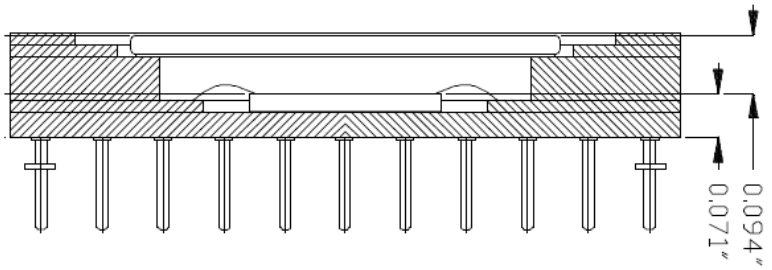

Figure 3.1: Geometry of KAF-1401, from [121]

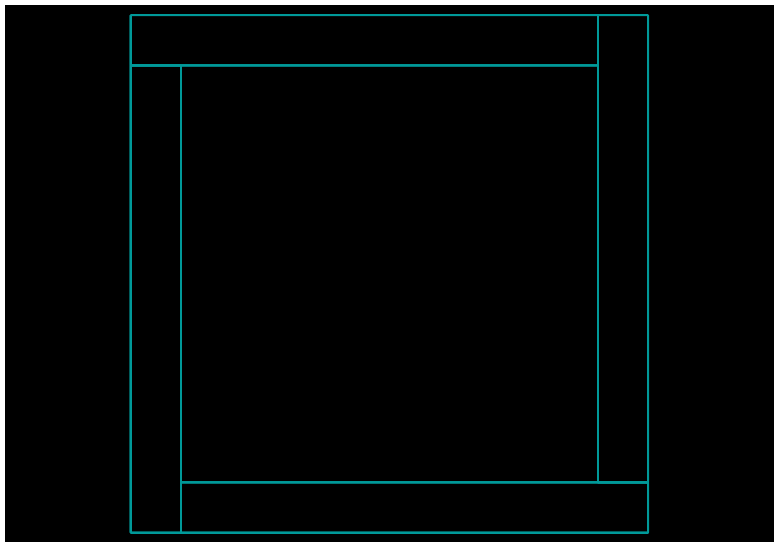

Figure 3.2: Box with a hole volume for modelling the CCD package

The corresponding world geometry in simulation is illustrated in Fig. 3.3a. To simplify the work, the bonding wires and the device pins were not modelled. The overall errors generated by omitting those components should be minor, as they were either far away from the sensitive region or have very small volume.

There is a gap of 1.4 mm air between the 1 mm coverslip (assumed to be SiO_2) and the 3 μm passivation (assumed to be SiO_2). The 15 μm active silicon in red is underneath the passivation. There is a 0.8 mm inactive silicon region underneath the active silicon. It has the same area as the active silicon in the x-y plane. Also one face of an aluminum enclosure above the coverslip also included in the simulation.

Neutrons were incident normally on the model from random positions within a plane above the aluminum enclosure. This plane covered an area of 4 cm^2. The

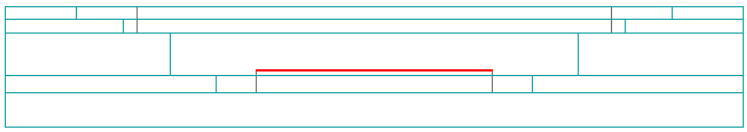

(a) Side view

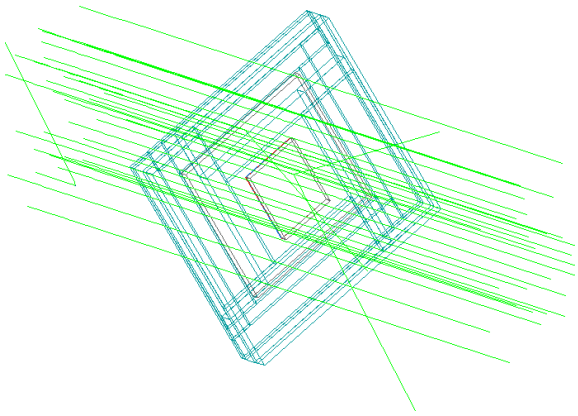

(b) neutron irradiation

Figure 3.3: KAF1401E geometry in GEANT4 simulation

simulated CCD irradiation in a neutron beam is illustrated in Fig. 3.3b. The propagation steps in the sensitive region was limited to 0.1 µm. Coordinates of the charged particles in that region, along with corresponding energy deposition of individual step were recorded.

3.3 Modelling charge diffusion in the diffusion region

The characteristics of the diffusion were studied based on Rolland's model [119]. In the case where S_c is a disc of radius R_D on the contact surface of the depletion and diffusion regions, and the point source is right beneath the centre of the disc. The total charge collection Q_c, which is equivalent to charge collection efficiency (CCE), can be calculated as,

$$Q_c(Z_0, R_D) = Q_c(Z_0, \infty) - \sum_{m=-\infty}^{m=+\infty} \frac{a_m \exp(-\eta R_m)}{R_m} \tag{3.1}$$

with

$$Q_c(Z_0, \infty) = \frac{\exp(-\eta a_0) - \exp(-\eta(2 - a_0))}{1 - \exp(-2\eta)}$$

$$and\ a_m = \frac{Z_0}{H} + 2m\,;\ R_m = \sqrt{\frac{R_D^2}{H^2} + a_m^2}\,;\ \eta = \frac{H}{L_d}$$

where Z_0 is the depth of the source, H is the thickness of the low-field region, L_d is the diffusion length. These equations are only valid for the "point source" radiation, such as X-rays. For charged particles, the trajectories of the particles are needed to be split into small segments to approximate the requirement. In the STARDUST code [120], the segments were user defined to be 0.1 µm. [122]

Fig. 3.4 shows the CCE of the 5 µm, 10 µm and 50 µm discs. The CCEs of circular planes were calculated assuming the depth of the diffusion region is 20 µm and the diffusion length is 80 µm. It's observed that the CCEs of smaller plane decrease much quicker.

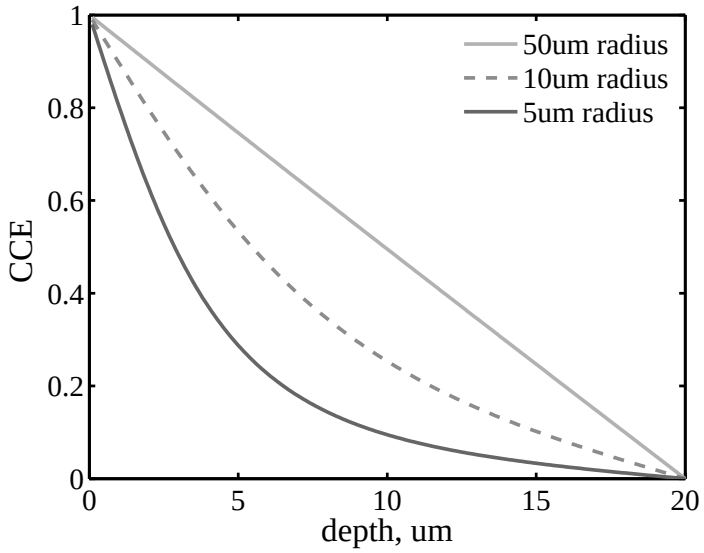

Figure 3.4: Charge collection efficiency as a function of the depth and the sensitive area

One of the hypothesis of this diffusion model is that the bottom plane of the diffusion region is a true ohmic contact. The closer the charges are to the bottom

plane, the larger chance they diffuse into the substrate, instead of being collected by a pixel. Therefore, it's not surprising to observe the CCE drop from 1 at the top plane to 0 at the bottom. In the case of a CCD, the bottom plane of the CCD diffusion region is a P to P^+ doped transition. A known effect of such a transition is to introduce a potential barrier which can partially reflect the carriers towards the potential well [122]. The impact of this effect is not clear. However, the good agreement of simulated and measured charge collection distributions suggested this effect has minor impact.

For the KAF-1401E, it is assumed that the 3 µm high-field region has 100% CCE, and the CCE of the 12 µm diffusion region varied against the depth of the source. Rolland's method [119] was used to calculate the pixel collection from the diffusion region. In the case where a point source located at the depth of Z_0, and the position of interest at the top of the diffusion region is $\vec{\rho}$, the charge density, Q, at that position is,

$$Q(Z_0, \vec{\rho}) = \frac{1}{2\pi H^2} \sum_{m=-\infty}^{m=+\infty} \frac{a_m(1+\eta R_m)\exp(-\eta R_m)}{R_m^3} \tag{3.2}$$

with

$$\rho = |\,\vec{\rho}\,|$$
$$and\ a_m = \frac{Z_0}{H} + 2m\,;\ R_m = \sqrt{\frac{\rho^2}{H^2} + a_m^2}\,;\ \eta = \frac{H}{L_d}$$

where Z_0 is the depth of the source in diffusion region, H is the thickness of low-field region, L_d is the diffusion length. The diffusion length is the average distance of electrons travel before the total number is reduced to $1/e$ of the original number [123]. This parameter is unknown at the moment. However, Janesick noted (page 615 of [123]) that "the extent of the field-free region in a CCD is considerably less than the diffusion length". Taking the diffusion length to be 200 µm may be a reasonable estimation.

Fig. 3.5 shows the density of the collected charges in this CCD model (calculated by of Equ. 3.2). The agreement with the density in the Rolland's original paper [119] is good.

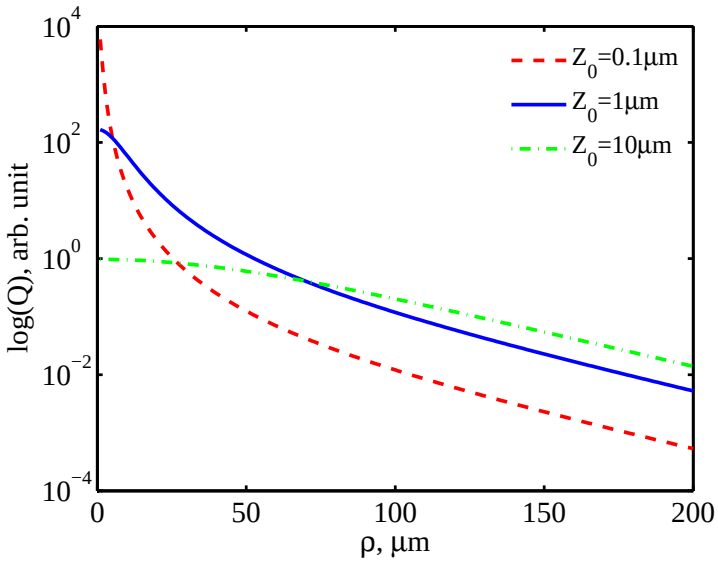

Figure 3.5: Density of collected charges

The calculations of charge densities are time consuming. Instead of calculating them at run time, the pre-calculated data can be used in the manner of a look-up table. This technique was introduced in the reference paper of STARDUST [120]; and it is introduced below.

Fig. 3.6 illustrates a pixel defined by four points, $P1(X_1, Y_1)$, $P2(X_2, Y_1)$, $P3(X_2, Y_2)$ and $P4(X_1, Y_2)$. The charge collection efficiency of the source at Z_0, CCE_p, can be efficiently calculated as

$$CCE_p = Q_{int}(P3) + Q_{int}(P1) - Q_{int}(P2) - Q_{int}(P4) \tag{3.3}$$

where Q_{int} is the integrated charge density, and defined by Equ. 3.4.

$$Q_{int}(P(x_1, y_1)) = \int_{-\infty}^{x_1} \int_{-\infty}^{y_1} Q(Z_0, \vec{\rho})\, dy\, dx \tag{3.4}$$

Therefore, a large 3 dimensional matrix of $Q_{int}[x, y, z]$ was prepared for the next stage of the work. The indexes x and y are the ordinates of a corner of a pixel. Index z is the depth of the source.

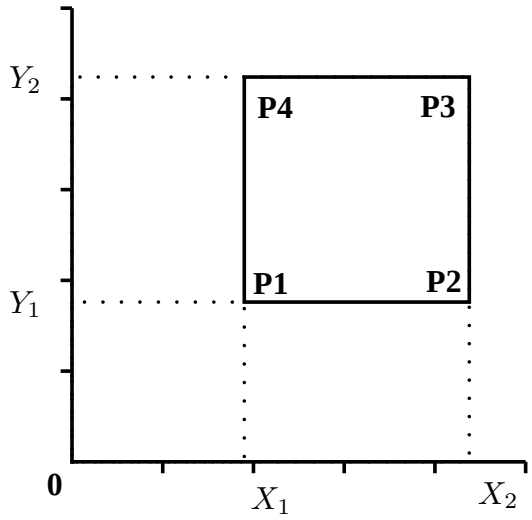

Figure 3.6: Calculating the charge collection efficiency of a pixel

3.4 The implementation of the charge diffusion model in KAF1401E

The matrix of Q_{int} was calculated by Matlab and stored in a mat file. This file is read by a binary executable to generate images according to the particle segments recorded in a GEANT4 simulation.

A 5 MeV proton with 90 degrees incident angle against the KAF-0402E was simulated. It assumes that the depth of the depletion region is 3 μm, the thickness of the diffusion region is 20 μm, and one digital number in the final readout image represents 51 electrons. Fig. 3.7 shows the simulated readout image. It can be seen the charge is evenly distributed around the proton entry point, and extended over 4 pixels. The most and second most outer rounds of the pixels show about 1% of the pixel DN [1] in the centre. About 0.35 MeV was deposited in the sensitive region, and only 0.14 MeV of that was collected by the pixels.

One example frame generated in a 900 MeV monoenergetic neutron simulation is illustrated in Fig. 3.8. There are $2.5 \times 10^6 \mathrm{cm}^{-2}$ neutrons passing normally through the simulated CCD geometry. Charges generated by the ionizing secondaries were accumulated in the CCD, and finally saved as this frame. All types

[1] DN, digital number of a pixel in a gray-level image

0	0	1	3	4	4	2	1	0	0
0	0	2	9	20	19	8	2	0	0
0	1	3	21	165	118	17	3	1	0
0	1	3	20	288	96	16	3	1	0
0	0	2	8	17	16	7	2	0	0
0	0	1	2	3	3	2	1	0	0
0	0	0	1	1	1	0	0	0	0

Figure 3.7: Simulated 5MeV proton 90 degree incident event

of reactions can be observed in Fig. 3.8. The most notable one is that due to the secondary protons. Most of the protons penetrate the active region. A small fraction of them have long tracks in the active region. For example, there are three proton tracks in the bottom left corner of Fig. 3.8.

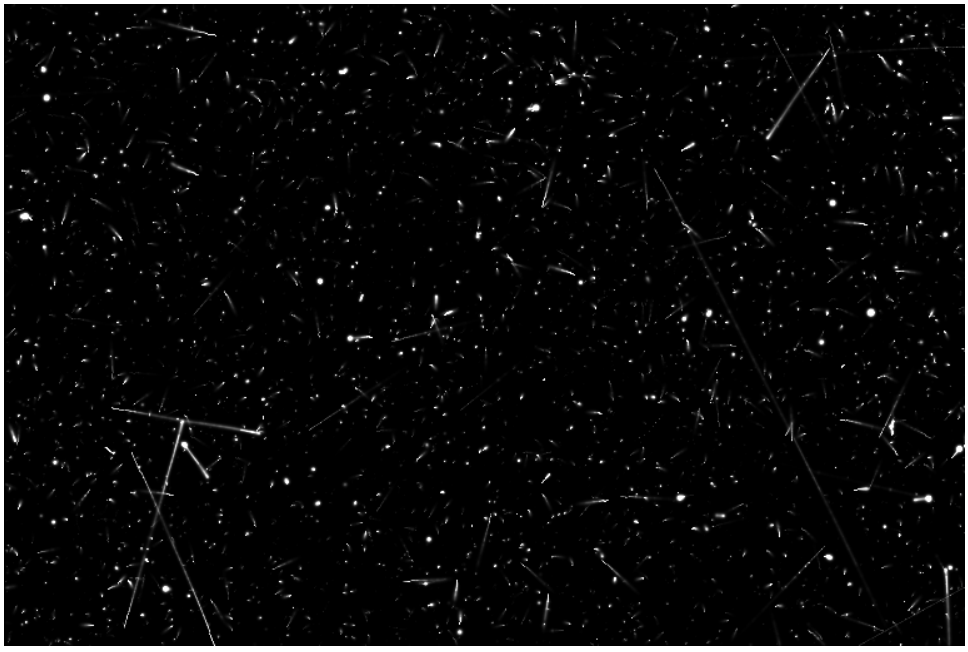

Figure 3.8: Simulated deposition of $2.5 \times 10^6 \mathrm{cm}^{-2}$ of 900 MeV neutrons in the CCD

3.4.1 Event analysis

In the measurements, an event in KAF-1401E was defined as a group of adjacent pixels that individually collected more than 1.44 fC charge, where there is more than 8 fC charge collected in total. The events in simulation were counted according to this definition.

The simulated and measured event cross-sections at LANSCE and TRIUMF are shown in Table 3.1. It's known that the error of absolute neutron fluence at TRIUMF is $\pm 30\%$. The agreement of simulation and measurement at TRIUMF is within 3%. The LANSCE simulation overestimated the measurement by 27.6%. The error of absolute neutron count at LANSCE was unknown. More discussions about the errors can be found in [124]. The overall prediction accuracy is good.

spectrum	simulated event cross-section $(1 \times 10^{-5}\text{cm}^2)$	measured cross-section $(1 \times 10^{-5}\text{cm}^2)$
LANSCE	13.4	10.5
TRIUMF	11.5	11.7

Table 3.1: Comparisons of simulated and measured KAF1401E event cross-sections

The event charge spectra are compared in Fig. 3.9. For both TRIUMF and LANSCE, the charge collection spectra agreed closely. However, there are more large events observed in measurement than in simulation at LANSCE.

The event area distributions are shown in Fig. 3.10. It can be seen that the simulated event area distributions decay much quicker than those from measurement; and this is not caused by the statistical errors. Very likely, it is caused by blooming effects of the device in the measurements. Approximately 20% of simulated event pixels exceed the blooming threshold (7.2 fC) at both LANSCE and TRIUMF. In practice, those event pixels would extend the event vertically. This miscounted effect can lead to the observation. This simulation methods are later implemented to the KAF-0402E. Results show that for KAF-0402E the simulated pixel distributions agreed closely with those from measurements for KAF-0402E.

Because fewer (11% out of the total event pixels) event pixels exceed the blooming threshold of that device.

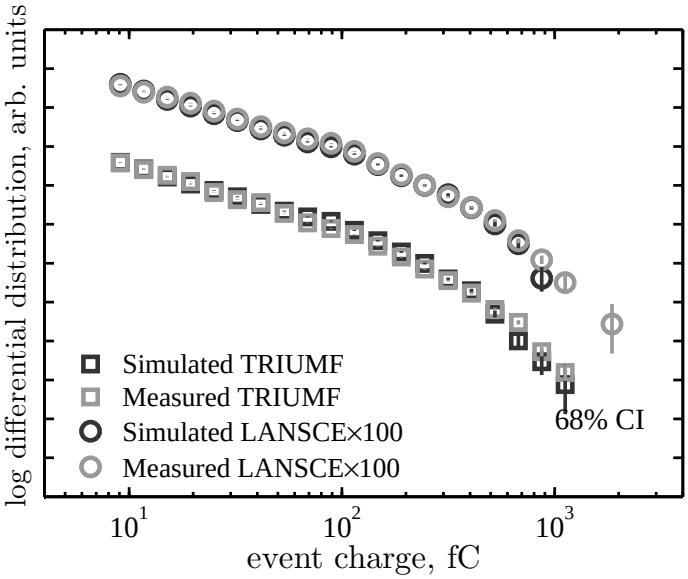

Figure 3.9: Comparisons of event charge spectra

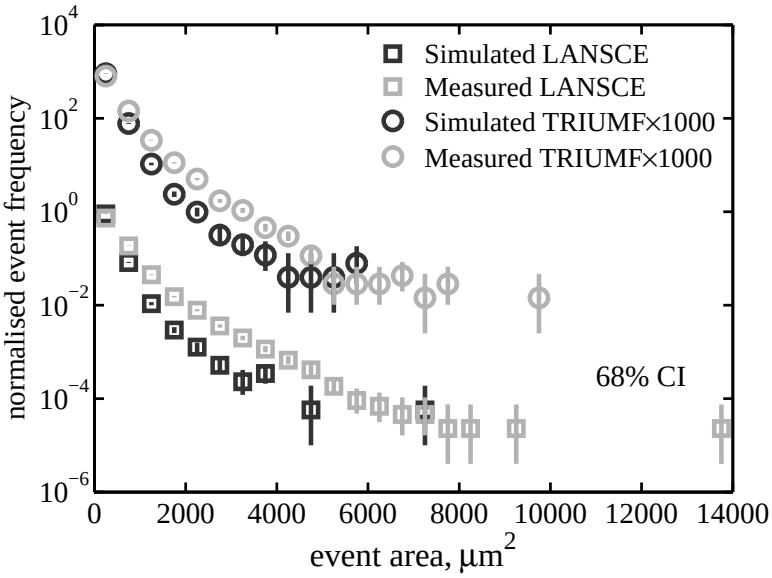

Figure 3.10: Comparisons of event size spectra

3.5 KAF-0402E parameter calibration

The simulation on KAF-1401E demonstrated the performance of the improved model.

The parameters of the KAF-0402E were calibrated using LANSCE spectrum. Table 3.2 tabulated three sets of parameters that were tested in the KAF-0402E model. The measured event cross-section of this device on LANSCE was $7.66 \times 10^{-5}\text{cm}^2$. The simulated cross-sections are very sensitive to the depth of the high-field region and are relatively insensitive to the diffusion length. It can be seen that the parameter sets with 3 µm depletion region depth and 20 µm diffusion region depth agree with the measurment with an error of 6% to 7%. Therefore, they were chosen to be used in the model.

depletion region (µm)	diffusion region (µm)	diffusion length (µm)	cross-section ($1 \times 10^{-5}\text{cm}^2$)
3	20	30	7.39
3	20	80	7.45
4	20	80	8.83

Table 3.2: Sets of parameters tested on KAF-0402E model

Indicated by Table 3.2, the diffusion length has a minor effect on the event cross-section. It also has minor effect to the event charge and spatial distributions. Fig. 3.11 and 3.12 illustrate an example of those distributions in LANSCE when the diffusion lengths are 30 µm and 80 µm.

3.6 Performance of the calibrated model

In previous section, the parameters of KAF-0402E were identified. The depth of depletion region is 3 µm. The depth of diffusion region is 20 µm. The diffusion length is 80 µm.

This calibrated model was used to calculate the event cross-sections in complex fields. The results are tabulated in Table 3.3. Simulation for TRIUMF underestimates the measurements by 25%, somewhat better than the quoted error in the measurement (i.e. ±30%). TSL simulations still systematically overestimate the measurements. The discrepancies increased from 16% to 42% when the quasi-monoenergetic peaks moved from 25 MeV to 180 MeV.

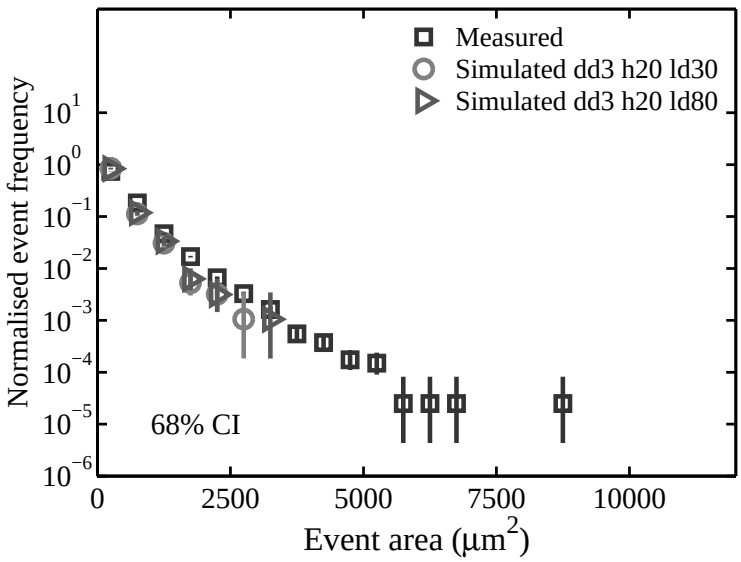

Figure 3.11: Comparisons of simulated and measured LANSCE event area distribution

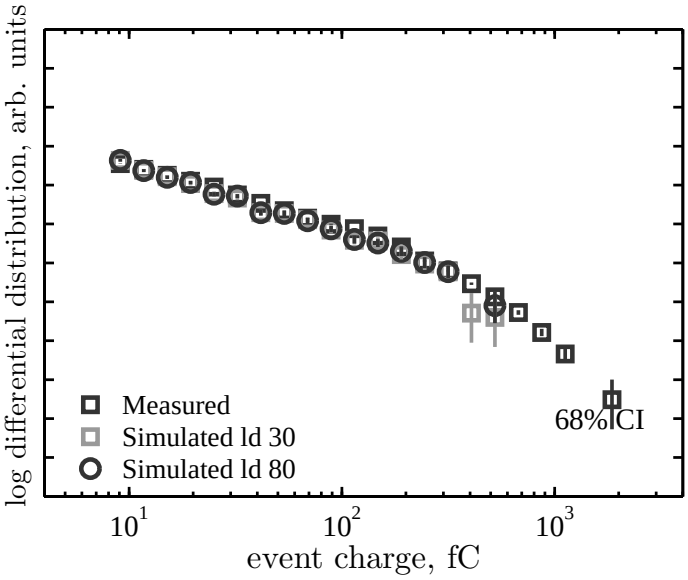

Figure 3.12: Comparisons of simulated and measured LANSCE event charge distribution

3.7 The response function of KAF-0402E to neutron

The response of calibrated KAF-0402E to neutrons is tabulated in Table 3.4. The cross sections are calculated for events above 8 fC. These data can be used to fold

facility	measured cross-section $(1 \times 10^{-5}\text{cm}^2)$	simulated cross-section $(1 \times 10^{-5}\text{cm}^2)$
LANSCE WNR	7.66	7.45
TRIUMF NIF	8.09	6.48
TSL QMN 25MeV	6.56	7.62
TSL QMN 108MeV	12.9	17.1
TSL QMN 180MeV	11.3	16.1

Table 3.3: Simulated results of using the calibrated KAF-0402E model

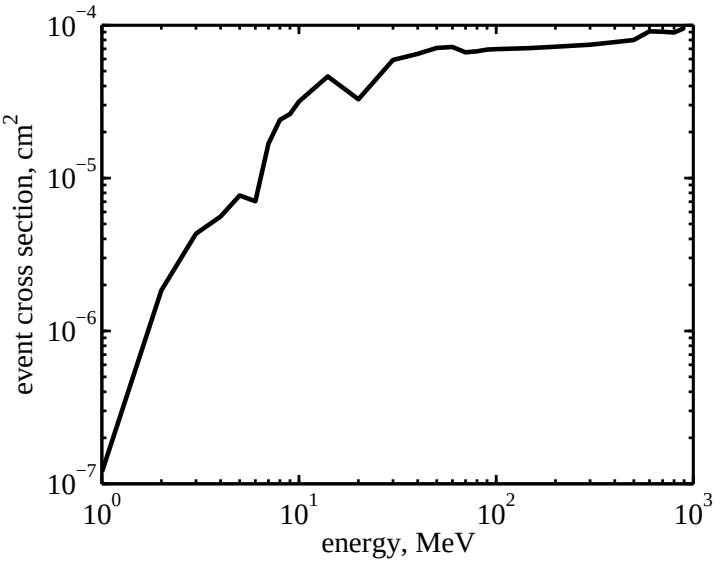

Figure 3.13: The response function of ISEEM

a neutron spectrum to estimate the event cross-section. They are also plotted in Fig. 3.13. The expected peak at 14 MeV was observed. However, the characteristic dip of some SRAM memory at 150 MeV [6] was not observed. Possible, simulations failed to predict this dip, or, more likely, it is only a characteristic of certain devices.

3.8 Summary

This chapter introduced the method of developing the improve ISEEM simulation model. This method was first applied to KAF-1401E to examine its correctness. Good results were obtained. Then KAF-0402E was simulated using this new model.

energy (MeV)	beam area (cm^2)	neutron count (10^7)	event (8fC Thr)	cross section ($10^{-5}cm^2$)
1	1	2.5	3	0.012
2	1	2.5	46	0.184
3	1	2.5	108	0.432
4	1	2.5	140	0.560
5	1	2.5	192	0.768
6	1	2.5	176	0.704
7	1	2.5	420	1.68
8	1	2.5	599	2.40
9	1	2.5	656	2.62
10	1	2.5	789	3.16
14	4	10	1154	4.62
20	4	10	817	3.27
30	4	10	1479	5.92
40	4	10	1620	6.48
50	4	10	1776	7.10
60	4	10	1880	7.20
70	4	10	1659	6.64
80	4	10	1684	6.74
90	4	10	1729	6.92
100	4	10	1740	6.96
150	4	10	1769	7.08
200	4	10	1805	7.22
300	4	10	1863	7.45
400	4	9.6	1861	7.75
500	4	10	2000	8.00
600	4	10	2280	9.12
700	4	10	2259	9.04
800	4	10	2234	8.94
900	4	10	2385	9.54

Table 3.4: Monoenergetic neutron simulation results

With the charge diffusion model, the results of the first simulation on KAF-1401E are promising. The simulated event cross-sections agreed with measurement better than 30%. The results validated the combination of GEANT4 simulation and charge diffusion model. However, some important factors were still unclear. For example, the doping profile of the CCD is unknown. The diffusion length of this CCD was taken to be 80 μm for KAF-0402E. Though diffusion length can slightly affect calculated cross-sections, the effect is minor. Changing

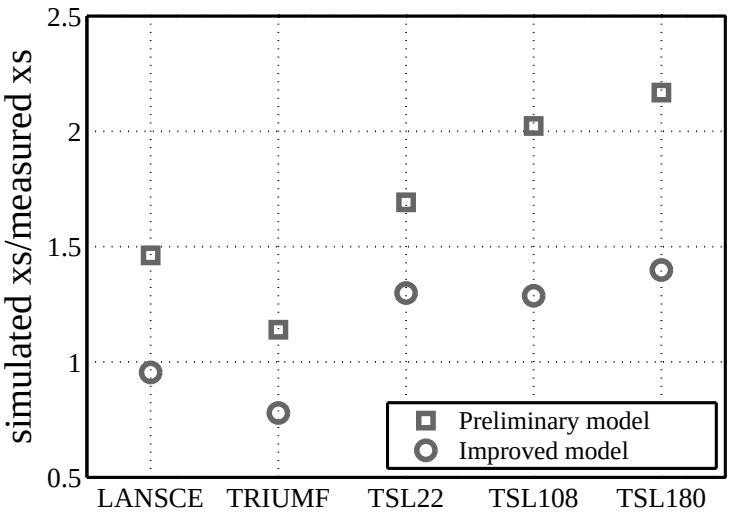

Figure 3.14: Performance comparison of the simulation models

the diffusion length of the KAF-1401E from 20 μm to 200 μm would increase the cross-sections in white beams by about 1%.

The simulated event cross-sections of KAF-0402E have better agreement with the measurements than the results from the preliminary work. (see Fig. 3.14) That is the key contribution of the diffusion model. The measured event spatial spectra of KAF1401E were strongly affected by CCD's blooming effect, but this effect is weaker in KFA-0402E, because the spatial distributions from simulation and measurement agreed.

Chapter 4

ISEEM performance in the natural cosmic radiation environment

The previous two chapters introduced the simulation results of ISEEM in accelerated testings, and the results were experimentally validated. This chapter discusses ISEEM performance in the natural cosmic ray life testing.

This chapter first discusses the different experimental conditions in SSER and ASER testings, and then analyzes the corresponding effects.

Two ASER measurements using ISEEM are also reported in this chapter. The measurement taken at Jungfraujoch was simulated in GEANT4. It has been found that neutrons, protons and alpha particles are the dominant sources of the events.

Overall results suggest that ISEEM is a good instrument to measure accelerated beams, but it has a poor performance in the natural environment testings.

4.1 Different experimental conditions of SSER and ASER testings

The event cross-section, σ, in the unit of cm^2, derived from a ASER testing can be used to calculate the SSER of a device in the unit of FIT as

$$SSER = \sigma\varphi \times 10^9 \tag{4.1}$$

φ, in the unit of $cm^{-2}.d^{-1}$, is flux density of a location in the atmosphere. The term 10^9 is the the billion hours in the FIT rate definition.

However, secondary cosmic rays are different to neutron beams in several aspects. First of all, secondary cosmic rays represent a compound field. It has extremely low flux density, and bombards devices with random angles. Therefore some neglectable effects in the ASER testings become significant in the SSER testings, such as the alpha contamination, device angular effect, and proton effect.

4.1.1 The major error sources

In a SSER testing, the event sources are the energetic protons and neutrons, alpha particle contaminations, and thermal neutrons.

Thermal neutrons can be the dominant event source if boron-10 is present near the device's sensitive region, as discussed in section 1.1. However, thermal neutrons can be shielded off by wrapping the devices with gadolinium or cadmium foils. Those foils have high cross-section to interact with thermal neutrons. Therefore, they can efficiently attenuate thermal neutrons. For example, a 1mm thick gadolinium foil have an attenuation factor of 4.3×10^{-53} ·[6].

For a modern SRAM, alpha particle contaminations and fast neutrons are the major event sources. Results of two 0.13 µm SRAM SSER testings in the literature are selected as in Table 4.1. It shows that events caused by alpha particles can be as many as those caused by neutrons. The alpha particle soft error rate in devices is mainly dependent on the materials and technology [4, 30, 34]. It

SRAM	location	neutron SER (FIT/Mb)	alpha SER
A[125]	Jungfraujoch	717	960
B[34]	ASTEP	710	380

Table 4.1: Selected SSER results

is independent of the neutron flux density. The most accurate way to quantify the alpha soft error rate is to place samples deep underground or underwater, where neutron flux density is negligible. The neutron soft error rate is proportional to the flux density of neutrons.

4.1.2 The angular effects

Flament ea al. [126] demonstrated that ome devices can have an order of magnitude different cross-sections at different neutron incident angles in a 14 MeV neutron beam. This effect is due to the nature of the angular-dependent secondaries distribution. For example, Fig. 4.1 shows the ^{28}Si (n,xα) energy-angle distributions at 100MeV. Data in this figure are calculated by TALYS version 1.0. [106] The 0° out going angle is the same direction as the incident neutron, while the 180° out going angle is the revers direction. It can be observed that the 0° out going angle has a higher cross-section, especially for the high energy alpha particles.

In the work of Schwank et al. [127], some SRAMs that contain high-Z materials were tested in proton beams from 50 MeV to 200 MeV. Strong angular dependance of SEE cross-section also observed. It is suggested by the authors that the secondary angular distribution of the high-Z materials should answer for this. The Rosetta experiment [36] of Xilinx undertook an ASER testing for FPGAs. The FPGAs also were measured in accelerated beam. The highest cross-section was obtained when the neutron beam was incident on the device from the substrate through the top face. It is suggested that there were higher

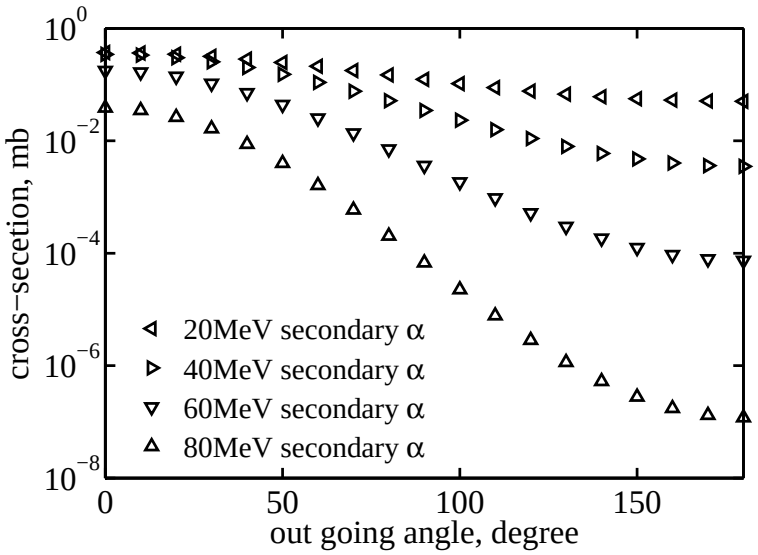

Figure 4.1: ^{28}Si (n,xα) energy-angle distributions at 100MeV incident energy

cross-section materials underneath FPGA. The materials are identified to be the flip chip solder balls used to connect the die and the substrate.

The complexity of this effect leads to an uncertainty in the event rates predicted by ASER.

4.1.3 The effective particles in cosmic rays

As suggested by Ziegler et al. [7], protons and neutrons are the dominant sources of SEE in the secondary cosmic ray. Pions can also have strong interactions with matter; but have a very low flux density. Muons, electrons, and gammas are too weakly ionising to induce SEE.

Protons are negligible in some accelerated neutron beams. For example, TSL QMN has one proton in a million neutrons [128], and simulation also has shown that the proton/neutron ratio at TSL ANITA is less than 0.15%. [129].

Energetic protons are one of the major secondaries in the atmosphere. Ratios of energetic (above 10 MeV) protons and neutrons were evaluated at three locations using QARM. The locations are Jungfraujoch (3570m above sea level), ASTEP (2550m above sea level) and Preston (sea level). The integral flux density of neutrons and protons were calculated by QRAM. The results are tabulated in

location	integral flux density above 10MeV ($10^{-3}\,\mathrm{cm}^{-2}\cdot\mathrm{s}^{-1}$density)		proportion of proton (%)
	neutron	proton	
Jungfraujoch	48.5	5.59	11.5
ASTEP	23.4	2.49	10.6
Preston	5.07	0.36	7.1

Table 4.2: The integral atmospheric flux density of protons and neutrons above 10 MeV

Table 4.2. It can be seen that the proportion of protons is decreasing against altitude. As only 1 in million neutrons is registered by the detector, the experiment time may be relatively long. However, at Preston (approximately at sea level), it's still as high as 7.1%. Monte Carlo simulations of ISEEM at Jungfraujoch suggested that when the event threshold is 8 fC (the charge generated by 0.18 MeV of a particle's kinetic engery), the proton induced event rate is higher than the rate induced by neutrons [124]. This is because the event detection threshold is too low, therefore many events generated by proton direct ionisation are detected.

The CCD (KAF-0402E) used in the life testings of this work has a relatively thick sensitive region (about 20μm), thereby small angle incident protons can easily generate events. One of the methods to deal with that is to increase the event detection threshold. However, a large number of real neutron events would be removed as well. A CCD with a thinner sensitive region could be used; however, the event rate would be reduced.

4.2 The characteristics of ISEEM in SSER testing

ISEEM used a CCD as the sensitive element to detect the stopping ions that are mostly generated by nuclear reactions taking place near or in the CCD's active region. As one type of semiconductor, the CCD also suffered from the three

problems discussed in section 4.1.

4.2.1 Alpha contamination in ISEEM

Two experiments took place in the laboratory of the University of Central Lancashire to evaluate the alpha contamination of the KAF-0402E and the KAF-6303E. Comparing with the alpha event rate, the neutron and proton event rates of ISEEM at this location are negligible [72]. The measurement of KAF-0402E was undertaken by Török [130]. A 12 times larger CCD (KAF-6303E) is examined in this work to compare with the data of KAF-0402E. It was suspected that most of the alpha came from CCD's coverslip. Therefore, in this work, a CCD was tested with and without the coverslip.

Fig. 4.2 shows the charge collection spectra of the measurements. Two spectra are normalized at 8 fC. Both CCDs have a peak at about 100 fC, which is the deposition of about 5 MeV ionizing radiation. Very likely, those peaks are events of alpha particles, because only alpha decay may contribute a peak in this region. Neutron and proton events do not have a peak at 100 fC, as shown in Fig. 4.6. However, the peak of the KAF-6303E is higher than that of the KAF-0402E. The event rate of the KAF-0402E with coverslip is $3.11\,\mathrm{cm^{-2}d^{-1}}$ (i.e. 75 events in 74 days). The event rate of the KAF-6303 with and without the coverslip is $3.64\,\mathrm{cm^{-2}d^{-1}}$ (i.e. 158 events in 8.5 days) and $3.28\,\mathrm{cm^{-2}d^{-1}}$ (i.e. 251 events in 15 days), respectively. The event rates in all those experiments are similar. It's appeared that the coverslip is not a significant source of alpha particles. The alpha particles are from the sensor itself or the bonding wires.

4.2.2 Angular effect in ISEEM

ISEEM has been tested in beams for angular dependence by Török [130]. Fig 4.3 is the experimental results of ISEEM at TRIUMF and LANSCE. In this figure, the data from TRIUMF are closed, from LANSCE are open. All experiments yielded similar event cross-sections for the KAF-0402E. Event cross sections are

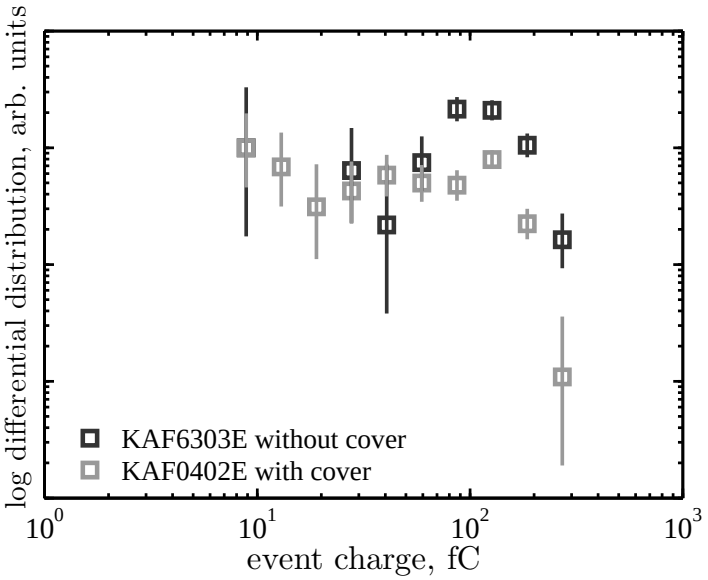

Figure 4.2: Charge collection spectra at sea level, 95% CI

almost constant when the angle changes. The angles were tested from 0°to 90°. Very likely, most of the neutrons at the high altitude laboratory strike ISEEM in this range, because there is solid rock underneath the laboratory.

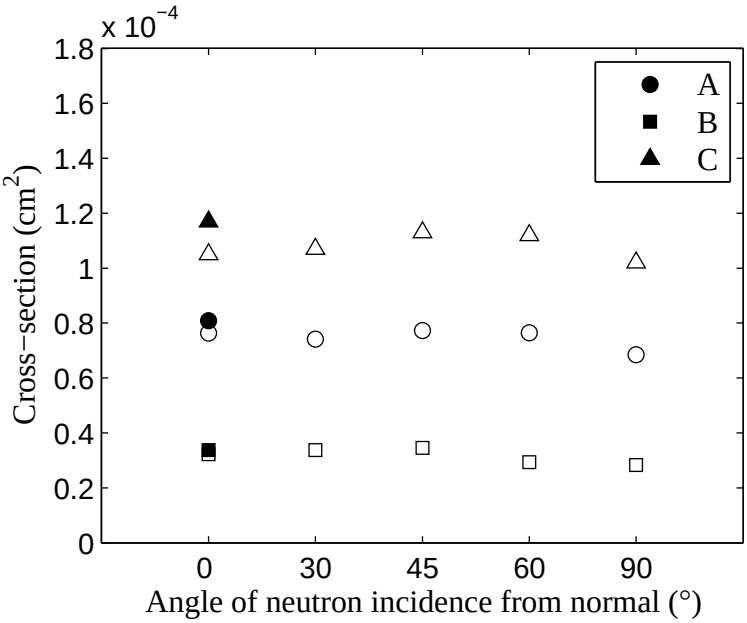

Figure 4.3: Measurement of ISEEM sensitivity of incident angles, TRIUMF are closed, LANSCE are open, A, B and C are different type of CCDs, after [130]

Work in this project has been carried out to investigate the mechanism of this characteristic of CCDs. It showed that the CCD coverslip and substrate have

a very similar cross-section, thereby they compensated each other to provide a quasi-isotropic response to neutrons.

4.3 Life testing results of ISEEM

ISEEMs have been deployed to two high altitude laboratories to perform SSER testings.

4.3.1 Life testing at Jungfraujoch

ISEEM has been deployed to Jungfraujoch experiment by Török. The data of the Jungfraujoch is published in 2007 [72]. The raw event rate is $1.66\,\mathrm{d}^{-1}$. And the event rate at Preston laboratory is about $0.99\,\mathrm{d}^{-1}$. The neutron flux density at Preston is approximately one tenth of Jungfraujoch. Moreover, the thicker roof at the Preston site further attenuate the energetic cosmic ray. Therefore it's concluded that almost all events in the Preston dataset are the product of alpha particle contamination. The rate of cosmic-ray induced events Jungfraujoch is estimated to be approximately $0.67\,\mathrm{d}^{-1}$.

4.3.2 Life testing at ASTEP

In this work, a re-engineered ISEEM gathered 6 months data at ASTEP. There are three runs. They are tabulated in Table 4.3. Event pixels were defined as those above 2.5 fC(DN 300). Events were defined as those at least 8 fC(ΣDN 961). Results are therefore directly comparable to those from Jungfraujoch [72].

Table 4.3: ISEEM runs at ASTEP

run ID	pixel detection threshold	event threshold		raw events	filtered events
	(DN)	(DN)	(ΣDN)		
1	100	300	961	80	30
2	50	300	961	20582	35
3	50	300	961	64016	214

Run001

From 29/11/2007 22:46 to 17/12/2007 17:17, duration 17 days, 18 hours, 31 minutes

Duration of this run is 1.535×10^6 seconds. The event detection threshold of this run is 100DN. 80 raw events are recorded. Applying a pixel filter DN of 300 doesn't reduce events. Applying ΣDN filter level of 961 reduces events to 30. As shown in Table 4.3, relatively few raw events were measured. Very likely, the pixel detection threshold is too high.

Run002

From 17/12/2007 17:20 to 10/01/2008 11:50, duration 23 days, 18 hours, 30 minutes

The pixel detection threshold was reduced to increase raw events. Duration of this run is 2.054×10^6 seconds. The event detection threshold of this run is 50DN. 20582 raw events are recorded. Applying a pixel filter DN of 300 reduces events to 104. Applying ΣDN filter level of 961 reduces events to 35.

Run003

From 10/01/2008 12:01 to 08/05/2008 13:24, duration 119 days, 1 hour, 23 minutes

Duration of this run is 1.028×10^7 seconds. The event detection threshold of this run is 50. 64016 raw events are recorded. Applying a pixel filter DN of 300 reduces events to 479. Applying ΣDN filter level of 961 reduces events to 214.

The amplifier gain was set to 2 in these three runs. One gray level of the pixel represents 52 electronic charges. The charge collection spectra of ASTEP, Jungfraujoch and LANSCE are compared in Fig. 4.4. The spectra are normalised to the area under the range from 8 fCto 32 fC. The error bars show 95 % confidence

intervals. False alarm peaks (between about 40 fC and about 200 fC) induced by radioactive contaminations are observed at both ASTEP and Jungfraujoch. The event rate at ASTEP was about $1.74\mathrm{d}^{-1}$; at Jungfraujoch it was about $1.66\mathrm{d}^{-1}$. As the neutron flux density at Jungfraujoch is higher than the flux density at ASTEP, the event rates indicated that the radioactive contaminations in the CCD used in ASTEP dataset is more serious than that in the CCD used at Jungfraujoch.

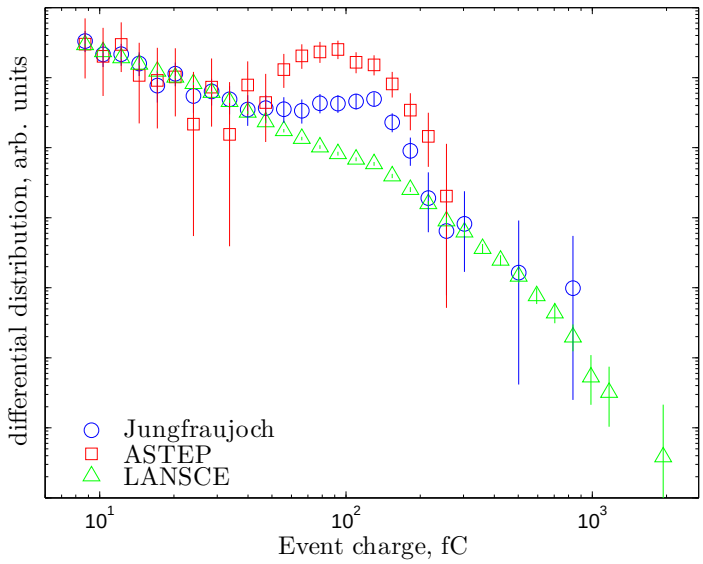

Figure 4.4: Jungfraujoch, ASTEP and LANSCE charge collection spectra

The QARM [24] calculated integral neutron flux density above 2 MeV (the threshold energy) at ASTEP and Jungfraujoch is 3.16×10^{-2} and $6.55 \times 10^{-2}\,\mathrm{cm}^{-2}.\mathrm{s}^{-1}$, respectively. And the integral proton flux density at ASTEP and Jungfraujoch is 2.53×10^{-3} and $5.67 \times 10^{-3}\,\mathrm{cm}^{-2} \cdot \mathrm{s}^{-1}$, respectively. Therefore the neutron and proton induced event rate at ASTEP is expected to be about half of the rate at Jungfraujoch. Events, in which the charge is less than 40 fC, are mostly induced by neutrons and protons. The event rates of these events at Jungfraujoch and ASTEP are tabulated in Table 4.4. 68 % confidence intervals are shown. The measurements are consistent with the QARM prediction.

	event count	time (day)	event rate (day^{-1})
Jungfraujoch	224	371.5	$0.603^{+7.1\%}_{-6.6\%}$
ASTEP	39	160.5	$0.243^{+18.6\%}_{-19.3\%}$

Table 4.4: Small event occurrence rate at ASTEP

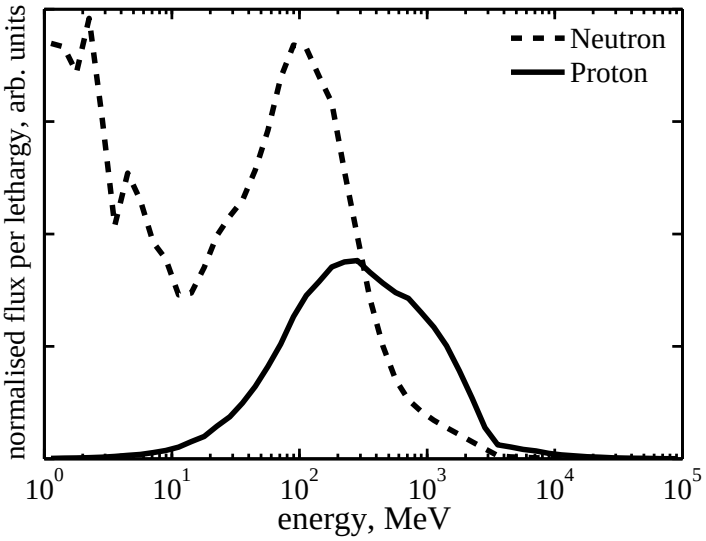

Figure 4.5: Particle spectra at Jungfraujoch, QARM calculation

4.4 Simulation and analysis

The response of ISEEM at Jungfraujoch are simulated and analyzed in this work. The measured alpha event spectrum at Preston was assumed to be the characteristic at Jungfraujoch. The neutron and proton effects at Jungfraujoch were simulated using the predicted spectra of QARM. The simulated spectra are shown in Fig. 4.5.

The cross-sections at Jungfraujoch is calculated using Equation 2.5, as for LANSCE. The integral flux density of downwards neutrons and protons above 10 MeV is $4.24 \times 10^{-2}\,\mathrm{cm}^{-2} \cdot \mathrm{s}^{-1}$ and $5.17 \times 10^{-3}\,\mathrm{cm}^{-2} \cdot \mathrm{s}^{-1}$, respectively. To simplify the work, all particles were assumed to be incident normally on the aluminium enclosure and the CCD. Table 4.5 shows the event rates of the three main

charge-inducing mechanisms: direct ionisation from cosmic-ray protons, nuclear reactions from cosmic-ray neutrons, and direct ionisation from contaminating α particles. Because the main proton interaction mechanism is direct ionisation, they have a higher event cross-section than neutrons although the flux density is lower. In consequence, the event rates due to protons and neutrons are close (at the 8 fC threshold). The estimated total event rate from protons and neutrons combined is $0.946\,\mathrm{d}^{-1}$. This result is 41% over our measurement. As shown in Table 4.5, the simulated Jungfraujoch neutron event rate is $0.384\,\mathrm{d}^{-1}$. Compared with the LANSCE event rate [62], of about $32\,\mathrm{s}^{-1}$, the corresponding acceleration factor is 7.2×10^6.

The simulated angle of incidence for protons was $0\,^\circ$. A larger proton incident angle would greatly affect the simulation result as the longer paths would lead to increased cross-section and a broader charge spectrum. However, Johnston et al. [131] have studied the angular effect in some optocouplers whose active region depth was close to that in our CCD. Their calculations showed that the increased shielding effect at larger angles of incidence compensated for the angular effect. Likely, the ISEEM aluminium enclosure, along with the lightweight laboratory roof at Jungfraujoch, could do similarly.

The significant event sources in Jungfraujoch are the alpha contamination, proton direct ionisation and neutron secondaries. The corresponding event charge spectra are shown in Fig. 4.6. The α-particle contamination spectrum shows a wide range below about 300 fC with a peak around 100 fC. The proton direct ionisation charge spectrum follows a power law below about 40 fC. The shape of the neutron event charge spectrum at Jungfraujoch has the same characteristic as that from neutron beam trials, and the largest events exceed 1 pC.

Combining the spectra in Fig. 4.6 results in the data shown in Fig. 4.7. The measured and simulated data agree quite well, although the calculated curve exceeds the measured data at the lowest energies. This might be due to an error in the treatment of the shielding at Jungfraujoch, as discussed above, or else in

Table 4.5: Simulated event rates at Jungfraujoch

reaction type	cross-section (cm^2)	event rate (day^{-1})
neutrons	1.05×10^{-4}	0.384
primary protons	1.12×10^{-3}	0.500
secondaries of proton	1.38×10^{-5}	0.062

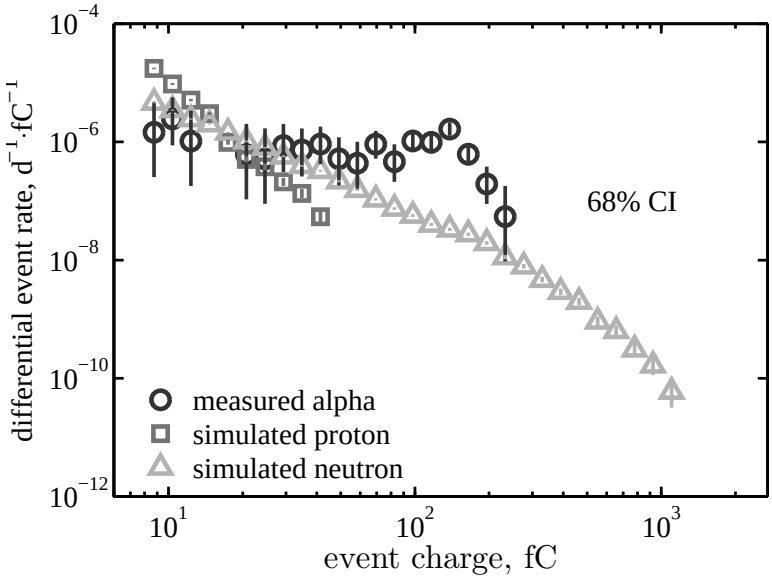

Figure 4.6: Event charge distribution by type at Jungfraujoch

the estimation of CCD parameters, such as the active depth.

4.5 Discussion

This chapter discussed the performance of ISEEM in the life testings. Results of the life testings at Jungfraujoch and ASTEP were compared.

ISEEM has a relatively strong response to neutron and is insensitive to neutron incident angle. This feature makes it a good tool to measure the neutron influence to causing SEE in atmosphere. However, the CCDs used in this work have strong alpha contamination. A long term underground experiment is needed

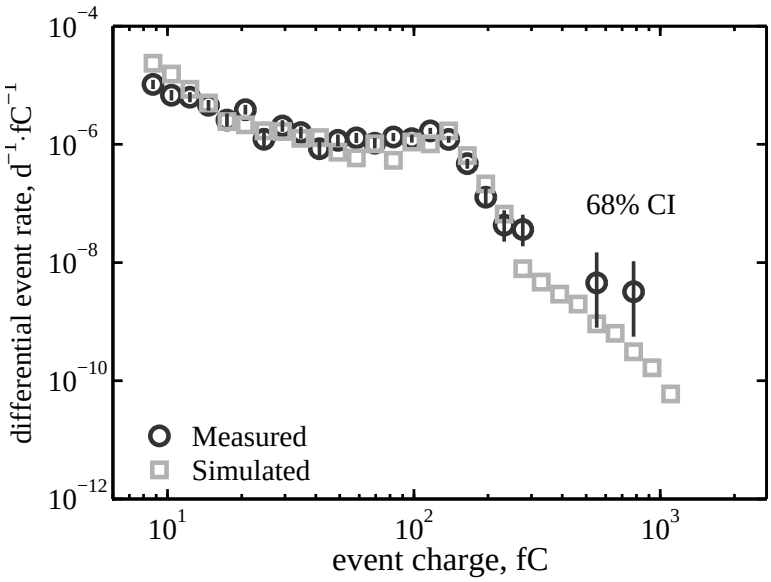

Figure 4.7: Event charge distribution comparison at Jungfraujoch

to measured the alpha event rate of a CCD, before placing it in atmosphere to measure cosmic ray induced events. As indicated in Table 4.5, the event rate of KAF-0402E based ISEEM is very low. The neutron event rate at Jungfraujoch is $0.384\,\mathrm{d}^{-1}$. Using a CCD with a thicker active region in the place of KAF-0402E, the event rate could be enhanced. However, such a device would be more sensitive to proton direct ionization. Using a CCD with thinner active region in the place of KAF-0402E, the proton effect could be suppressed. However, the neutron event rate would be reduced at the same time. To summarize, CCD based ISEEM is not an ideal proxy device to measure the influence of neutron fields in causing single event effect in the atmosphere. A better proxy device is introduced in Chapter 6.

Chapter 5

The improvements of the imaging SEE monitor

Two improved versions of ISEEM were developed in this work. Both versions are re-engineered based on the system developed by Török and his co-workers. [64]

5.1 The improved ISEEM version one

A single board computer was used instead of a desktop PC. The overall system is packaged into an aluminium box as shown at Fig.5.1. Therefore this monitor is more convenient to carry to remote location, such as ASTEP. This portable monitor has been taken to ASTEP[34] for a 6-month life testing in 2007.

5.2 The improved ISEEM version two

This re-engineered ISEEM communicates with host computer via the USB [1] 2.0 bus instead of the PCI bus to reduce the board size and power consumption. The system composed of a mother board that serves the requests of host computer and a daughter board to interface the analog system which can operate up to six CCDs. The dimensions of these boards are consistent with the PC/104+ form fac-

[1] USB, Universal Serial Bus

Figure 5.1: The portable ISEEM at ASTEP (44.6°N, 5.9°E, 2550m above sea level)

tor. Therefore this system is compatible with a wide range of PC/104+ products, such as power supplies, single board computers, and enclosures. This ISEEM has been used for one month at Preston to characterize the alpha contaminations of a CCD.

5.2.1 System overview

The system block diagram is shown in Fig. 5.2. The overall system is controlled by the host computer through a USB controller. The CCD integration interval is timed by a timer in the host computer. When the timer ticks, a clock pattern generator in an FPGA is triggered to drive the content of the CCD to the ADC for the digitization. The digitized data of a full frame are transferred into an external SDRAM. This SDRAM acts like a large FIFO buffer to accelerate the data transfer rate from this system to the host computer. Once the clock generator asserts the "done" signal, the host computer requests the USB controller to upload the data stored in the SDRAM. The enhanced performance of using an SDRAM is discussed in next paragraph.

Since the USB bus needs a relatively long period of time to establish each data

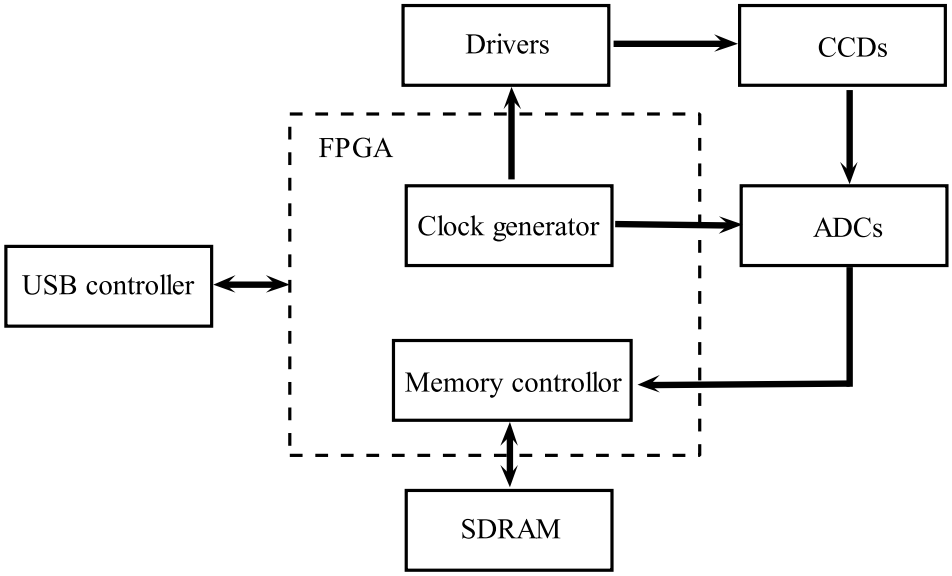

Figure 5.2: System block diagram

transmission process, the transfer rate can be very low if the payload is small. Fig. 5.3 shows the rate as a function of payload size. The data transfer rate can be as high as 38 MB/s when the payload is larger than several MB. This rate drops to less than 0.1 MB/s when the payload is larger than several kB. Therefore, a 32MB SDRAM was used in this system to ensure a high data transfer rate.

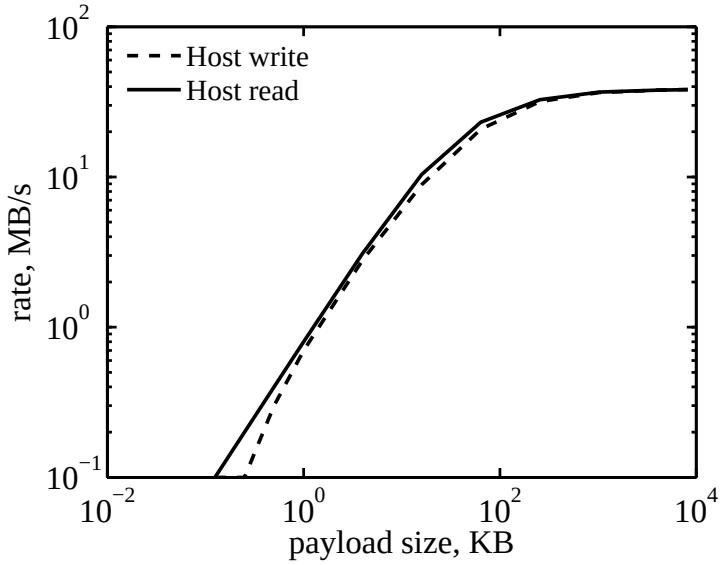

Figure 5.3: USB data transfer rate, data are from [132]

5.2.2 The mother board and improved subsystems

The mother board is a 4 layer design. Only a 5V input voltage is required to supply this board. The PCI [2] and ISA [3] bus sockets in the PC/104+ stack are only used for powering and securing this board. An alternative 5V external power rail could be selected by one of the on board jumper.

Figure 5.4 illustrates the block diagram of the mother board. A XEM3005[132] FPGA module is used to control the programable voltage references (PVRs), SPI bus, CCD video processors and provide programable IOs. The clock of the FPGA can be adjusted from several MHz to 400MHz by changing internal registers of the PLL [4]. The CCD video processor is comprised of two ADCs [5] (AD9822). There are six video input channels in total. The maximum pixel sample rate for each ADC is 12.5 MSPS[6].

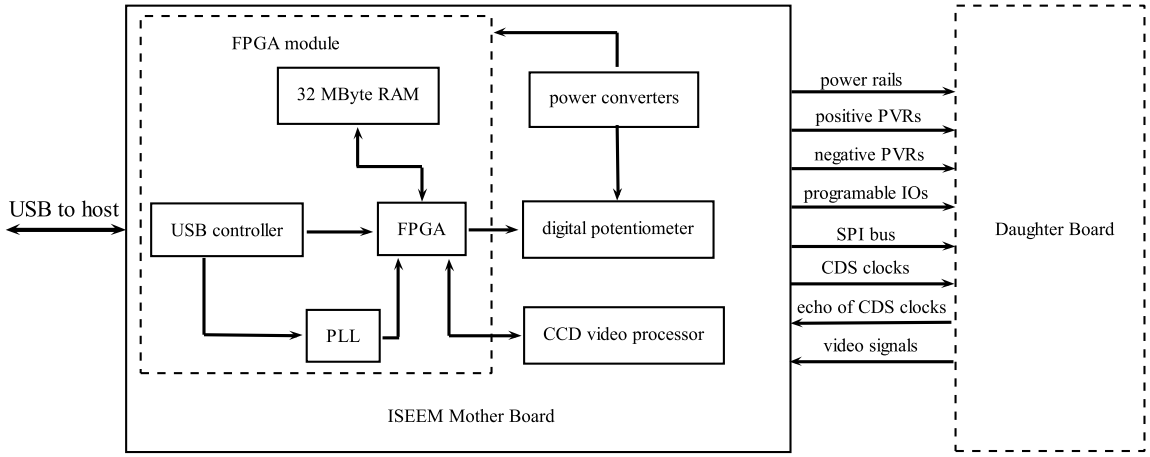

Figure 5.4: Mother board block diagram

[2]PCI, Peripheral Component Interconnect

[3]ISA, Industry Standard Architecture

[4]PLL, Phase-locked loop

[5]ADC, analog to digital converter

[6]MSPS, Mega Sample Per Second

5.2.3 The echoing method to synchronize CCD video signal

Correlated double sampling (CDS) is the method used to remove the reset noise in the CCD video. The CDS processes of AD9822 (a CCD signal processor from Analog Devices) is illustrated in Fig. 5.5. A video signal is processed by a CDS enabled ADC. Two voltages are sampled for each charge package. The first sample is measured before a reset clock. This sample is the sum of the charge package and the dark signal. The second sample is measured right after the reset when the charge package is clear. It's the raw dark signal. The subtraction of those samples then results the charge package.

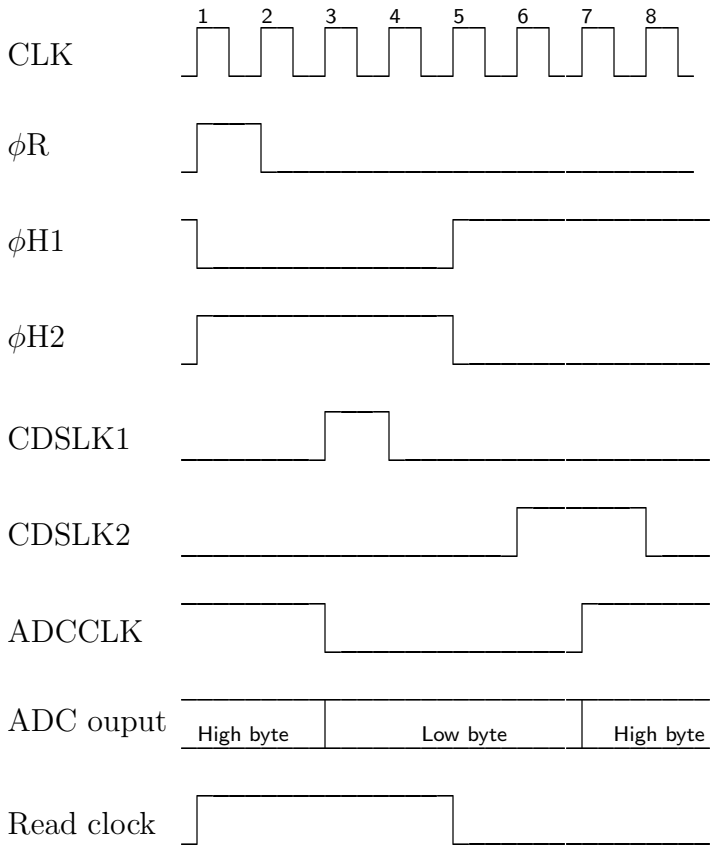

Figure 5.5: RAM based generator generated waveforms for reading CCD pixels

It can be seen that the timing needs to be very precise. Otherwise, noise will be introduced. However, the required precision is difficult to satisfy in the

accelerated neutron testings. In such testings, a CCD and the ADC along with other digital components are separated by a long cable, so that neutrons don't influence the digital system. However, the cable delay makes it difficult to generate an accurate readout waveform.

Fig. 5.6 illustrates the method used to solve this problem in the original ISEEM. Both of the CCD driving clock (from the digital system to CCD) and the CCD video signal (from the CCD to the digital system) are delayed by the long cables. To synchronize the video with the sampling processes, the CDS clocks are delayed (i.e. twice the cable delay) by a programable delay circuit. This design has a very good performance. But it only works for a fixed-length cable. Once the length of the cable changes, the in-circuit delay needs to be re-programmed.

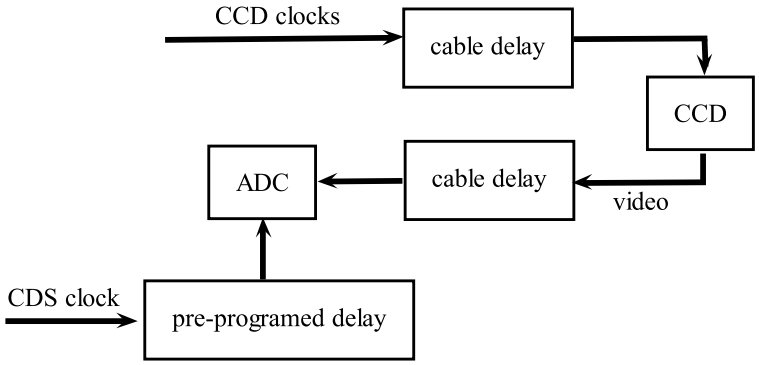

Figure 5.6: Solution of cable delay in old ISEEM

A fixed length cable is a inconvenience in the experiments. It has to be as long as possible in order to be used at different facilities. The block diagram of the new design is shown in Fig. 5.7. The CDS clocks are then encoded as the effective CDS clock. The information carried in the CDS clocks are compressed into the single signal to optimize the use the cable. In this design, when the digital system trying to read the CCD video, it sends the reset, vertical and horizontal clocks to the daughter board along with the effective CDS clock. The daughter board echos back the effective CDS clock and the video signal. In this way, video can be properly synchronized, and not affected by the propagation delay introduced

by the long communication media. Therefore, an arbitrary length of cable could be used. Moreover, the complex in-circuit delay is replaced by a pairs of wires.

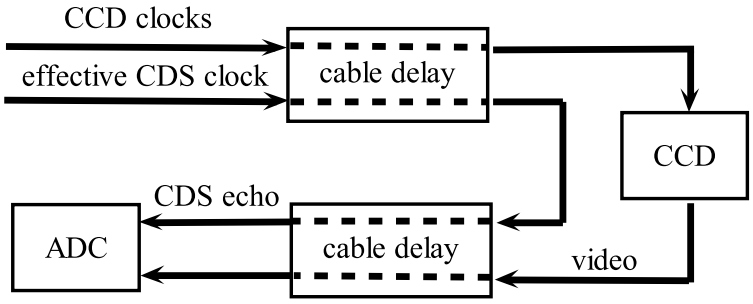

Figure 5.7: The new solution of cable delay

5.2.4 Programmable voltage references

Driving a CCD requires many different levels of voltages for biasing. To optimize the system performance in harsh environmental conditions, digital potentiometers are used to replace mechanical trimmers. In the life testing of Jungfraujoch, some of the gathered images are blurred because temperature variation affected the voltage of the mechanical trimmers. One digital potentiometer along with an operational amplifier formed a programable voltage reference (PVR). There are some advantages in using digital potentiometers in such applications. First of all, they are insensitive to temperature. Also they can work in a wide voltage ranges. The AD5263 was chosen as the replacement. This device can output the voltage with less than 1% error when operating in the voltage divider mode at a temperature between -40°C and 125°C.

A section of the negative PVR schematic (an AD5263 and one set of output buffers) is shown in Fig. 5.9. For the device AD5263, terminals A, B are connected to two different voltages, and terminal W is the divided voltage of the voltage across A and B. The level of the voltage at W is adjustable via the SPI bus. The desired negative voltages are buffered by a couple of operational amplifiers to invert the voltage and drive the capacitive load. The main challenge of this design is to avoid the operational amplifier oscillations and reduce the voltage

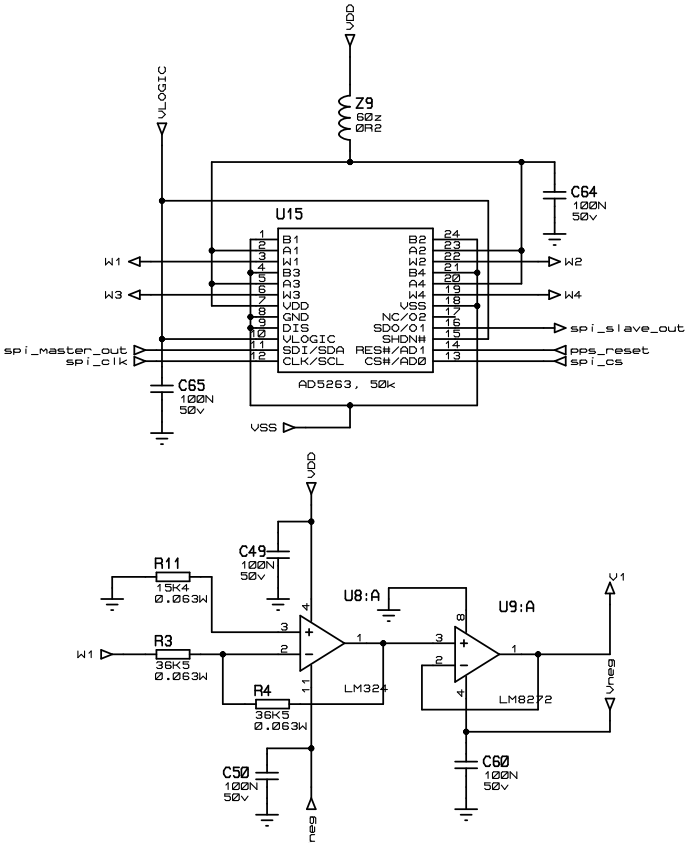

Figure 5.8: Schismatics of the programable voltage references

overshoot. The LM8272 is used as the buffer. This amplifier is designed to drive unlimited capacitive loads without oscillations. Additionally, the output of the digital potentiometer can be adjusted in several small steps, instead of one big step, to avoid large voltage swing at the output. Therefore large voltage overshoots can be avoided.

The measured voltage output of the PVRs are shown in Fig. 5.9. The x axis is the value held by internal register of the digital potentiometer which represents the scale of the output voltage. The voltages across positive and negtive PVRs are 15V and -10V, respectively. The output of the negative PVR is saturated at about 200.

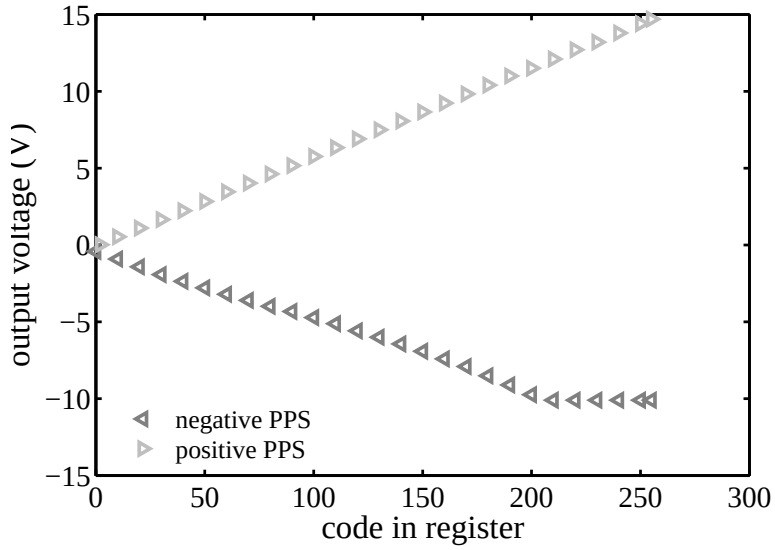

Figure 5.9: Measured voltage output of programable voltage references

class name	description
USBController	control ISEEM and manage data flow
ImageLable	image real time display
PixelExtractor	event pixel extraction
EventProcessor	event pixel grouping
EventListManager	event storage and read back
Spectroscope	event profile characterization
Logger	global system logging

Table 5.1: ISEEM software package classes

structure name	description
AFrame	raw data of one frame
AnEventPixel	one event pixel
AnEvent	one event, comprised of AnEventPixel
EventsInAFrame	events from the same frame, comprised of AnEvent
EventListFile	all events in a trial, comprised of EventsInAFrame

Table 5.2: ISEEM software package data structures

5.2.5 Host side software

The host computer software was developed based on the Qt toolkit. Qt is a open-source cross-platform application and UI framework. The code written in Qt can be compiled in most of the operating system without changing any source code. The latest version of the software was tested on Windows and Linux.

5.3 Summary

This section introduced two versions of re-engineered ISEEM. Version one has been taken to a high altitude laboratory for a 6-month life testing. Version two was used to measure CCD alpha contaminations in the Preston laboratory for a month.

Chapter 6

Design of an extended Bonner sphere as a proxy device

The Imaging Single Effect Monitor (ISEEM) response in accelerated artificial beams have been studied to characterise the neutron induced charge transients in semiconductors. It has been deployed to Jungfraujoch and ASTEP for long term experiments to attempt to validate the neutron prediction models. However, the alpha impurity behaved as the dominant event source even at the mountain altitudes [72]. Simulations also suggested the noise of low energy proton direct ionization intermingled with the neutron events below 40 fC. (see Chapter 4) Increasing the event detection threshold could remove most of the proton noise, but would further extend the experiment time.

A Bonner sphere was studied as an alternative proxy. In the natural environment, the Bonner sphere spectrometer is one of the instruments widely used to measure the neutron spectrum [38, 45–48]. This type of detector was first described in 1960 [40]. They have very good sensitivity for thermal, epithermal, and fast neutrons, and isotropic angular response [38]. MCNP and MCNPX are the most common tools used to calculate the Bonner sphere response in most studies (i.e. [38, 45–48]).

Comparing with the ISEEM's passive mechanism to measure neutron fluence

(see Chapter 2), Bonner spheres measure neutron fluence in a aggressive way. Energetic neutrons are firstly thermalized by the modulator surrounding a thermal neutron sensor, and then detected. A variety of thermal neutron sensors could be used as the sensitive element in a Bonner sphere. The last section of this chapter will discuss the suitable application of different types of sensors.

In 2009, a paper by Garny et al. was published [42] to claim that GEANT4 is as good as MCNPX. They compared the simulation results of MCNPX(version 2.6.6) and GEANT4 (version 8.2) in their work. Gold foil was used as the sensitive element. They firstly compared the simulated neutron energy spectra in a 6 inch sphere produced by 1 MeV monoenergetic primary neutron using GEANT4 and MCNPX. There is a 2mm gold foil placed in the center of the sphere. Simulated spectra are overlapped for most of the energies, except that MCNPX had about 5% higher prediction for the neutrons in the energy range between 0.03 and 0.1 eV. Then, they calculated the response of this sphere to primary neutrons at 1 eV and 1 MeV. Results show that the largest discrepancy is about 7%. Such agreements may be considered very good.

The conventional Bonner sphere has a very weak response to neutrons above 100MeV. To increase the high energy response, high-Z materials were proposed to be added to the sphere by Hsu et al.[44]. Such a sphere is so called an "extended Bonner sphere". The mechanism of improved response is that high-Z materials act as neutron multipliers at high energy. Examples of high-Z material neutron productions are shown in Fig. 6.1. Data for ^{56}Fe(n,xn) and ^{208}Pb(n,xn) are from ENDF. Threshold energies of iron and lead are about 0.8 and 2 MeV, respectively. Lead has a higher cross-section than iron above 4 MeV. The cross-section difference increases with the increase of energy. Lead has more than a 7 times higher cross-section than iron above 30 MeV. Therefore, lead should have a better performance than iron in terms of the enhancement of the response.

In the progress of this work, an 18 inch extended Bonner sphere showed similar response to neutrons in the energy range from 1 MeV to 1 GeV as ISEEM in

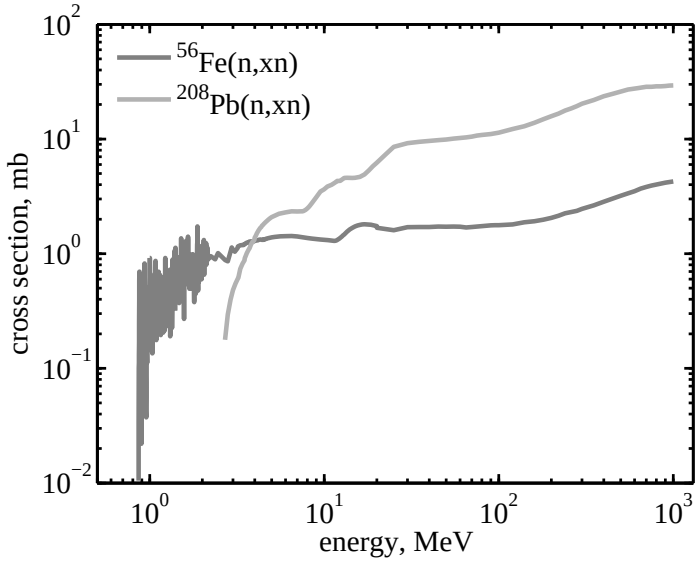

Figure 6.1: Neutron productions of ^{56}Fe and ^{208}Pb, data from ENDF 6

simulation. The response function of this sphere was found in the paper of Hsu et al. [44] in 1994. Like microelectronics, large extended Bonner spheres (larger than 15inch) are not sensitive to thermal and epithermal neutrons, and have a constant response to the high energy neutrons. More analysis can be found in section 6.1.

This Chapter introduces the development and verification of a GEANT4 simulation to study the extended Bonner sphere in section 6.1. Only the response of the a ^{3}He counter was simulated, the response of the electronics to pulses generated by the ^{3}He counter are not included. Section 6.2 studies the mechanism of simulating semiconductor response by a Bonner sphere. Section 6.3 applies the knowledge acquired in section 6.2 to simulate the response of ISEEM to neutrons. In this work, a ^{3}He counter was chosen as it has high efficiency for detecting thermal neutron. This feature is a particular advantage in the natural environment.

6.1 Verification of the simulation code

The methods and physics models introduced in Garny et al. [42] are listed in Table 6.1, and re-produced for simulation. The correctness of the developed code is verified by comparing with the response function of the 18 inch extended Bonner sphere, which was published in Hsu's paper [44]. In Hsu's work, they simulated a set of extended Bonner spheres in different configuration. One sphere of size 18 inch is also simulated in this work to compare with its calculated response function by Hsu. Both of the simulations calculate for a ^{3}He counter with 4 atmospheres pressure. There is lead shell in between 3 inch to 4 inch in this sphere. Except for the sensor and lead shell, the rest of the volume is pure polyethylene. The densities of lead and polyethylene are 0.92 and 11.34 g.cm^{-3}, respectively. However, this work simulates a ^{3}He counter with diameter of 5cm instead of the 3.2cm counter used in Hsu's work. Therefore, the simulated response function is expected to be higher than the function of Hsu's. The major reason for calculating a different size counter is that Hsu et al. didn't mention how they applied the event threshold. This makes numerical comparison difficult. Today, the 5cm ^{3}He counter counters are commonly used in extended Bonner spheres [38, 46–48], as this counter is the largest counter commercially available. The simulated results also indicate the orders of magnitude of the event rate enhancement over ISEEM. Therefore, only the shapes of the response functions were compared.

The geometry of the Bonner sphere is shown in Fig. 6.2. The thermal sensor in this sphere is a 5cm ^{3}He counter, with a gas pressure of 4 atmospheres. In some applications, especially for small size ^{3}He counters, to minimize the wall effect, some heavier gas is added to the sensor to increase the stopping power. In this simulation, the gas is taken to be 100% ^{3}He . ^{3}He has a high cross-section to capture thermal neutrons, and generates a secondary tritium and proton. The total kinetic energy of the secondaries is 0.764 MeV. This reaction can be expressed as

$$n + {}^3He \rightarrow {}^3H + {}^1H + 0.764MeV$$

Process	Energy	G4 class name	G4NeutronHP-dataset
Elastic	<4eV	G4NeutronHPThermalScattering	ThermalScatteringData
	<20MeV	G4NeutronHPElastic	ElasticData
	>19MeV	G4LElastic	-
Inelastic	<20MeV	G4NeutronHPInelastic	InelasticData
	>19MeV	G4BinaryCascade	-
Fission	<20MeV	G4NeutronHPFission	FissionData
	>19MeV	G4LFission	-
Capture	<20MeV	G4NeutronHPCapture	CaptureData
	>19MeV	G4LCapture	-

Table 6.1: GEANT4 models to simulate Bonner sphere response to neutrons

In this simulation, charged particles which deposit more than 24% of the peak energy in a event (i.e. 0.183 MeV) were considered as events. This threshold is previously used in the literature [46–48].

All reactions below 20 MeV were modelled by HP (high precision) models which are data driven. A corresponding dataset for the HP models is shown in Table 6.1.

Nine energies were simulated from 0.1 MeV to 1 GeV. The response function from GEANT4 simulations is compared with the function from Hsu's original paper in Fig. 6.3. These two functions were normalized at 0.1 MeV. It can be seen that, the agreement below 10 MeV is good. A more rapid rise from GEANT4 over MCNP is observed. It begins at 50 MeV, which is lower than the 250 MeV in the MCNP simulation. Observations can be understood as when the neutron production effect is weak, agreement is good. Otherwise, agreement is poor. Therefore, the neutron production models used in these two simulations should correspond to the discrepancy at high energy. Fig. 6.4 shows the neutron production in lead. The cross-section rapidly increases at high energy. At high energy, secondary neutrons are the dominant effective particle. According to this figure, the response function from GEANT4 seems to be more reliable, because it has a similar shape with the neutron production for lead above 50 MeV. The

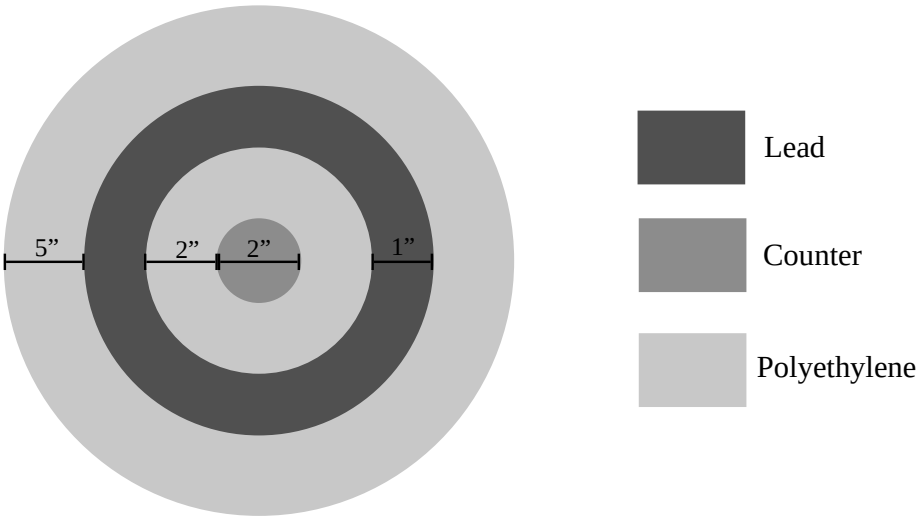

Figure 6.2: Geometry of simulated 18 inch extended Bonner sphere (not to scale)

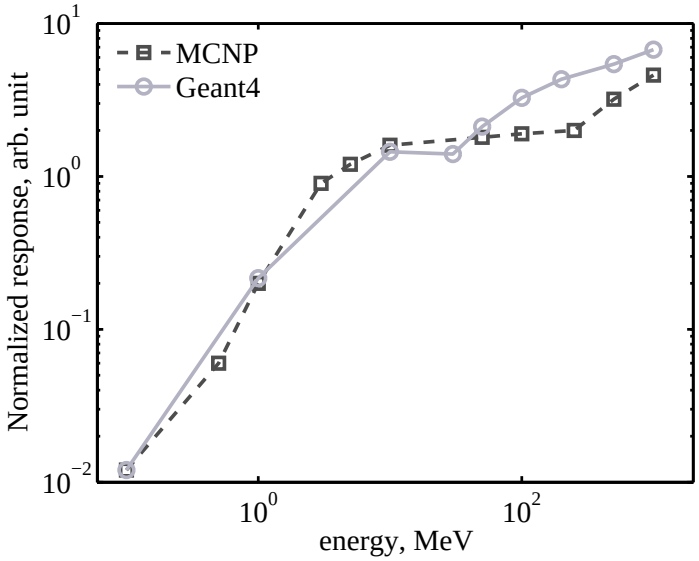

Figure 6.3: Comparisons response functions given by GEANT4 (this work) and MCNP (from [44])

MCNP simulation was done in 1990s. Probably, the cascade model used in that simulation was not as good as the more recent model used in GEANT4.

The event cross-section of ISEEM at high energy is the order of $10^{-5}\,\mathrm{cm}^2$, while it is of the order of $1\,\mathrm{cm}^2$ for this 18 inch extended Bonner sphere. Comparing less than 0.4 events per day of ISEEM at Jungfraujoch high altitude laboratory, this Bonner sphere can measure about 40000 events every day.

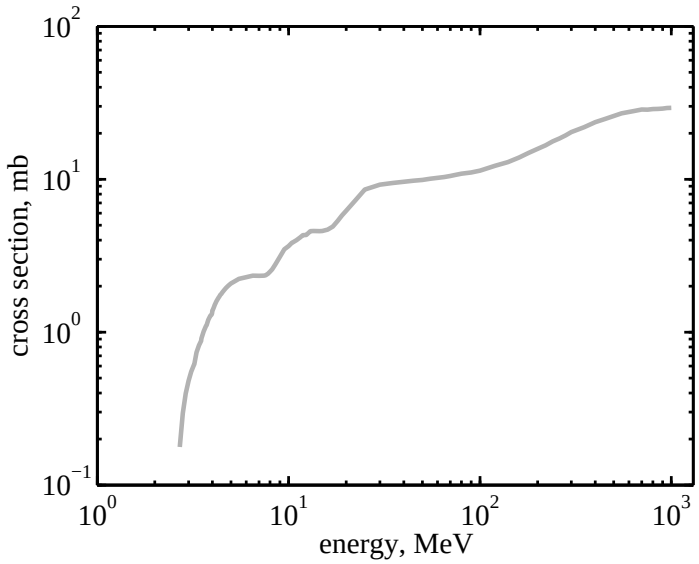

Figure 6.4: Neutron production on lead

6.2 Sphere configurations and their effect to the response function

The event cross-section of a semiconductor from threshold energy to infinity can be split into three regions by its characteristics.

These regions are referred as the lower, medium and higher energy region in the following text, and they are denoted as region A, B and C, respectively, in Fig. 6.5. Fig. 6.5 is the desired response function of an extended Bonner sphere.

The event cross-section in the lower energy region rises from the threshold energy to the lower boundary of the medium energy region. The event cross-section characteristic in this region is that the slope is constant on log-log scale. The medium energy region is between the lower and higher energy region. The cross-section slope in this region diminishes against the increase in energy towards few at the saturated energy of this device. Above the saturated energy, the event cross-section is a constant value, or a "limiting cross-section". Of course, a Bonner sphere is sensitive to thermal and epithermal neutrons. For large spheres, the sensitivity is very low, but still higher than ideal. In practice, a spherical layer of thermal neutron absorber may be added to the Bonner sphere to minimize this

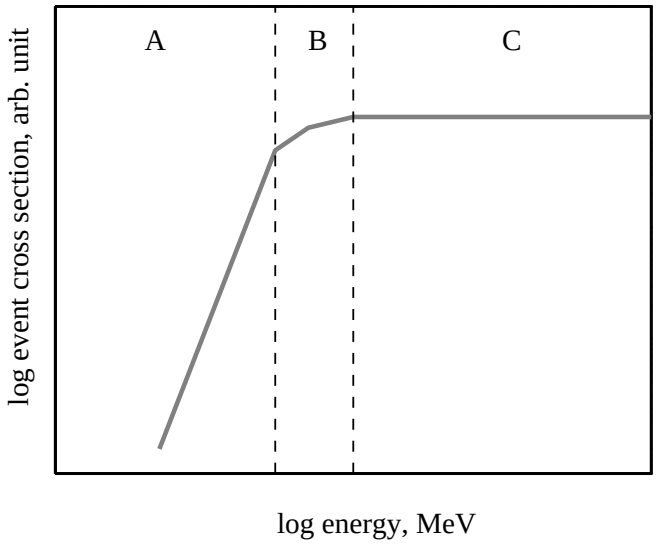

Figure 6.5: The ideal response function of a Bonner sphere as the proxy of a microelectronics device

effect. This is not discussed in this chapter, and will be studied in future work.

This section discusses modelling of the response function of an extended Bonner sphere in the three regions classified above. Methods also are discussed for adjusting the Bonner sphere configuration to match a semiconductor response better. The next section will apply these methods in iterations to approximate the response function of a Bonner sphere to ISEEM's event cross-section. However, the size and weight of this Bonner sphere is not optimized.

6.2.1 Modelling the response in the lower energy region

A conventional Bonner sphere has a sharp global peak response to neutrons at a certain energy. The rapid rise of this peak can be used to model the rise of the event cross-section of a semiconductor at the lower energy region. The position of the peak depends on the thickness of polyethylene. Example peak locations are tabulated in Table 6.2. Data were taken from the simulated results in [42] and [44]. It can be observed that with the increase of sphere size, the peak is moved to higher energies. For a Bonner sphere larger than 9 inch, the width (in unit of MeV) of the peak is a nearly a constant. The peaks' upper cut off energies are

Table 6.2: Peak response of Bonner spheres to neutron energy

sphere diameter (inch)	peak location (MeV)
1.3	2×10^{-6}
5.5	0.6
7	1
10	3
15	7
18	13

all at about 50 MeV.

A conventional Bonner sphere uses pure polyethylene to thermalize neutrons. However, the rise of the peak is not as rapid as in semiconductors. For example, an 18 inch Bonner sphere response increases 7 times in the energy range between 1MeV to 10MeV as shown in Fig. 6.3. ISEEM's response increased about two orders of magnitude in the same region as shown Fig. 6.7.

6.2.2 Modelling the response in the higher energy region

The event cross-section of a semiconductor device in the higher energy region is approximately a constant value. It is so called "limiting cross-section". For an extended Bonner sphere, the response in this region increases against energy, because metals have a high neutron production at higher energy, as can be observed in Fig. 6.1. Energetic neutrons can generate multiple neutrons, and sometimes more than one neutron can be detected at almost the same time. Therefore, pulse pile-up is expected to occur. With the increase of a energy, the possibility of observing pulse pile-up is increased.

For example, the pulse height spectra on 100 MeV and 1 GeV neutrons of a 18 inch extended Bonner sphere is shown in Fig. 6.6. All peaks in this figure locate at 0.764 MeV and at multiples of that energy. Each 0.764 MeV is the energy deposition of the reaction ^{3}He(n,p)T. Because the light ions of this reaction have

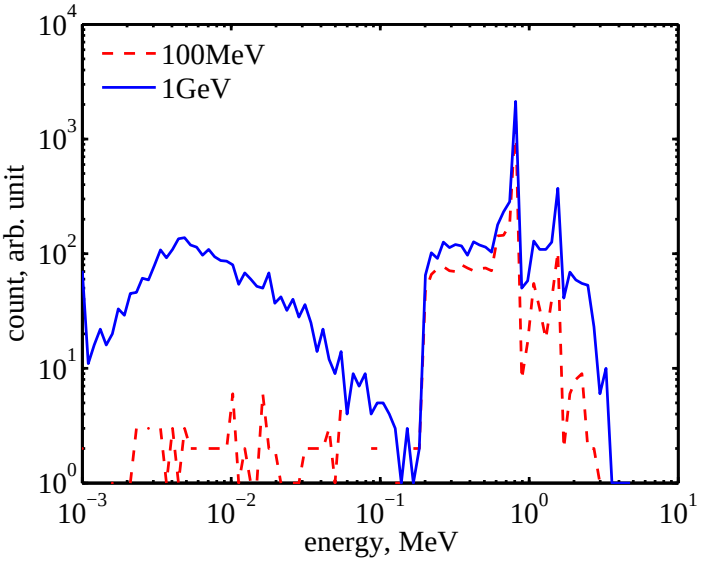

Figure 6.6: 100MeV and 1GeV neutrons pulse height spectra

a relatively long range in gas, many of them can hit the wall of the Helium-3 counter. As they are not stopped in the gas, a large portion of their energy is deposited in the wall. This wall effect can be observed in Fig. 6.6. Before each peak, there is a constant response followed by a rapid rise. The response peaks of 1 GeV neutrons are higher than the peaks of 100 MeV neutrons, similar results were observed in many other cases. This provides an opportunity to correct the overall response function of the Bonner sphere. Neutron production becomes significant above 30 MeV. Therefore, the lower limit energy of this region is set to 30 MeV. It's also the upper limit energy of the median energy region.

The correction of the response function is

$$\sigma'(E) = \sigma_1(E) - C_1\sigma_2(E) - C_2\sigma_3(E) \tag{6.1}$$

where $\sigma'(E)$ is the corrected response function, and $\sigma_1(E)$, $\sigma_2(E)$ and $\sigma_3(E)$ are the response of the events higher than 0.1834 MeV,1.5280 MeV and 2.2920 MeV respectively. C_1 and C_2 are the correction coefficients. Their value can be determined by comparing the event cross-section of the aimed semiconductor and $\sigma(E)$ and $\sigma_h(E)$ of the Bonner sphere. Double, and triple events become significant above 30 and 100 MeV, respectively. Therefore, the term $C_1\sigma_2(E)$ and $C_2\sigma_3(E)$

are used to mainly suppress the overresponse above 100 MeV. An example estimation of C_1 and C_2 for ISEEM is given in section 6.3.

6.2.3 Modelling the response in the median energy region

For an extended Bonner sphere, neutron modulation and heavy metal neutron production are the major detection mechanisms at the lower energy region and higher energy region, respectively. The median energy region is the transition region, where the major detection mechanisms switch over. The volume and location of the lead shell in the extended Bonner sphere are the important factors to properly model the semiconductor's event cross-section.

6.3 Designing the extended Bonner sphere as a proxy for ISEEM

In this section, Monte Carlo simulations were applied to identify the design parameter of a Bonner sphere to simulate ISEEM response to neutrons. The simulation results were used to estimate the event rate enhancement of the extended Bonner sphere against ISEEM in the fields defined by JESD89A[6], ANITA, and LANSCE. It has been observed that the enhancement is almost a constant at all these fields. The time requirement of ISEEM life testing could be reduced from several years to several days, if the Bonner sphere is used in the place of ISEEM.

The cross-section of ISEEM in Table 3.4 is used as the benchmark. It's illustrated in Fig. 6.7. The event threshold is 8 fC. The calculated event rate, by folding the functions with the neutron spectra, results a discrepancy of 20% with our measurements at all the neutron beams. Overall, the accuracy is good. This response function is divided into three regions by two energies at 10 MeV and 50 MeV.

The upper limit energy of the lower energy region is effected by the size of the sphere as discussed in section 6.2.1. 15 inch and 18 inch spheres may be both

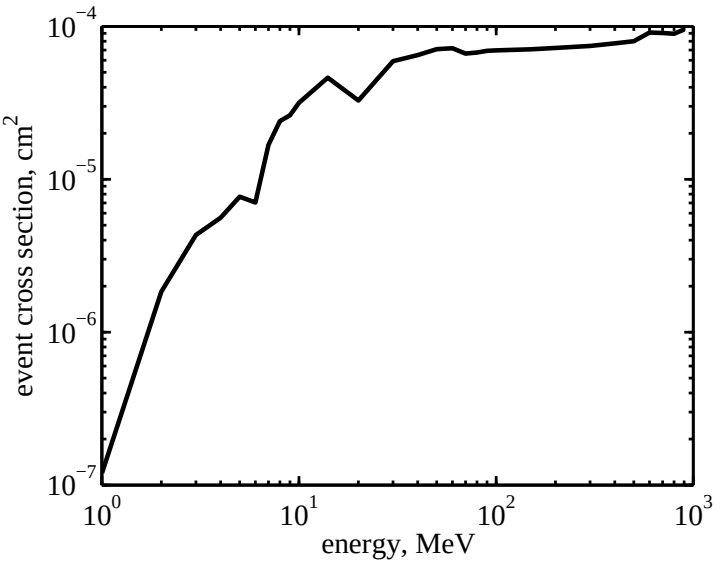

Figure 6.7: The response function of ISEEM

	D (inch)	D_1 (inch)	D_2 (inch)	D_3 (inch)	D_4 (inch)
Type A	18	2	0	1	7
Type B	18	2	0	1.5	6.5
Type C	18	2	0	2	6
Type D	18	2	1	1	6

Table 6.3: Extended Bonner sphere geometry parameters

valid. However, to re-use the simulated data of the 18 inch sphere, the size of the Bonner sphere is taken to be 18 inch.

A half inch thick lead shell was added to the sphere. The simulated response is shown in Fig. 6.8. The response in the median energy region has an increasing negative slope instead of a decreasing positive slope. This indicated that the volume of lead shell is not large enough. To investigate how much lead is adequate, a set of configurations were simulated. The geometry is shown Fig. 6.9. The parameters in this figure are tabulared in Table. 6.3.

In type A to C, the lead shells contact with the counter. The thickness of the lead shell is increased by 0.5 inch each type. The lead shell in type D has a gap of 1 inch before the counter.

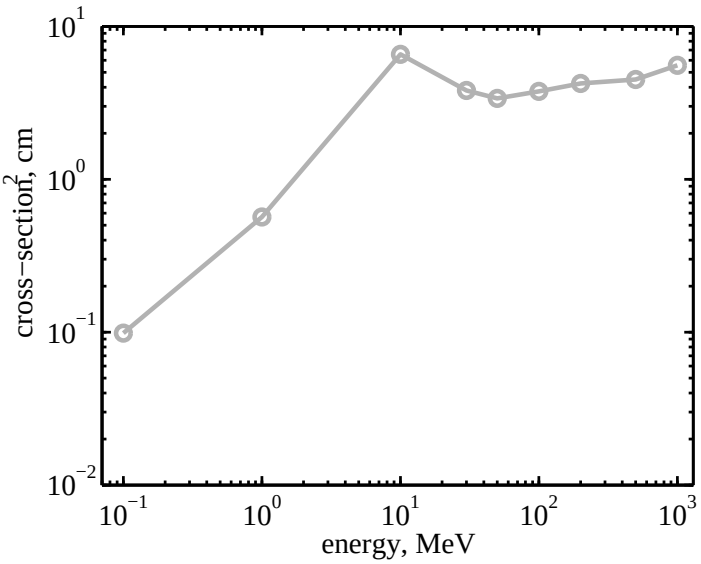

Figure 6.8: Response function of a 18 inch Bonner sphere with half a inch lead shell

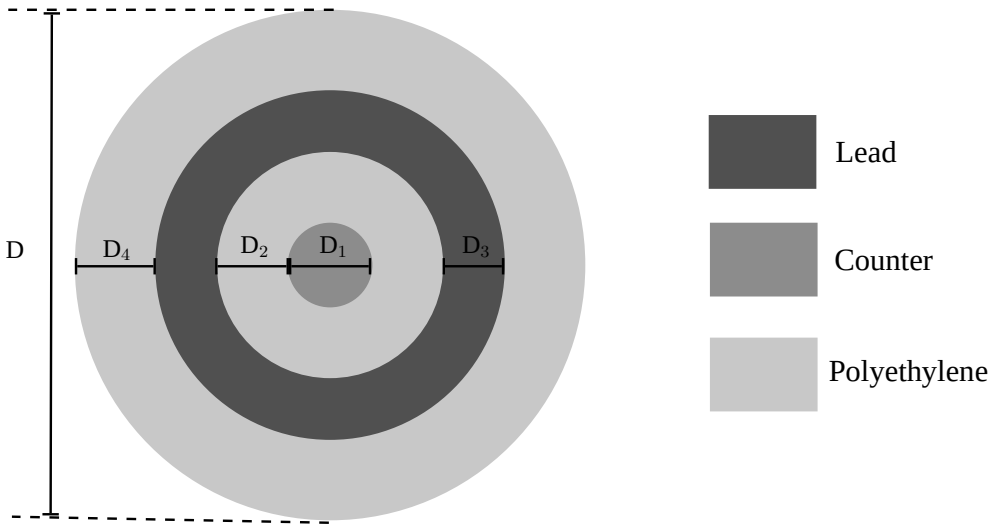

Figure 6.9: The simulated Bonner sphere geometry (not to scale)

Fig. 6.10 shows the response functions of type A to type D. The absolute value of the slope of transition region (10 to 50MeV) is decreased towards few when a thicker lead shell is used. Dips were observed in the functions of type A and B in this region. Therefore, they are not the ideal candidates. Type B and D contain 15kg and 16kg of lead, respectively. However, type D shows a smoother transition in this region. This may be due to the fact that the lead shell contacts with the sensor. In that case, low energy neutrons generated by 10 MeV neutrons

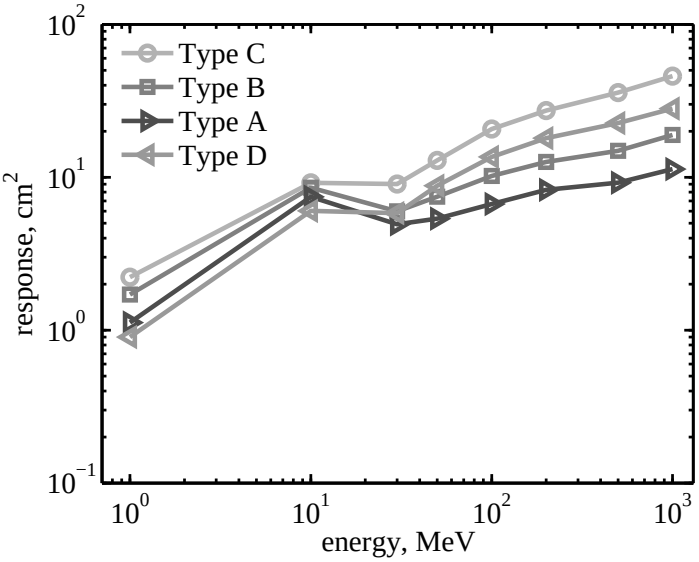

Figure 6.10: Response functions Type A to D

had higher probability to enter the counter. Both type C and type D can provide a smooth transition in this region, these two spheres have very similar shape, and type D contains less lead than type C (i.e. about 24kg). Type D is lighter, and seems less sensitive to neutrons below 1MeV. Therefore, type D was chosen to be used.

The response functions defined in Equ. 6.1 of a type D Bonner sphere is shown in Fig. 6.12. The response is corrected according to Equ. 6.1 with $C_1 = 4$ and $C_2 = 0$. Those coefficients can be adjusted in another iteration of the design, if the agreement of the proxy and target device are not satisfied in specified fields.

6.4 Evaluating the performance of the extended Bonner sphere

The event rate of the Bonner sphere and ISEEM in different fields are tabulated in Table 6.4. The response enhancement factors, H, were calculated as

$$H = \frac{\int \sigma_b(E)\varphi(E)\, dE}{\int \sigma_i(E)\varphi(E)\, dE} \tag{6.2}$$

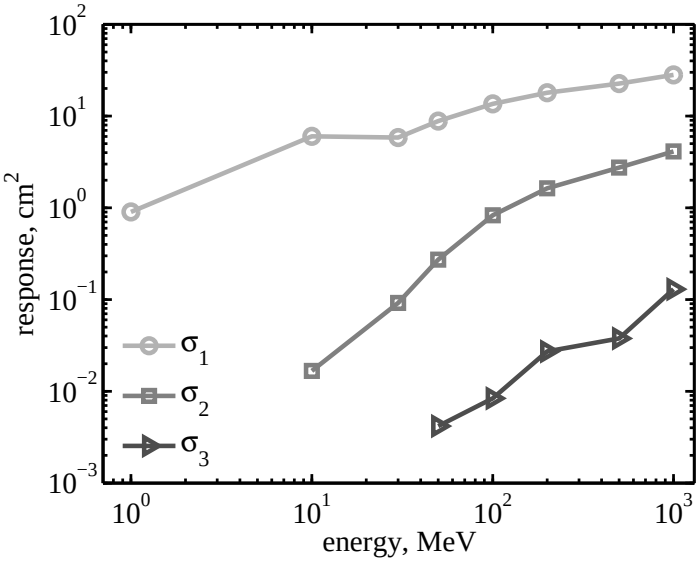

Figure 6.11: The response of type D

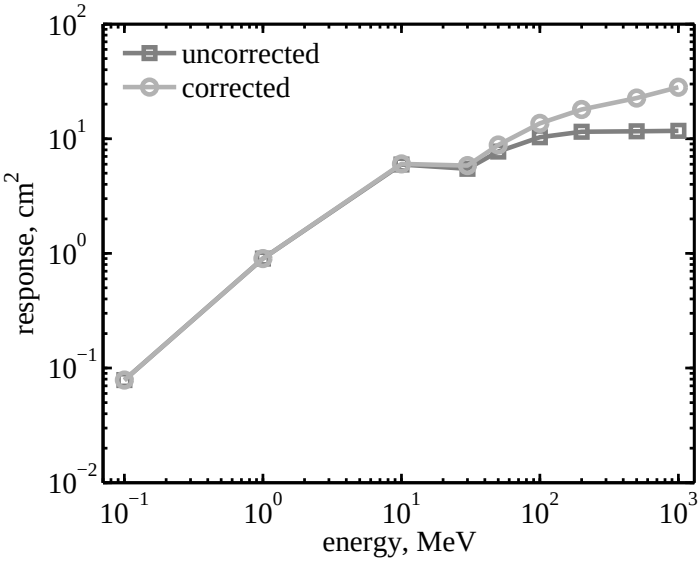

Figure 6.12: The corrected response of type D

where σ_b and σ_i are the response functions of the Bonner sphere and ISEEM, respectively. $\varphi(E)$ is the neutron spectrum. Simulations didn't cover the whole energy range. The cross-sections, which were not calculated, were assumed equal to the cross-section of the closest calculated energy. This assumption is almost valid at high energy. However, it overestimates the influence of thermal neutrons for the Bonner sphere, because a large Bonner sphere has a very weak response for thermal neutrons. The neutron spectrum at Jungfraujoch is predicted by

	Bonner event rate ($10^6\,\mathrm{cm}^2$)	ISEEM event rate (cm^2)	enhancement (10^5)
Jungfraujoch	4.54×10^{-7}	2.87×10^{-6}	1.57
LANSCE	5.16	32.2	1.60
ANITA	8.54	50.0	1.71
TRIUMF	23.5	164	1.43
TSL25MeV	1.20	7	1.71
TSL108MeV	12.9	98.2	1.32
TSL180MeV	1.71	11.5	1.48

Table 6.4: Simulated event rates of the extended Bonner sphere and of ISEEM in different neutron fields

QARM; it is from 10^{-6} MeV. All other fields are artificial beams, the neutron spectra begin from 0.1 MeV. The equilethargic contributions at Jungfraujoch are compared in Fig. 6.13. Though the Bonner sphere's response to thermal neutrons is overestimated, those neutrons have very weak contribution to the overall response. Contributions from the neutrons in the range of 0.1 MeV to 1 MeV are very weak. Comparing with ISEEM, the Bonner sphere has more events contributed by neutrons in the range between 1 MeV to 10 MeV. This effect was explained in section 6.2.1. Later analysis shows that this effect is too weak to influence the results. However, it can be further reduced by increasing the thickness of the polyethylene.

The enhancement factors of the Bonner sphere are very close to a constant. At TSL QMN 25MeV, the constant is 1.32×10^5 which is 15% lower than the enhancement at Jungfraujoch. That's because this Bonner sphere is relatively poor to simulate the response below the saturated energy.

6.5 Discussion

A ^{3}He counter based extended Bonner sphere is purposed to be a proxy device of microelectronics. Methods of designing an appropriate sphere is introduced. To

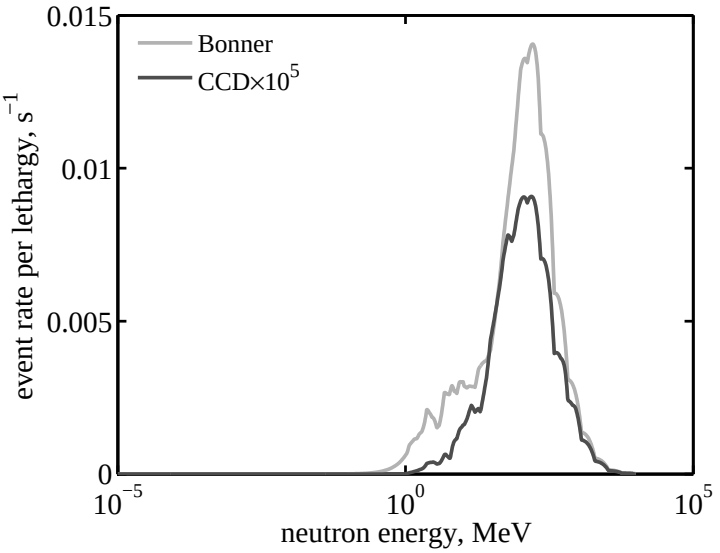

Figure 6.13: The equilethargic contribution of type D Bonner sphere as a function of energy

take an example, one sphere is designed as the proxy of ISEEM. Actually, any thermal sensor can be used in the place of the ^{3}He counter. Sensor replacement may only effect the detection efficiency but not the shape of the response function. Therefore, it is possible to use metal foil in a high flux density field, while using gaseous counters in a low flux density neutron field.

It is notable that the Bonner sphere was used as a proxy device for another system. In the 1960s, during Bramblett, Ewing, and Bonner's investigation [40] of this new spectrometer, they have found that the 12 inch sphere had a similar shape as the dose equivalent delivered per neutron as a function of energy. This sphere was the only detector that could be used to estimate neutron dose in a wide energy range (from thermal to MeV) at that time [43].

Chapter 7

Summary and discussion

7.1 Contribution to knowledge

This work is aimed at investigating an alternative method (see section 1.6) of estimating the real-time SEU rate of a microelectronic device.

In the first year of study, a preliminary analysis of the measured data in accelerated beam and atmospheric radiation environment contributed to a part of a paper [72] published in the European Conference on Radiation and its Effects on Components and Systems (RADECS) 2007. Efforts were made to improve the system performance of the original ISEEM to make it more convenient for life testings. Two re-engineered systems were later (in 2008) used in a 6-month life testing at ASTEP [34] (section 4.3.2), and for a life testing at Preston to evaluate the alpha contamination effects of a large CCD (section 4.2.1), respectively.

The second year of study was dedicated to develop models to simulate interactions of neutrons with ISEEM. A preliminary CCD model (Chapter 2) based on GEANT4 was constructed. Some device parameters were determined from openly published data, and some others were derived from the alpha particle irradiations of the CCD. The simulated results were presented at in RADECS 2008 [**?**]. An extended revision of this paper [124] was published in the IEEE Transaction on Nuclear Science (TNS). This model overestimated event cross-sections in accel-

erated neutron fields by 14.0% to 116%, because of inaccurate charge collection behaviour in this model. Later, methods were evaluated to improve the performance of the preliminary CCD model. During that time, it was realized that ISEEM has poor performance in atmospheric radiation environment due to more that half of the events being caused by alpha contaminations or low energy proton direct ionization. The activities of searching for a better proxy device started.

An improved CCD model (Chapter 3) was successfully developed in the third year of study. The discrepancy of simulated and measured event cross-sections at LANSCE and TRIUMF were smaller than 30%, which is within the quoted error of the facilities. The calculated response function of ISEEM was used in Prokofiev et al. [129] to calculate the LANSCE-equivalence flux density of TSL ANITA and in Platt et al. [133] as an example device to evaluate the fidelity of neutron beam spectra for accelerated testing. A paper introducing this improved model has been accepted for presentation at RADECS 2010. The response function of an extended 18 inch Bonner sphere introduced by Hsu et al. [44] attracted much attention. The shape of the response function is very similar to the response shape of memory devices. The predicted performance of the large extended Bonner sphere as a proxy device of semiconductor devices was analyzed in Chapter 6. The results will be presented at RADECS 2010.

7.2 Further work

7.2.1 Evaluating the simulated ISEEM response

Calibration trials are needed to evaluate the correctness of the simulated response functions and event rate. However, there is no monoenergetic neutron source above 19 MeV. To calibrate the response function of a device at higher energy, quasi-monoenergetic neutron beams are usually used. For example, one set of Bonner sphere spectrometers developed by the Physikalisch-Technische Bundesanstalt (PTB) was calibrated by monoenergetic neutrons from 1.2 keV

to 19 MeV, and by a quasi-monoenergetic neutron beam at 60 MeV. [61] At higher energy, the calibration becomes difficult. For SRAM's response function, it's common to used proton sources as proxy to neutrons at those energies.

In this work, no trials were designed to calibrate the response function. Simulations show better agreement with measurements in white neutron beams than in quasi-monoenergetic neutron beams. (See Table 3.3 and Table 3.1) It's interesting to observe that the discrepancy of simulated and measured cross-section at TSL QMN increases when the mono-energetic peak moves to higher energy. In that beam, high energy neutrons are the dominant component, and the binary cascade model in GEANT4 is used to model the interactions of the high energy neutrons with matter. Researchers from Vanderbilt University have noted that GEANT4 underestimates the production of secondaries of 173 MeV protons on aluminium, and similar results were obtained for other residual nuclei [99]. Further investigations are needed to evaluate the correctness of the response function.

7.2.2 Designing a smaller shield for the Bonner spheres

The extended Bonner sphere is firstly proposed by Hsu et al. in 1997. [44] Their main purpose of developing this device was to enhance the response of a Bonner sphere at high energy. Chapter 6 designed a 18 inch Bonner sphere which has similar response to ISEEM. However, the size may be larger than the beam areas in many accelerated beams. This may limit the usage of it. Techniques can be investigate to shrink the size. The thick polyethylene used in this sphere is to minimize the impact from low energy neutrons. Thermal neutron absorbers, which are the materials that have very high cross-section for thermal neutron capture, can be added in the sphere to achieve a similar effect at a smaller size. A similar method can be found used in the extended REM counter [134], which uses a thin layer of borated materials in the middle to attenuate neutrons moderated by polyethylene.

7.2.3 Experimental validation of the indirect method for accelerated testing

The indirect accelerated testing method was not experimentally validated in this work. Further work may focus on this. The real-time neutron event rate of a memory device predicted by this method can be evaluated by the actual results from SSER testings. As SSER testings are very expensive, results from the literature can be used. There are many SSER testings which have taken place in high altitude laboratories. For example, Autran et al. [34, 37] published real-time neutron event rates of many devices at Altitude SEE Test European Platform (ASTEP). Proxy spheres can be made for some of those devices. The indirect accelerated testing method can be used to predict the event rates. Results given by Autran can justify the performance of this new accelerated method.

Appendix A

Publications

1. Z. Török, S. P. Platt, and Xiao Xiao Cai, "SEE-inducing effects of cosmic rays at the high-altitude research station Jungfraujoch compared to accelerated test data", RADECS 2007, September 2007

   Preliminary analysis of the measured data at LANSCE and Jungfraujoch was contributed to this paper
2. Cai Xiao Xiao, S. P. Platt, Chen Wei, "Modelling neutron interactions in the Imaging SEE Monitor", RADECS 2008 The model introduced in Chapter 2 was published in this paper
3. Extended paper of paper 2 was selected to be published in IEEE Transactions on nuclear science, Vol. 56, no. 4, Aug 2009
4. Alexander V. Prokofiev, Jan Blomgren, Mitja Majerle, Ralf Nolte, Stefan Röttger, Simon P. Platt, Cai Xiao Xiao, and Andrey N. Smirnov, "Characterization of the ANITA neutron source for accelerated SEE testing at The Svedberg Laboratory", NSREC 2009

   Simulated response function of ISEEM from the improved model, which is introduced in Chapter 3, was used in this paper to calculate the LANSCE-equivalent flux density of ANITA
5. S. P. Platt, A. V. Prokofiev, Cai Xiao Xiao , "Fidelity of energy spectra at neutron facilities for single-event effects testing", IRPS 2010

Simulated response function of ISEEM from the improved model was used as an example to evaluate neutron spectra.

6. Cai Xiao Xiao, S. P. Platt, "Improved simulation model for Imaging Single Event Effects Monitor", submitted to RADECS 2010

   The improved ISEEM model (Chapter 3) was published in RADECS 2010

7. Cai Xiao Xiao, S. P. Platt, S. Monk, "Simulating the neutron response function of the Imaging SEE monitor by a Bonner sphere", RADECS 2010

   Work described in Chapter 6 has published in RADECS 2010

Bibliography

[1] J. Wallmark and S. Marcus, "Minimum size and maximum packing density of nonredundant semiconductor devices," *IRE Proc.*, vol. 50, pp. 286–298, 1962.

[2] D. Binder, E. Smith, and A. Holman, "Satellite anomalies from galactic cosmic ray," *IEEE Trans. Nucl. Sci.*, vol. NS-30, p. 2675, 1975.

[3] J. Pickel and J. Blandford, "Cosmic ray induced errors in MOS memory cell," *IEEE Trans. Nucl. Sci*, vol. NS-30, p. 1166, 1978.

[4] T. C. May and M. H. Woods, "Alpha-particle-induced soft errors in dynamic memories," *IEEE Trans. Electron Devices*, vol. 26, no. 1, pp. 2–9, 1979.

[5] C. S. Guenzer, E. A. Wolicki, and R. G. Allas, "Single event upset of dynamic RAMs by neutrons and protons," *IEEE Trans. Nucl. Sci.*, vol. 26, no. 6, pp. 5048–5052, 1979.

[6] *Measurement and Reporting of Alpha Particle and Terrestrial Cosmic Ray-Induced Soft Errors in Semiconductor Devices*, Std. JESD89A, Oct. 2006. [Online]. Available: http://www.jedec.org/download/search/jesd89a.pdf

[7] J. F. Ziegler and W. A. Lanford, "Effect of cosmic rays on computer memories," *Science*, vol. 206, p. 776, 1979.

[8] G. C. Messenger and M. S. Ash, *Single Event Phenomena.* Chapman and Hall, 1997.

[9] W. S. Boyle and G. E. Smith, "Charge coupled semiconductor devices," *Bell Sys. Tech. J.*, vol. 49, pp. 587–593, 1970.

[10] J. R. Srour, "Radiation effects R & D in the 1970s: A retrospective view," *IEEE Trans. Nucl. Sci*, vol. 41, pp. 2660 – 2665, 1994.

[11] D. F. Barbe, J. M. Killiany, and H. L. Hughes, "Effects of gamma radiation on charge-coupled devices," *Appl. Phys. Lett.*, vol. 23, p. 400, 1973.

[12] J. M. Killiany, W. D. Baker, N. S. Saks, and D. F. Barbe, "Effects of ionizing radiation in charge-coupled device structures," *IEEE Trans. Nucl. Sci.*, vol. 21, pp. 193–200, 1974.

[13] R. A. Williams and R. D. Nelson, "Radiation effects in charge coupled devices," *IEEE Trans. Nucl. Sci.*, vol. 22, pp. 2639–2644, 1975.

[14] G. W. Autio and M. A. Bafico, "Gamma noise in CCDs," *Infrared Phys.*, vol. l5, p. 249, 1975.

[15] W. Shedd and E. Buchanan, "Transient radiation effects in CCDs," *IEEE Trans. Nucl. Sci.*, vol. 23, pp. 1636–1638, 1976.

[16] C. P. Chang, "Radiation hardened p-surface channel CCDs," *IEEE Trans. Nucl. Sci.*, vol. 23, pp. 1639–1643, 1976.

[17] ——, "Radiation effects in N-buried channel CCDs fabricated with a hardened process," *IEEE Trans. Nucl. Sci.*, vol. 24, pp. 2190–2193, 1977.

[18] N. S. Saks, "Investigation of bulk electron traps created by fast neutron irradiation in a buried N-channel CCD," *IEEE Trans. Nucl. Sci.*, vol. 14, pp. 2153–2157, 1977.

[19] J. R. Srour, S. C. Chen, S. Othmer, and R. A. Hartmann, "Neutron damage mechanisms in charge transfer devices," *IEEE Trans. Nucl. Sci.*, vol. 25,, pp. 1251–1260, 1978.

[20] ——, "Radiation damage coefficients for silicon depletion regions," *IEEE Trans. Nucl. Sci.*, vol. 26, pp. 4784–4791, 1979.

[21] F. W. Sexton, "Measurement of single event phenomena in devices and ICS," *NSREC Short Course*, 1992.

[22] QinetiQ Atmospheric Radiation Model (QARM). [Online]. Available: http://geoshaft.space.qinetiq.com/qarm

[23] F. Lei, A. Hands, S. Clucas, C. Dyer, and P. Truscott, "Improvements to and validations of the QinetiQ atmospheric radiation model (QARM)," in *Radiation and Its Effects on Components and Systems, 2005. RADECS 2005. 8th European Conference on*, 19-23 Sept. 2005, pp. D3–1–D3–8.

[24] ——, "Improvement to and validations of the QinetiQ Atmospheric Radiation Model (QARM)," *IEEE Trans. Nucl. Sci.*, vol. 53, pp. 1851–1858, Aug. 2006.

[25] F. Lei, S. Clucas, C. Dyer, and P. Truscott, "An atmospheric radiation model based on response matrices generated by detailed Monte Carlo simulations of cosmic ray interactions," *IEEE Trans. Nucl. Sci.*, vol. 51, no. 6, pp. 3342–3451, Dec. 2004.

[26] T. Nakamura, M. Baba, E. Ibe, Y. Yahagi, and H. Kameyama, *Terrestrial neutron-induced soft errors in advanced memory devices.* World Scientific Publishing, 2008.

[27] R. Baumann, "Radiation-induced soft errors in advanced semiconductor technologies," vol. 5, no. 3, pp. 305–316, Sept. 2005.

[28] E. Normand, "Single-event effects in avionics," *IEEE Trans. Nucl. Sci.*, vol. 43, no. 2, pp. 461–474, 1996.

[29] T. R. Oldham, S. Murrill, and C. T. Self, "Single event upset of VLSI memory circuits induced by thermal neutrons," *Radiation Effects, Research and Engineering*, vol. 5, p. 6, 1986.

[30] R. Baumann, T. Hossain, E. Smith, S. Murata, and H. Kitagawa, "Boron as a primary source of radiation in high density DRAMs," in *VLSI Technology, 1995. Digest of Technical Papers. 1995 Symposium on*, Kyoto, 1995, pp. 81–82.

[31] H. Kobayashi *et al.*, "Soft errors in SRAM devices induced by high energy neutrons, thermal neutrons and alpha particles," in *Proc. Digest. International Electron Devices Meeting IEDM '02*, 2002, pp. 337–340.

[32] J. Armani, J. Armani, G. Simon, and P. Poirot, "Low-energy neutron sensitivity of recent generation srams," *IEEE Trans. Nucl. Sci.*, vol. 51, no. 5, pp. 2811–2816, 2004.

[33] M. P. Baze and S. P. Buchner, "Attenuation of single event induced pulses in cmos combinational logic," *IEEE Trans. Nucl. Sci.*, vol. 44, no. 6, pp. 2217–2223, 1997.

[34] J.-L. Autran *et al.*, "Altitude SEE Test European Platform (ASTEP) and first results in CMOS 130 nm SRAM," *IEEE Trans. Nucl. Sci.*, vol. 54, no. 4, pp. 1002–1009, Aug. 2007.

[35] H. Kobayashi *et al.*, "Comparison between neutron-induced system-SER and accelerated-SER in SRAMs," in *Reliability Physics Symposium Proceedings, 2004. 42nd Annual. 2004 IEEE International*, 25-29 April 2004, pp. 288–293.

[36] A. Lesea, S. Drimer, J. J. Fabula, C. Carmichael, and P. Alfke, "The Rosetta experiment: atmospheric soft error rate testing in differing technology FPGAs," vol. 5, no. 3, pp. 317–328, Sep. 2005.

[37] J. Autran *et al.*, "Altitude and underground real-time SER characterization of CMOS 65nm sram," *IEEE Trans. Nucl. Sci.*, vol. 56, pp. 2258–2266, 2009.

[38] D. Thomas and A. Alevra, "Bonner sphere spectrometers - a critical review," *Nuclear Instruments and Methods in Physics Research A*, vol. 476, pp. 12–20, 2002.

[39] J. Clem, "Atmospheric yield functions and the response to secondary particles of neutron monitors," *Proc. 26th Int. Cosmic Ray Conf.*, 1999.

[40] R. L. Bramblett, R. I. Ewing, and T. Bonner, "A new type of neutron spectrometerstar," *Nuclear Instruments and Methods*, vol. 9, pp. 1–12, 1960.

[41] R. Bedogni *et al.*, "Characterization of the neutron field at the ISIS-VESUVIO facility by means of a Bonner sphere spectrometer," *Nuclear Instruments and Methods in Physics Research Section A: Accelerators, Spectrometers, Detectors and Associated Equipment*, vol. 612, no. 1, pp. 143 – 148, 2009. [Online]. Available: http://www.sciencedirect.com/science/article/B6TJM-4X66S12-3/2/1a80f08d5cffe15ff92021562e894ae9

[42] S. Garny, V. Mares, and W. Rhm, "Response functions of a Bonner sphere spectrometer calculated with GEANT4," *Nuclear Instruments and Methods in Physics Research Section A*, vol. 604, pp. 612–617, 2009.

[43] G. F. Knoll, *Radiation detection and measurements*, third, Ed. John Wiley & sons, 2000.

[44] H. H. Hsu, K. R. Alvar, and D. G. Vasilik, "A new Bonner-sphere set for high energy neutron measurements: Monte Carlo simulation," *IEEE Trans. Nucl. Sci.*, vol. 41, no. 4, pp. 938–940, 1994.

[45] Y. Uwamino, T. Nakamura, and A. Hara, "Two types of multi-moderator neutron spectrometers: Gamma-ray insensitive type and high-efficiency

type," *Nuclear Instruments and Methods in Physics Research Section A*, vol. 239, pp. 299–309, 1985.

[46] P. Goldhagen *et al.*, "Measurement of the energy spectrum of cosmic-ray induced neutrons aboard an ER-2 high-altitude airplane," *Nuclear Instruments and Methods in Physics Research A*, vol. 476, pp. 42–51, 2002.

[47] P. Goldhagen, J. M. Clem, and J. W. Wilson, "The energy spectrum of cosmic-ray induced neutrons measured on an airplane over a wide range of altitude and latitude," *Radiation Protection Dosimetry*, vol. 110, pp. 387–392, 2004.

[48] M. S. Gordon *et al.*, "Measurement of the flux and energy spectrum of cosmic-ray induced neutrons on the ground," *IEEE Trans. Nucl. Sci.*, vol. 51, no. 6, pp. 3427–3434, 2004.

[49] L. Tommasino *et al.*, "Cosmic-ray neutron spectrometry by solid state detectors," *Radiation Measurements*, vol. 36, pp. 307–311, 2003.

[50] ——, "Passive multidetector stack for the assessment of aircrew exposure," *Environment International*, vol. 22, pp. 115–119, 1996.

[51] M. Chadwick *et al.*, "ENDF/B-VII.0: Next generation evaluated nuclear data library for nuclear science and technology," *Nuclear Data Sheets*, vol. 107, no. 12, pp. 2931–3118, Dec. 2006. [Online]. Available: http://www.sciencedirect.com/science/journal/00903752

[52] K. Shibata *et al.*, "Japanese Evaluated Nuclear Data Library Version 3 Revision-3: JENDL-3.3," *J. Nucl. Sci. Technol.*, vol. 39, p. 1125, 2002.

[53] A. Koning, R. A. Forrest, Y. Rugama, and H. Henriksson, "The JEFF evaluated data project," *Proceedings of the International Conference on Nuclear Data for Science and Technology*, 2007.

[54] Y. Zhang, L. Tingjin, Z. Jingshang, and L. Ping, "Cendl-3: Chinese Evaluated Nuclear Data Library, version 3," *Journal of Nuclear Science and Technology*, pp. 37–39, 2002.

[55] *Russian File of Evaluated Neutron Data (RUSFOND).* [Online]. Available: http://www.ippe.ru/podr/abbn/libr/rosfond.php

[56] J. Ziegler, "Trends in electronic reliability — effects of terrestrial cosmic rays," accessable at http://www.srim.org/SER/SERTrends.htm. [Online]. Available: http://www.srim.org/SER/SERTrends.htm

[57] "ER-2 High altitude airborne science aircraft fact sheets." [Online]. Available: http://www.nasa.gov/centers/dryden/news/FactSheets/FS-046-DFRC.html

[58] T. Nakamura, T. Nunomiya, S. Abe, K. Terunuma, and H. Suzuki, "Sequential measurements of cosmic-ray neutron spectrum and dose rate at sea level in Sendai, Japan," *Journal of Nuclear Science and Technology*, vol. 42, no. 10, pp. 843–853, 2005.

[59] M. Kowatari *et al.*, "Evaluation of geomagnetic latitude dependence of the cosmic-ray induced environmental neutrons in Japan," *Journal of Nuclear Science and Technology*, vol. 44, no. 2, pp. 114–120, 2007.

[60] D. J. Thomas, A. G. Bardell, and E. M. Macaulay, "Characterisation of a gold foil-based Bonner sphere set and measurements of neutron spectra at a medical accelerator," *Nucl. Instr. and Meth.*, vol. 476, pp. 31–35, 2002.

[61] B. Wiegel and A. V. Alevra, "NEMUS - the PTB Neutron Multisphere Spectrometer Bonner spheres and more," *Nuclear Instruments and Methods*, vol. 476, pp. 36–41, 2002.

[62] Z. Török and S. P. Platt, "Application of imaging systems to characterization of single-event effects in high-energy neutron environments," *IEEE Trans. Nucl. Sci.*, vol. 53, no. 6 part 1, pp. 3718–3725, Dec. 2006.

[63] C. Dyer, A. Hands, K. Ford, A. Frydland, and P. Truscott, "Neutron-induced single event effects testing across a wide range of energies and facilities and implications for standards," *IEEE Trans. Nucl. Sci.*, vol. 53, no. 6, pp. 3596–3601, 2006.

[64] S. P. Platt, B. Cassels, and Z. Török, "Development and application of a neutron sensor for single event effects analysis," *J. Phys.: Conf. Ser.*, vol. 15, pp. 172–176, Sep. 2005. [Online]. Available: http://stacks.iop.org/1742-6596/15/172

[65] B. Takala and S. A. Wender. Accelerated neutron testing of semiconductor devices. [Online]. Available: http://wnr.lanl.gov/see/poster.pdf

[66] P. Lisowski, C. Bowman, G. Russell, and S. Wender, "The Los Alamos National Laboratory Spallation Neutron Sources," *Nucl. Sci. Eng.*, vol. 106, p. 208, 1990.

[67] P. W. Lisowski and K. F. Schoenberg, "The Los Alamos Neutron Science Center," *Nuclear Instruments and Methods in Physics Research Section A*, vol. 562, pp. 910–914, 2006.

[68] A. V. Prokofiev *et al.*, "A new neutron beam facility at TSL," in *Proc. International Workshop on Fast Neutron Detectors and Applications (FNDA2006)*, Apr. 2006, poS(FNDA2006)016.

[69] ——, "The TSL neutron beam facility," *Rad. Prot. Dos.*, vol. 126, no. 1-4, pp. 18–22, May 2007.

[70] E. Blackmore, P. Dodd, and M. Shaneyfelt, "Improved capabilities for proton and neutron irradiations at TRIUMF," in *Radiation Effects Data Workshop, 2003. IEEE*, 2003, pp. 149–155.

[71] S. P. Platt and Z. Török, "Analysis of SEE-inducing charge generation in the neutron beam at The Svedberg Laboratory," *IEEE Trans. Nucl. Sci.*, vol. 54, no. 4, pp. 1163–1169, Aug. 2007.

[72] Z. Török, S. P. Platt, and X. X. Cai, "SEE-inducing effects of cosmic rays at the High-Altitude Research Station Jungfraujoch compared to accelerated test data," in *European Workshop on Radiation Effects on Components and Systems 2007*, Sep. 2007, paper D-1.

[73] S. P. Platt, Z. Török, C. D. Frost, and S. Ansell, "Charge-collection and single-event upset measurements at the ISIS neutron source," *IEEE Trans. Nucl. Sci.*, vol. 55, 2008, in press.

[74] A. V. Prokofiev *et al.*, "Characterization of the ANITA neutron source for accelerated SEE testing at The Svedberg Laboratory," *NSREC 2009*, 2009.

[75] S. Agostinelli *et al.*, "Geant4–a simulation toolkit," *Nuclear Instruments and Methods in Physics Research Section A: Accelerators, Spectrometers, Detectors and Associated Equipment*, vol. 506, no. 3, pp. 250 – 303, 2003. [Online]. Available: http://www.sciencedirect.com/science/article/B6TJM-48TJFY8-5/2/23ea98096ce11c1be446850c04cfa498

[76] J. Allison *et al.*, "Geant4 developments and applications," *IEEE Trans. Nucl. Sci.*, vol. 53, no. 1, pp. 270–278, Feb. 2006.

[77] P. Dunne, "Characterisation and classification of radiation induced events in optical CCD images," Master's thesis, University of Central Lancashire, Aug. 2005.

[78] Vienna TCAD tools. Vienna University of Technology. [Online]. Available: http://www.iue.tuwien.ac.at/index.php?id=2

[79] P. C. Murley and G. R. Srinivasan, "Soft-error Monte Carlo modeling program, SEMM," *IBM J. Res. Dev.*, vol. 40, no. 1, pp. 109–118, Jan. 1996.

[80] H. H. K. Tang, "Nuclear physics of cosmic ray interaction with semiconductor materials: Particle-induced soft errors from a physicist's perspective," *IBM J. Res. Dev.*, vol. 40, no. 1, pp. 91–108, Jan. 1996.

[81] R. Barrett *et al.*, "MCNP Version 5," *Trans. Am. Nucl. Soc.*, vol. 87, p. 273, 2002.

[82] T. E. Booth *et al.*, "MCNP5 1.50 release notes," 2008.

[83] L. S. Waters, *MCNPX 2.3.0 User's Manuals*.

[84] G. W. McKinney *et al.*, "MCNPX overview," *Proceedings of the 2006 HSSW*, 2006.

[85] *MCNPX Capabilities*. [Online]. Available: https://mcnpx.lanl.gov/opendocs/misc/FeaturesList.pdf

[86] N. Mokhov and S. Striganov, "Mars15 overview," *Hadronic Shower Simulation Workshop AIP Proceedings*, p. 896, 2007. [Online]. Available: http://www-ap.fnal.gov/users/mokhov/papers/2007/Conf-07-008.pdf

[87] G. Battistoni *et al.*, "The FLUKA code: description and benchmarking," *Proceedings of the Hadronic Shower Simulation Workshop*, 2006.

[88] *Geant4 Software License*, Version 1.0 ed., Geant4 Collaboration, http://geant4.web.cern.ch/geant4/license/LICENSE.html, June 2006.

[89] D. Heynderickx, B. Quaghebeur, J. Wera, E. Daly, and H. Evans, "New radiation environment and effects models in ESA's space environment information system (SPENVIS)," in *Radiation and Its Effects on Components and Systems, 2003. RADECS 2003. Proceedings of the 7th European Conference on*, 15-19 Sept. 2003, pp. 643–646.

[90] P. Truscott *et al.*, "MULASSIS - monte carlo radiation shielding simulation for space applications made easy," in *Radiation and Its Effects on Components and Systems, 2003. RADECS 2003. Proceedings of the 7th European Conference on*, 15-19 Sept. 2003, pp. 191–196.

[91] G. Santin *et al.*, "GRAS: a general-purpose 3-D modular simulation tool for space environment effects analysis," *IEEE Trans. Nucl. Sci.*, vol. 52, no. 6, pp. 2294–2299, 2005.

[92] P. Truscott *et al.*, "Neutron energy-deposition spectra measurements, and comparisons with Geant4 predictions," *IEEE Trans. Nucl. Sci.*, vol. 53, no. 4, pp. 1883–1889, Aug. 2006.

[93] A. Chugg *et al.*, "Analyses of CCD images of nucleon-silicon interaction events," *IEEE Trans. Nucl. Sci.*, vol. 51, no. 5, pp. 2851–2856, 2004.

[94] A. M. Chugg, R. Jones, M. J. Moutrie, and P. R. Truscott, "Analyses of images of neutron interactions and single particle displacement damage in CCD arrays," *IEEE Trans. Nucl. Sci.*, vol. 51, no. 6, pp. 3579–3584, Dec. 2004.

[95] A. Keating *et al.*, "Modelling packaging effects on proton irradiation response of NMRC RadFETs new GEANT4 simulations and Co-60 irradiations," in *Proc. 7th European Conference on Radiation and Its Effects on Components and Systems RADECS 2003*, A. Mohammadzadeh, Ed., 2003, pp. 457–463.

[96] R. Lemrania *et al.*, "Low-energy neutron propagation in MCNPX and GEANT4," *Nuclear Instruments and Methods in Physics Research Section A*, vol. 560, pp. 454–459, 2006.

[97] Y.-S. Yeh, C.-H. Wang, H.-M. Liu, T.-C. Liu, and G.-L. Lin, "Simulating neutron propagations with FLUKA, GEANT4 and MCNP," in *IEEE Nuclear Science Symposium Conference Record NSS '07*, vol. 3, 2007, pp. 2016–2018.

[98] *Geant4 Medium Energy Verifications*, GEANT4 Collaboration. [Online]. Available: http://geant4.fnal.gov/hadronic_validation/validation_plots/thin_target/hadronic/mediu

[99] R. A. Reed *et al.*, "Impact of ion energy and species on single event effects analysis," *IEEE Trans. Nucl. Sci.*, vol. 54, no. 6, pp. 2312–2321, 2007.

[100] A. Ciccarelli *et al.*, "Front-illuminated full-frame charge-coupled device image sensor achieves 85% peak quantum efficiency," in *Sensors and Camera Systems for Scientific, Industrial, and Digital Photography Applications III, Proc. SPIE*, vol. 4699, 2002, pp. 153–160.

[101] *Device performance specification Kodak KAF-0402E/ME*, Eastman Kodak Company, Jan. 2003, rev. 1.

[102] J. Ziegler. SRIM & TRIM. [Online]. Available: http://www.srim.org

[103] D. Lambert *et al.*, "Analysis of quasi-monoenergetic neutron and proton SEU cross sections for terrestrial applications," *IEEE Trans. Nucl. Sci.*, vol. 53, no. 4, pp. 1890–1896, Aug. 2006.

[104] J. Baggio *et al.*, "Single event upsets induced by 1-10 MeV Neutrons in Static-RAMs using mono-energetic neutron sources," *IEEE Trans. Nucl. Sci.*, vol. 54, no. 6, pp. 2149–2155, Dec. 2007.

[105] "ENDF/B-VII Incident-Neutron Data," Los Alamos National Laboratory. [Online]. Available: http://t2.lanl.gov/data/neutron7.html

[106] A. Koning, S. Hilaire, and M. Duijvestijn, "TALYS: Comprehensive nuclear reaction modeling," *Proceedings of the International Conference on Nuclear Data for Science and Technology - ND2004*, vol. 769, p. 1154, 2005.

[107] A. M. Chugg *et al.*, "Single particle dark current spikes induced in CCD's by high energy neutrons," *IEEE Trans. Nucl. Sci.*, Dec. 2003.

[108] S. A. Wender *et al.*, "A fission ionization detector for neutron flux measurements at a spallation source," *Nucl. Inst. Meth. Phys. Res., A*, vol. 336, no. 1–2, pp. 226–231, Nov. 1993.

[109] "Neutron fluence calibrations at the TRIUMF neutron facility," May 2008, unpublished report.

[110] S.-B. Ko, "Observation of alpha particle effects in the charge-coupled image sensor," *IEEE Trans. Nucl. Sci.*, vol. 27, no. 6, pp. 1500–1505, 1980.

[111] I. Cornelius, A. Rosenfeld, R. Siegele, and D. Cohen, "LET dependence of the charge collection efficiency of silicon microdosimeters," *IEEE Trans. Nucl. Sci.*, vol. 50, no. 6, pp. 2373–2379, 2003.

[112] T. Lomheim *et al.*, "Imaging charge-coupled device (ccd) transient response to 17 and 50 MeV proton and heavy-ion irradiation," *IEEE Trans. Nucl. Sci.*, vol. 37, no. 6, pp. 1876–1885, 1990.

[113] S. Kirkpatrick, "Modeling diffusion and collection of charge from ionizing radiation in silicon devices," *IEEE Trans. Electron Devices*, vol. 26, no. 11, pp. 1742–1753, 1979.

[114] G. C. Messenger, "Collection of charge on junction nodes from ion tracks," *IEEE Transactions on Nuclear Science*, vol. 29, 1982.

[115] G. Pavlov and J. Nousek, "Charge diffusion in CCD X-ray detectors," *Nuclear Instruments and Methods in Physics Research A*, vol. A 428, pp. 348–366, 1998.

[116] L. D. Edmonds, "A time-dependent charge-collection efficiency for diffusion," *IEEE Transactions on Nuclear Science*, vol. 48, p. 5, 2001.

[117] J. M. Palau *et al.*, "Device simulation study of the SEU sensitivity of SRAMs to internal ion tracks generated by nuclear reactions," *IEEE Trans. Nucl. Sci.*, vol. 48, no. 2, pp. 225–231, 2001.

[118] S. Rodney and J. Tonry, "Charaterizing charge diffusion in CCDs with X-rays," *Astronomical Society of the Pacific*, vol. 118, pp. 866–873, 2006.

[119] G. Rolland, "New analytical solutions of the diffusion equation available to radiation induced substrate currents modeling," *IEEE Trans. Nucl. Sci.*, vol. 55, no. 4, pp. 2028–2035, 2008.

[120] G. Rolland *et al.*, "Stardust: A code for the simulation of particle tracks on arrays of sensitive volumes with substrate diffusion currents," *IEEE Trans. Nucl. Sci.*, vol. 55, no. 4, pp. 2070–2078, 2008.

[121] *Device performance specification Kodak KAF-1401E/ME*, Eastman Kodak Company, Jan. 2003, rev. 1.

[122] G. Rolland. Private comunication, May 2009.

[123] J. R. Janesick, *Scientific Charge-Coupled Devices*. SPIE Publications, 2001.

[124] X. Cai, S. Platt, and W. Chen, "Modelling neutron interactions in the Imaging SEE Monitor," *IEEE Trans. Nucl. Sci*, vol. 56, 2009.

[125] T. Heijmen and J. Verwijst, "Altitude and underground real-time SER tests of embedded SRAM," *RADECS 2009*, 2009.

[126] O. Flament, J. Baggio, C. D'hose, G. Gasiot, and J. Leray, "14 MeV neutron-induced SEU in SRAM devices," *IEEE Trans. Nucl. Sci.*, vol. 51, no. 5, pp. 2908–2911, 2004.

[127] J. R. Schwank *et al.*, "Effects of angle of incidence on proton and neutron-induced single-event latchup," *IEEE Trans. Nucl. Sci.*, vol. 53, no. 6, pp. 3122–3131, 2006.

[128] J. Klug *et al.*, "SCANDAL - A facility for elastic neutron scattering studies in the 50 - 130 MeV range," *Nucl. Instr. Meth. Phys. Res.*, vol. A489, pp. 282–303, 2002.

[129] A. V. Prokofiev *et al.*, "Characterization of the ANITA neutron source for accelerated SEE testing at The Svedberg Laboratory," *NSREC 2009*, 2009.

[130] Z. Török, "Development of image processing systems for cosmic ray effect analysis," Ph.D. dissertation, University of Central Lancashire, 2007.

[131] A. Johnston, T. Miyahira, G. Swift, S. Guertin, and L. Edmonds, "Angular and energy dependence of proton upset in optocouplers," *IEEE Trans. Nucl. Sci.*, vol. 46, no. 6, pp. 1335–1341, Dec. 1999.

[132] XEM3005 user's manual. Opal Kelly Incorporated. [Online]. Available: http://www.opalkelly.com/library/XEM3005-UM.pdf

[133] S. P. Platt, A. V. Prokofiev, and X. X. Cai, "Fidelity of energy spectra at neutron facilities for single-event effects testing," *IRPS 2010 Proceeding*, 2010.

[134] C. Birattari *et al.*, "The extended range neutron rem counter LINUS: Overview and latest developments," *Radiation Protection Dosimetry*, vol. 76, pp. 135–148, 1998.